# EPITAXIAL GROWTH OF ICOSAHEDRAL BORON ARSENIDE ON SILICON CARBIDE SUBSTRATES: IMPROVED PROCESS CONDITIONS AND ELECTRICAL PROPERTIES

by

YI ZHANG

B.S., East China University of Science and Technology, 2004

AN ABSTRACT OF A DISSERTATION

submitted in partial fulfillment of the requirements for the degree

DOCTOR OF PHILOSOPHY

Department of Chemical Engineering
College of Engineering

KANSAS STATE UNIVERSITY
Manhattan, Kansas

2011

# Abstract

The exceptional radiation resistance, high melting point, and wide energy bandgap (3.2 eV) of icosahedral boron arsenide, $B_{12}As_2$, make it an attractive candidate for applications in radiation intense environments, for example, in radioisotope batteries. These devices have potential lifetimes of decades rather than days or weeks that are typical of conventional chemical power cells. Solid state neutron detectors are another potential application of this semiconductor, as the boron-10 isotope has a high thermal neutron capture cross-section, orders of magnitude higher than most elements. To produce high quality crystalline $B_{12}As_2$ for these applications, this research focused on the epitaxy and electrical properties of $B_{12}As_2$ thin films. The major findings include the following.

Twin-free heteroepitaxial $B_{12}As_2$ layers were obtained on *m*-plane 15R-SiC and *c*-plane 4H-SiC inclined 4 °and 7 °off-axis in the [1-100] direction. These substrates exposed asymmetric step-terrace surface structures that force $B_{12}As_2$ layers to adopt a single orientation, thus, twins were eliminated. Consequently, the crystal quality was greatly improved over films on on-axis *c*-plane 6H-SiC, yielding a maximum hole mobility of 80 $cm^2V^{-1}s^{-1}$, nearly 100 times higher than previously reported values. $B_{12}As_2$ epilayers grown at 1300 ℃ had the lowest defect densities, smallest residual strains, highest mobility and highest deposition rate. Excess $AsH_3$ concentration was advantageous to prevent the loss of arsenic from the epilayer.

Undoped $B_{12}As_2$ exhibited a variable-range-hopping conduction, indicating it was a highly disordered system. All films were *p*-type with a room temperature hole concentration on the order of $10^{12}$~$10^{15}cm^{-3}$. The thermal activation energy of acceptors varied from 0.15 eV to 0.33 eV. The Hall mobility was dominated by impurity scattering at low temperatures and by polar phonon scattering at high temperatures.

H, C, O and Si were the major impurities present in the undoped $B_{12}As_2$ films with concentrations on the order of $10^{18}$~$10^{19}$ $cm^{-3}$. Si doping and annealing decreased the resistivity by up to two orders of magnitude. The density of localized states was small in the undoped $B_{12}As_2$ as the intrinsic acceptor levels (IALs) were compensated by the boron interstitials. However, in Si-doped $B_{12}As_2$, Si may prevent the interstitial boron atoms from compensating the IALs, yielding a decreased density of localized states. The Hall mobility of $B_{12}As_2$ epilayer was significantly reduced with increasing silicon concentration.

# EPITAXIAL GROWTH OF ICOSAHEDRAL BORON ARSENIDE ON SILICON CARBIDE SUBSTRATES: IMPROVED PROCESS CONDITIONS AND ELECTRICAL PROPERTIES

by

YI ZHANG

B.S., East China University of Science and Techonology, 2004

A DISSERTATION

submitted in partial fulfillment of the requirements for the degree

DOCTOR OF PHILOSOPHY

Department of Chemical Engineering
College of Engineering

KANSAS STATE UNIVERSITY
Manhattan, Kansas

2011

Approved by:

Major Professor
Dr. James H. Edgar

# Copyright

# Abstract

The exceptional radiation resistance, high melting point, and wide energy bandgap (3.2 eV) of icosahedral boron arsenide, $B_{12}As_2$, make it an attractive candidate for applications in radiation intense environments, for example, in radioisotope batteries. These devices have potential lifetimes of decades rather than days or weeks that are typical of conventional chemical power cells. Solid state neutron detectors are another potential application of this semiconductor, as the boron-10 isotope has a high thermal neutron capture cross-section, orders of magnitude higher than most elements. To produce high quality crystalline $B_{12}As_2$ for these applications, this research focused on the epitaxy and electrical properties of $B_{12}As_2$ thin films. The major findings include the following.

Twin-free heteroepitaxial $B_{12}As_2$ layers were obtained on *m*-plane 15R-SiC and *c*-plane 4H-SiC inclined 4 °and 7 °off-axis in the [1-100] direction. These substrates exposed asymmetric step-terrace surface structures that force $B_{12}As_2$ layers to adopt a single orientation, thus, twins were eliminated. Consequently, the crystal quality was greatly improved over films on on-axis *c*-plane 6H-SiC, yielding a maximum hole mobility of 80 $cm^2V^{-1}s^{-1}$, nearly 100 times higher than previously reported values. $B_{12}As_2$ epilayers grown at 1300 ℃ had the lowest defect densities, smallest residual strains, highest mobility and highest deposition rate. Excess $AsH_3$ concentration was advantageous to prevent the loss of arsenic from the epilayer.

Undoped $B_{12}As_2$ exhibited a variable-range-hopping conduction, indicating it was a highly disordered system. All films were *p*-type with a room temperature hole concentration on the order of $10^{12}$~$10^{15}cm^{-3}$. The thermal activation energy of acceptors varied from 0.15 eV to 0.33 eV. The Hall mobility was dominated by impurity scattering at low temperatures and by polar phonon scattering at high temperatures.

H, C, O and Si were the major impurities present in the undoped $B_{12}As_2$ films with concentrations on the order of $10^{18}$~$10^{19}$ $cm^{-3}$. Si doping and annealing decreased the resistivity by up to two orders of magnitude. The density of localized states was small in the undoped $B_{12}As_2$ as the intrinsic acceptor levels (IALs) were compensated by the boron interstitials. However, in Si-doped $B_{12}As_2$, Si may prevent the interstitial boron atoms from compensating the IALs, yielding a decreased density of localized states. The Hall mobility of $B_{12}As_2$ epilayer was significantly reduced with increasing silicon concentration.

# Table of Contents

# List of Figures

# List of Tables

# Acknowledgements

I wish to express my sincere gratitude to my major professor, Dr. James Edgar, for leading me to the research world of semiconductor material synthesis, characterization and devices. His broad knowledge, detail-oriented guidance, countless help and all-the-time encouragement enabled the completion of this research an enjoyable experience. Appreciation is extended to Dr. Jennifer Anthony, Dr. Keith Hohn, Dr. Andrew Rys and Dr. Bharat Ratra for serving on my advisory committee. I also want to thank Dr. Michael Dudley, Dr. Hui Chen, Dr. Yu Zhang and the research group for defect characterization on icosahedral boron arsenide samples. Thanks are also given to Dr. Martin Kuball, Dr. Yinyan Gong and Dr. Silvia Bakalova for physical properties measurement and device characterization.

I would like to thank Dr. Ed Kenik and Dr. Harry Mayer III from Oak Ridge National Lab. for SEM, SAM and XPS experiments, Dr. Zihua Zhu from Pacific Northwest National Lab. for SIMS experiments and discussions, Dr. Rachel Ward from Naval Research Lab. for x-ray rocking curve measurement, Dr. Douglas McGregor and his research group from Kansas State University for radiation detection measurement and Dr. David Look from Wright State University for Hall effect characterization.

I would also thank my colleagues, Dr. Li Du, Dr. Clinton Whiteley, Kyle Swanson, Wei Gao, Daming Wei, Tashfin Hossain and Clint Frye for their help during my research. Thanks are given to all the faculties and members of the staff in the Department of Chemical Engineering, Kansas State University, for their assistance, willingness to provide feedback and continued support.

# Dedication

TO MY PARENTS

**YAJIE SI** AND **SHUSEN ZHANG**

TO MY SISTER

**BINSI ZHANG**

TO MY HUSBAND

**JUNHU JIANG**

# Chapter 1 - Introduction

## 1.1 Background, Motivation and Hypothesis

Icosahedral boron arsenide, $B_{12}As_2$, one of the icosahedral boron-rich solids, raises the researcher's interest because of their distinctive structures and potential applications in long life-time radioisotope batteries and solid-state neutron detectors. It is a wide bandgap (3.2 eV at room temperature) semiconductor [1], with a high melting point, hardness, resistance to radiation damage and neutron absorption capability [2, 3]. These extraordinary properties stem from its unique structure and bonding configuration. In $B_{12}As_2$, boron atoms form an icosahedra residing at the corners of a rhombohedral unit cell, with the As-As chain spanning the body diagonal. The internal bonds in the icosahedra are electron-deficient: two valence electrons are shared between three atoms [2, 4, 5]. This specific type of bonding enables $B_{12}As_2$ to "self-heal" from radiation damage; vacancies and interstitials caused by radiation spontaneously recombine, due to the strong Coulombic attraction forces between the degraded boron icosahedra and the boron interstitial [2, 4, 6, 7].

The "self-healing" property provides a possible solution for semiconductor device applications in a high irradiation environment. A good example is the betavoltaic cell (or beta-cell), a device that directly converts nuclear energy into electrical power [3, 6-9]. These devices are similar to photovoltaics, except employing beta-particles emitted from radioisotopes instead of photons as the energy and excitation source. Beta-voltaic cells take advantage of the much greater energy density available from nuclear decay compared to chemical reactions. They have the potential to power cells with exceptional lifetimes; they are capable of supplying energy for years rather than days or weeks, typical of electrochemical batteries. Such long-lived nuclear batteries can power remotely located, difficult to maintain environmental sensors. However, when such devices are made of conventional semiconductors, Si or Ge, they cease to function quickly due to radiation damage. This has hindered the development of beta-cells [10]. Thus, $B_{12}As_2$, a semiconductor that can self-heal from radiation damage, may make beta-cells feasible.

Solid state neutron detectors are another potential application for boron-rich compound semiconductors. One of boron's isotopes, $^{10}B$, has a high thermal neutron capture cross-section (~4000 barns), orders of magnitude higher than that of most elements. Thus, it can be exploited for solid-state neutron detectors. The current standard for thermal neutron detectors is based on

tubes filled with the helium-3 isotope, a rare gas. This device has a number of drawbacks: it requires high voltages, it is subject to interference from microphotonics, and is fragile and susceptible to breakage. In addition, the exponential demand for neutron detectors sparked by the 9-11 attack to prevent smuggling of fissile materials and nuclear terrorism has caused a severe shortage of the helium-3 isotope [11]. Thus, there is a demand for alternative technologies for neutron detectors. Compared to helium-3 neutron detectors, solid-state neutron detectors based on $^{10}B$ enriched $B_{12}As_2$ are more sensitive, more compact, operate on minimal power, and could be lower cost [3]. Such devices could be widely distributed near airports, other points of entry, and potential terrorist targets, to provide the earliest warnings possible.

There have been several attempts to make neutron detectors from boron-based semiconductors [12, 13]. However, the efficiency and stability of these detectors was quite poor. A possible reason for this is the poor materials quality employed in prior studies. To advance the technology of boron-based solid state neutron detectors and beta-cells, this research focuses on producing low defect density $B_{12}As_2$ and accurately measuring its properties. This semiconductor has rarely been studied; very few papers have been published on any aspects of this material. By first establishing its fundamental properties, its potential for semiconductor neutron detectors and beta-cells can be realistically evaluated.

Single crystals are preferred compared to amorphous or polycrystalline materials for obtaining the best electrical properties, as the charge carrier mobility in single crystals can be 3 orders of magnitude higher. However, the quality of bulk $B_{12}As_2$ crystals was not reported and the defect densities were unknown prior to this work. The lack of high quality bulk $B_{12}As_2$ crystals with sufficient large dimensions necessitates the heteroepitaxial growth on lattice matched substrates.

In the past, heteroepitaxial $B_{12}As_2$ thin films have been deposited on Si and SiC substrates of various orientations via chemical vapor deposition (CVD). SiC is superior due to its small lattice mismatch and good thermal stability [14]. For films grown on on-axis (0001) 6H-SiC, Nagarajan, Xu and Wang [14, 15, 16] observed a high density of double positioning twins. Michael *et al* [4] theoretically predicted the existence of a number of $B_{12}As_2$ structural variants according to the non-equivalent nucleation sites available on the (0001) SiC surface. The presence of the resulting twin boundaries deteriorates the electrical properties of the semiconductor, and degrades the device performance. Chen *et al* [17, 18] reported the major

defect, rotational twins, were eliminated on a (11-20) 15R-SiC with significantly improved crystal quality. It was found that the specific step-terrace structure on this specific orientation of 15R-SiC limits the nucleation sites and forces the $B_{12}As_2$ to adopt only one orientation. Therefore, we hypothesize that specific orientations of the SiC substrate can eliminate the twins and improve the electrical properties in the epitaxial film.

## 1.2 Aim, Scope and Outline of Dissertation

The primary goal of this project was to produce single crystalline $B_{12}As_2$ epitaxial films with low defect densities and controlled impurity concentrations. The following issues were addressed to produce high quality films and to fabricate solid-state devices. 1) Appropriate orientations and polytypes were sought for SiC substrates to produce untwined high quality $B_{12}As_2$; 2) The effect of temperature, reactant concentration and feed reactant ratio on the growth rate and film quality were investigated, to determine the optimal growth conditions; 3) The film structure, composition and quality, surface morphologies, crystallographic orientations, defects type and densities of the $B_{12}As_2$ film were revealed by commonly used characterization techniques, XRD, SEM, Raman, SAE, TEM and SIMS; 4) The electrical properties of the $B_{12}As_2$ film, carrier density and hole mobility were determined by Hall effect measurements; 5) The electrical properties were tuned by silicon doping, and how the dopant and impurities influent the electrical properties was determined; and 6) the charge carrier transport mechanism was determined via Hall effect measurement.

In addition, two interesting relevant topics are discussed here: 1) icosahedral boron arsenide nanowires were produced via CVD, the first such experiments in the field; and 2) bulk boron carbide crystals, member of icosahedral boron-rich solids, were synthesized by solution growth method and characterized.

## Reference


[1] S. Bakalova, Y. Gong, C. Cobet, N. Esser, Y. Zhang, J. H. Edgar, Y. Zhang, M. Dudley, and M. Kuball, *Phys. Rev. B*, 81, 075114 (2010)

[2] D. Emin, *Phys. Today*, 55, January (1987)

[3] D. Emin and T. L. Aselage, *J. App. Phys.*, 97, 013529 (2005)

[4] J.R. Michael, T. L. Aselage, D. Emin and P.G. Kotula, *J. Mater. Res.*, 20 (11), 3004 (2005).

[5] H. Chen, G. Wang, M. Dudley, L. Zhang, L. Wu, Y. Zhu, Z. Xu, J.H. Edgar and M. Kuball, *J. Appl. Phys.*, 103 (12), 123508 (2008)

[6] M. Carrard, D. Emin and L. Zuppiroli, *Phys. Rev. B*, 51(17), 11270 (1995).

[7] D. Emin, *J. Solid. State Chem.*, 179, 2791 (2006)

[8] D. Emin, *J. Solid. State Chem.*, 177, 1619 (2004)

[9] Y. Gong, M. Tapajna, S. Bakalova, Y. Zhang, J.H. Edgar, Y. Zhang, M. Dudley, M. Hopkins, and M. Kuball, *Appl. Phy. Lett.*, 96(22), 223505(2010)

[10] W. G. Pfan and W. Van Roosbroeck, *J. Appl. Phys.*, 25, 1422 (1954)

[11] D. Dixion, Helium-3 Shortage Could Mean Nuke Detection Disaster, online sources, http://www.wired.com/dangerroom/2010/04/helium-3-shortage-could-mean-nuke-detection-disaster/

[12] F. Wald and J. Bullitt, Semiconductor Neutron Detector, 1973

[13] B. W. Robertson, S. Adenwalla, A. Harken, P. Welsch, J. I. Brand, P. A. Dowben, and J. P. Claassen, *Appl. Phys. Lett.* **80**, 3644 (2002)

[14] R. Nagarajan, Z. Xu, J. H. Edgar, F. Baig, J. Chaudhuri, Z. Rek, E. A. Payzant, H. M. Meyer, J. Pomeroy and M. Kuball, *J. Cryst. Growth*, 273, 431 (2005)

[15] X. Zhou, J. H. Edgar and S. Speakman, *J. Cryst. Growth*, 293, 162 (2006)

[16] S. H. Wang, E. M. Lysczek, Bangzhi Liu, S. E. Mohney, Z. Xu, R. Nagarajan and J. H. Edgar, *Appl. Phys. Lett.*, 87, 042103 ( 2005)

[17] H. Chen, G. Wang, M. Dudley, L. Zhang, L. Wu, Y. Zhu, Z. Xu, J.H. Edgar and M. Kuball, *J. Appl. Phys.*, 103 (12), 123508 (2008)

[18] H. Chen, G. Wang, M. Dudley, Z. Xu, J. H. Edgar, T. Batten, M. Kuball, L. Zhang, and Y. Zhu, *Appl. Phys. Lett.*, 92 (23), 231917 (2008)

# Chapter 2 - Background and Literature Review

## 2.1 Structure and properties of icosahedral boron-rich solid

Icosahedral boron-rich solids are a group of compounds that contain clusters of 12 boron atoms residing at each vertex of icosahedrons. They include α-boron ($B_{12}$), $B_{12}As_2$, $B_{12}P_2$ and $B_{12+x}C_{3-x}$. These compounds have remarkable properties compared with conventional semiconductors, including wide bandgaps (>3 eV) at room temperature, high melting points (>2100℃) and high resistance to radiation damage [1-9]. Thus they are of interest for a variety of applications in high temperature solid state devices, wide bandgap semiconductors and radiation intense environments.

Table 2.1is a summary of physical and electrical properties of crystalline icosahedral boron-rich solids, see next page. These extraordinary properties are the results of their unique structures and bonding configurations.

**Table 2.1 Properties of Crystalline Icosahedral Boron-rich Solids**

| Properties | Alpha-B | $B_{12}As_2$ | $B_{12}P_2$ | $B_{12+x}C_{3-x}$ |
|---|---|---|---|---|
| Color | Red and transparent [10] | Amber or colorless | Varied from black to blue [11] | Bluish gray or dark [12, 13] |
| Lattice Constant (Å) | a=5.057 [14] | a=6.156, c=11.929 [15] a=6.139, c=11.908 [16] a=6.141, c=11.894 [7] | a=5.9876, c=11.8411 [11] a=5.989, c=11.851 [17] | a=5.60 c=12.12 [18]. Varies with C concentrations [19] |
| Melting Point (℃) | 2180-2300 [20] | 2127~2427 [1] | 2120 (under inert gas) [17] | 2427 [21] |
| Density ($g\ cm^{-1}$) | 2.45 [20] | 3.56 [22, 23] | 2.60 [17] | 2.465~2.52 [19] varies with C concentrations |
| Bandgap eV | 2 [24] | 3.48[17], 3.2[4] | 3.35 [17], 3.3[25] | 0.77-1.8[26] |
| Resistivity (Ω cm) | ~10 at T=1000K [27] | p-type, $10^4$~$10^5$[28] T=298K | p-type, $5.2\times10^4$ $9.0x10^4$[29] p-type, $6.2\times10^4$ 6~$10\times10^3$ [11] T=298K | $B_{13}C_2$:2 $B_4C$: 5 [30] T=298K |
| Hole mobility ($cm^2V^{-1}sec^{-1}$) | 100 [31] | 0.5-2 [28] | 100 [31] | 1 [13] |
| Carrier Concentration ($cm^{-3}$) | N/A | $10^{12}$~$10^{15}$ [32] | $1.2\times10^{12}$, $8.9\times10^{11}$ [29] | $10^{21}$ [13] |

### *2.1.1 Structure and Bonding*

In these compounds, twelve boron atoms form icosahedra, lying at each vertex of a rhombohedra, and two group V atoms (As and P) or three C atoms form chains along the body diagonal of the rhombohedra. Shown in Figure 2.1is the unit cell of a representative, icosahedral boron-rich compound, $B_{12}As_2$.

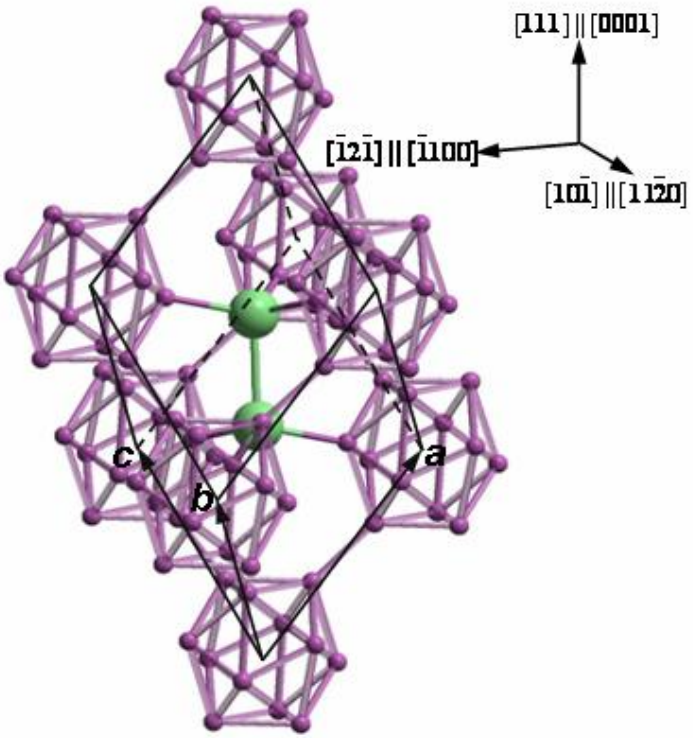


**Figure 2.1 Side view of $B_{12}As_2$ unit cell showing boron icosahedra. B atoms are the smaller spheres and As atoms are the larger spheres. The structure can be equivalently referred to either as a rhombohedral or hexagonal unit cell. a, b and c indicate the rhombohedral unit cell axes. The [111], [121] and [101] directions are indicated, in referrence to the rhombohedral cell, and are equivalent to [0001], [1100] and [1120] directions, respectively, in the hexagonal cell [8].**

Emin [1] described in detail the unusual bonding and crystal structures of icosahedral boron-rich solids. Within each icosahedron there are 36 electrons available for bonding; however, each boron atom provides 4 orbitals, so there are 48 bonding orbitals available to fill. The boron icosahedra are “electron deficient”. Thus the covalent bonds are so called three center bonds: two electrons are shared by three atoms, as illustrated in Figure 2.2. Compared to the conventional

two-center bond, the pair of electrons resides in the midst of the three atoms that are being bonded, instead of residing between each of the two bonding atoms.

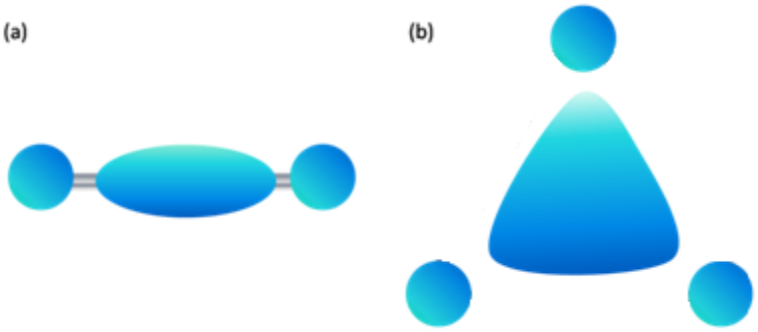


**Figure 2.2 The circles represent B atoms and the colored regions roughly show the dominant part of the electron charge of a (a) two center bond and a (b) three-center bond.**

The highest electron charge density is located not on a line between two boron atoms, but in the center of the icosahedron's triangular faces, as depicted in Figure 2.3.

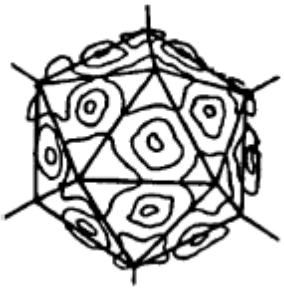

**Figure 2.3 An illustration of icosahedron in $B_{12}As_2$. The contours illustrate accumulation of bonding charge on the triangular faces of the icosahedrons [33].**

Strong and stable three-center bonding occurs only in boron compound [1]. Boron-rich solids are thus very distinctive and unique in forming such strong covalent materials. Worth emphasizing is that icosahedral boron-rich solids are not molecular solids, that is, solids composed of weakly bonded molecular units. They are so-called "inverted molecular solids", because the two-center covalent external bonding is often even stronger and stiffer than that within the icosahedra.

### *2.1.2 Self-healing property*

Icosahedral boron-rich solids survive extremely well in radiation intense environments, which has been attributed to their self-healing property [1-3]. Several boron-rich solids (β-B [34,

35], $B_{12}P_2$ and $B_{12}As_2$ [33, 36]) were investigated by high resolution transmission electron microcopy (HR-TEM) before and after heavy bombardments (e.g. by 400 keV electrons). Figure 2.4 displays HR-TEM images of $B_{12}P_2$ before and after an intense bombardment ($10^{18}$ electrons/($cm^2$ s) by 400 keV electrons to a net dose of about $10^{23}$ electrons/$cm^2$) [33]. Damage such as clustering of defects and amorphization, which would be expected in most materials, was not observed.

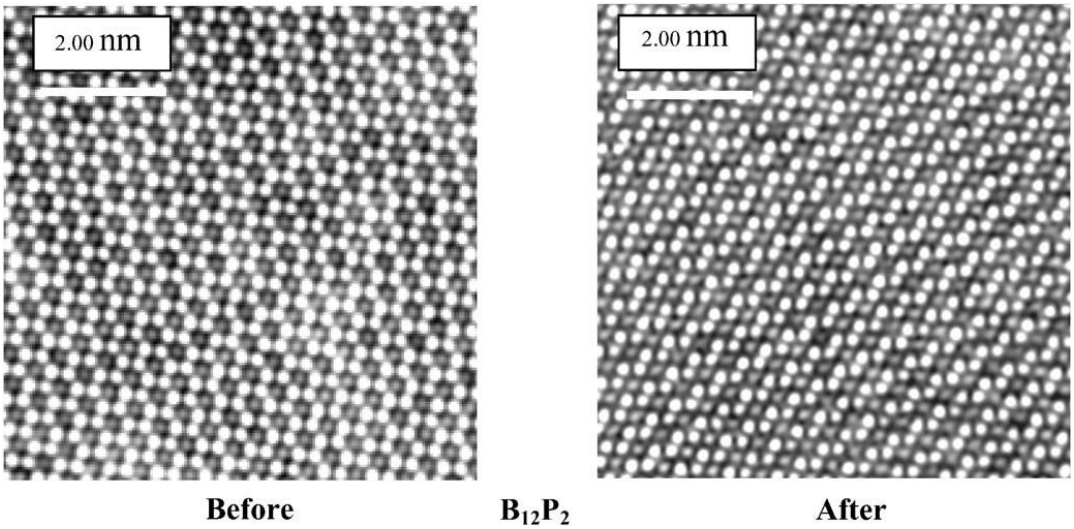


**Figure 2.4 HR-TEM images of $B_{12}P_2$ before and after a high energy electron bombardment [33].**

When highly energetic electrons or ions bombard a solid, atoms of the compound are readily displaced because of the conservation of energy and momentum, creating interstitials and vacancies. When icosahedral boron-rich solids are subjected to energetic particles, boron atoms are kicked off the icosahedron. Consequently, positively charged boron ions and negatively charged degraded-icosahedra are created, as shown in Figure 2.5. The Columbic attraction forces between them are so strong that they draw the small boron ions back to their equilibrium positions spontaneously; the material self-heals from radiation damage. In addition, the boron cation is small, which would aid its diffusion and thereby facilitate recombination. But this self-healing does not occure in boron compounds with conventional two atoms centered bonds, such as BN, BAs or BP, only in compounds with boron icosahedra.

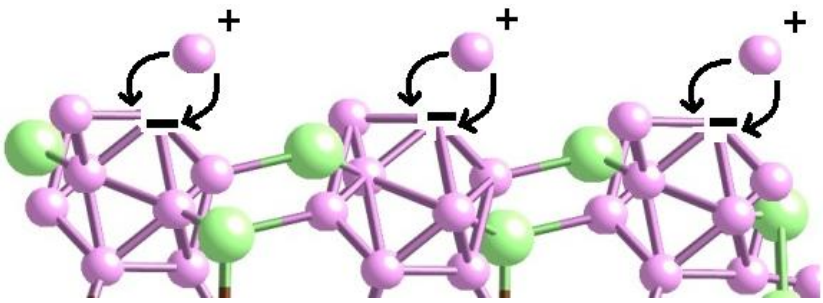

**Figure 2.5 An illustration of the self-healing properties of icosahedral $B_{12}As_2$.**

## 2.2 Synthesis methods for icosaheral boron arsenide

### *2.2.1 Bulk crystal*

#### *2.2.1.1 Direct reaction of elements*

Icosahedral boron arsenide crystals were first produced by the direct reaction of elements [37, 38]. Williams [37] and Ku [38] prepared BAs and $B_{12}As_2$ in two-temperature-zone reactors via direct reaction between B and As (Figure 2.6). Boron and arsenic powder were placed at opposite ends of a sealed and evacuated silica ($10^{-5}$ torr) tube. The arsenic side was heated to 640 ℃. Two products were produced, depending on the temperature and arsenic pressure. Cubic BAs was obtained at 700-900 ℃ with arsenic pressure greater than one atmosphere, and icosahedral $B_{12}As_2$ was produced at 1000 ℃ or above with arsenic pressure less than one atmosphere [37, 38].

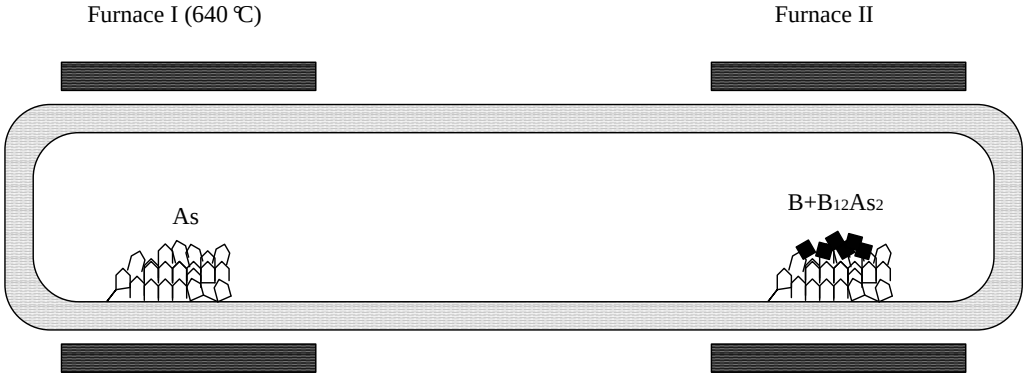


**Figure 2.6 A schematic of a two-temperature-zone quartz reactor used for growing BAs and $B_{12}As_2$ bulk crystals.**

The crystalline BAs and $B_{12}As_2$ obtained by this method contained high concentrations of impurities. For example, Mg, Ag, Al and Pb concentrations were at levels of 50 ppm, probably from the source materials. In crystalline BAs, the Cu and Si concentrations were more than 50 ppm [38]. In the $B_{12}As_2$ crystals, Si concentrations as high as 1% were observed, possibly originated from the silica tube reactor. Thus, such high concentrations of impurities are expected to diminish the charge carrier transport properties of $B_{12}As_2$ crystals, such as the hole mobility and minority carrier lifetimes. Also, the size of these crystalline BAs and $B_{12}As_2$ was not reported in the literature [37, 38]. Therefore, the growth of high quality $B_{12}As_2$ crystals with dimensions in the range of millimeter to centimeter is our goal.

#### *2.2.1.2 Solution growth from metal flux*

Bulk $B_{12}As_2$ crystals have also been precipitated by reacting As vapor with a molten boron-metal solution. Aselage [39] grew $B_{12}As_2$ crystals from Pd-B solution at temperature of 1215 ℃. Whiteley *et al* [9] grew $B_{12}As_2$ crystals from Ni-B solutions at a temperature of 1150 ℃.

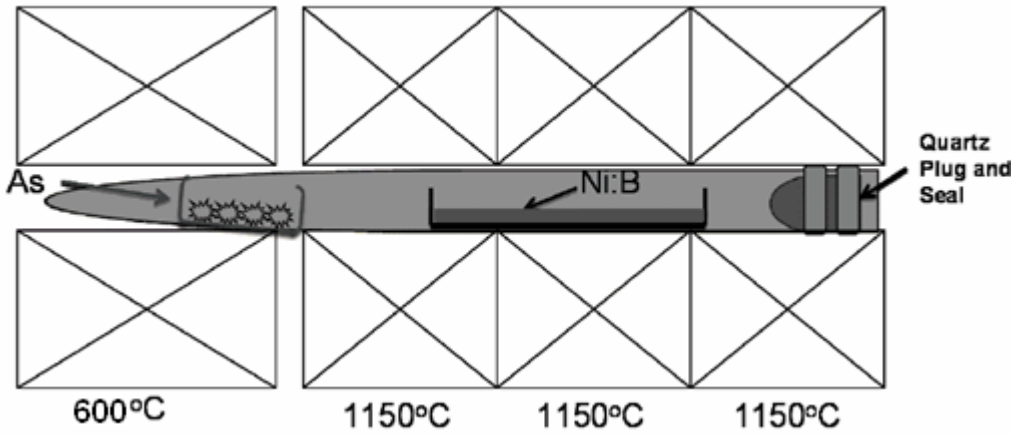


**Figure 2.7 A schematic of a two-temperature zone reaction used for growing $B_{12}As_2$ crystals from a molten boron-nickel solution [9].**

As shown in Figure 2.7, a boron-nickel mixture and arsenic powder were placed at opposite ends of a sealed and evacuated ($10^{-6}$ torr) quartz tube. The arsenic side was heated to 600 ℃ to maintain a high As vapor pressure in the reactor, and the boron-nickel side was held at 1150 ℃ to form a homogenous liquid mixture. It was held at this temperature for 48 hours. Then the system was slowly cooled by 3.5 ℃/hr, to precipitate $B_{12}As_2$ crystals from the liquid phase. Crystals with dimensions up to 1 $cm^2$ in cross-section were obtained, the largest to date.

Hydrogen, carbon, oxygen and silicon were the major impurities detected in those bulk crystals, with concentrations on the order of $10^{20}$, $10^{19}$, $10^{19}$ and $10^{17}$ $cm^{-3}$, respectively [80]. The H, C and O may have come from the original source materials. Si originated from the quartz tube. The impurities concentrations were high enough to be considered degenerate and certainly producing trapping, or recombination centers in the $B_{12}As_2$ crystals.

### *2.2.2 Chemical vapor deposition (CVD) of epitaxial film*

Compared to bulk crystal growth, CVD is capable of producing much higher purity $B_{12}As_2$ films due to the low residual impurities in source gases employed in this method. Epitaxy refers to the method of depositing a single-crystalline film on a single-crystalline substrate. The substrate serves as a seed crystal, thus the deposited film takes on a lattice structure and orientation that matches that of the substrate. If a film is deposited on a substrate of the same composition, the process is homoepitaxy; otherwise it is heteroepitaxy. In the absence of native substrates, $B_{12}As_2$ has been heteroepitaxially grown on substrates with compatible structural parameters.

As a process, CVD enables excellent control of the composition, stoichiometry, and impurity concentration in the thin film-all necessary properties for making electronic device. A typical schematic of the CVD process is shown in Figure 2.8. This is a cold-wall CVD reactor cooled by water. A hollow susceptor is placed inside the reactor with insulation and heated inductively.

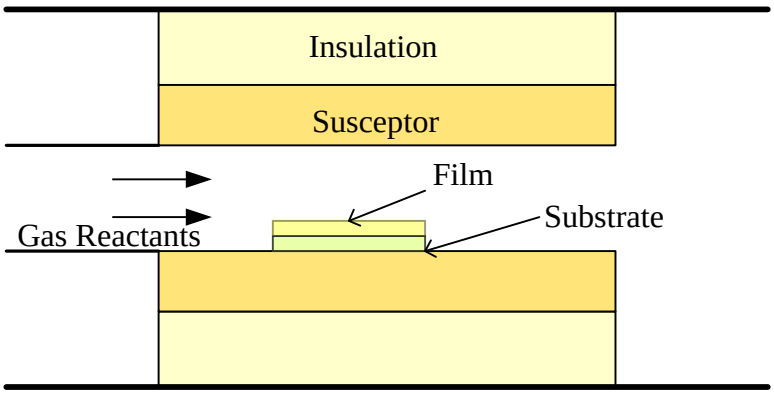


**Figure 2.8 Schematic of a typical CVD growth of $B_{12}As_2$**

The gas phase reactants in a carrier gas flow over a heated substrate held in a susceptor. Thin films of $B_{12}As_2$ are deposited on the substrate by the following reaction.

$$6B_2H_6 + 2AsH_3 \rightarrow B_{12}As_2 + 21H_2$$

The substrate and process conditions are the key parameters that determine the crystal quality of the epitaxial film. The effects of substrate and process conditions on the $B_{12}As_2$ growth are reviewed in the following. The conditions reported for $B_{12}As_2$ thin film growth by CVD in the literature are summarized in Table 2.2

**Table 2.2 Summary of growth conditions of $B_{12}As_2$ thin films growth by CVD**

| B Source | Flow Rate (sccm) | As Source | Flow Rate (sccm) | Carrier Gas | Flow Rate (slm) | Substrates | Temperature (℃) | Pressure (torr) | Ref. |
|---|---|---|---|---|---|---|---|---|---|
| $B_2H_6$ | 2 | $AsH_3$ | 8 | $H_2$ | 20 | SiC, Si(111) NaF(111), | 800-850 | N/A | [40] |
| $BBr_3$ | | $AsCl_3$ | | | | W, Ni, Fused quartz, Si (111), (100) | 800-1150 | | [41] |
| 1%$B_2H_6$ in $H_2$ | 30 | 1%$AsH_3$ in $H_2$ | 30 | $H_2$ | 2.5 | Si(100),(110) Si(111) | 1150 | N/A | [42] |
| 1%$B_2H_6$ in $H_2$ | 50 | 1%$AsH_3$ in $H_2$ | 50 | $H_2$ | 5 | (0001)6H-SiC | 1150 | 100 | [5] |
| 1%$B_2H_6$ in $H_2$ | 20-100 | 2%$AsH_3$ in $H_2$ | 40-100 | $H_2$ | 5 | (0001)6H-SiC | 1100-1450 | 100 | [6] |
| 1%$B_2H_6$ in $H_2$ | 10 | 2%$AsH_3$ in $H_2$ | 100 | $H_2$ | 2.5 | Si(100),(110), and (111) | 1300 | 500 | [7] |
| 1%$B_2H_6$ in $H_2$ | | 2%$AsH_3$ in $H_2$ | | $H_2$ | | 15R-SiC (1-100) | 1200 | 500 | [43] |

#### *2.2.2.1 Effects of Substrate*

Correia *et al* [41], Hirayama *et al* [42] and Xu *et al* [7] reported the growth of $B_{12}As_2$ films by CVD on (100), (101), (110) and (111) Si and other substrates. The films thus obtained were either amorphous or polycrystalline. The orientation relationships were as follows: $B_{12}As_2$ (110)<1-10>// Si(100) <100>, $B_{12}As_2$ (110)<1-10>// Si (110) <1-10>, and $B_{12}As_2$ (211)<11-2>// Si (111) <-101>. In comparison with SiC, silicon substrates were not stable at the deposition temperature of 1150 ℃. Silicon from the substrate could diffuse into the $B_{12}As_2$ films, resulting concentrations as high as 4 atomic%.

Chu *et al* [40] decomposed a $B_2H_6$-$AsH_3$ mixture in a hydrogen atmosphere to deposit $B_{12}As_2$ films on the basal plane of hexagonal silicon carbide, sodium fluoride (111), and silicon (111) substrates at 800 ℃-850 ℃. Adherent $B_{12}As_2$ films with random orientations were deposited on the silicon carbide substrates. Amorphous films were obtained on silicon substrates. The film deposited on the sodium fluoride substrates peeled off due to the large differences of their coefficients of thermal expansion.

Although Chu *et al* [40] claimed the films obtained were BAs, it is more likely that they were actually $B_{12}As_2$ because of an erroneous interpretation of the electron diffraction pattern, as argued later by Correia [40, 41]. Correia *et al* [41] also claimed that it was probably impossible to prepare BAs by CVD synthesis from halide or hydride sources because CVD synthesis from halide or hydride sources was not able to provide an arsenic pressure over 1 atm, which was necessary for growing BAs crystals.

Xu *et al* [7] reported crystalline $B_{12}As_2$ thin films were obtained on Si (100), Si (110) and Si (111) substrates. “Cross”, “wire” and “chain” morphologies were formed on these substrates, respectively. On Si (100), the $B_{12}As_2$ films had a 4-fold symmetry; on Si (111), the $B_{12}As_2$ films exhibited a wire-like structure; while on Si (110), $B_{12}As_2$ thin films displayed two in-plane rotational orientations.

Silicon carbide is a more suitable substrate for the growth of $B_{12}As_2$ than Si because of two important advantages [6]: its basal plane lattice parameter (3.080Å) is close to one-half of that of the a-axis lattice parameter of $B_{12}As_2$ (6.156Å), and its thermal stability is excellent. For example, Wang *et al* [5] deposited $B_{12}As_2$ thin films on (0001) and 3.5 ° off (0001) 6H-SiC

substrates at 1150 ℃ using the $B_2H_6$-$AsH_3$-$H_2$ system. The films were oriented with (0001) $B_{12}As_2$//(0001)6H-SiC and (10-10) $B_{12}As_2$//(10-10) 6H-SiC.

Nagarajan *et al* [6] deposited $B_{12}As_2$ thin films using the same source gases on (0001) 6H-SiC at higher temperatures, up to 1450 ℃. The resulted orientation relationship was (0001)<10-10>//(0001)<11-20>. However, unevenly distributed double positioning twins were observed in all the $B_{12}As_2$ films. Therefore, the microstructural quality of films deposited on 6H-SiC was relatively poor.

Chen *et al* [43] reported that a single crystalline and untwined $B_{12}As_2$ film was achieved on an *m*-plane 15R-SiC. Observations of the $B_{12}As_2$ on *m*-plane, i.e. (1-100), 15R-SiC by synchrotron white beam x-ray topography provided global determination that the film was single crystal with a (353) orientation and was twin free. Raman spectra confirmed this improved film quality as the Raman line-width was narrower and intensity was significantly stronger. High resolution transmission electron microscopy also showed a clean and untwined interface between film and substrate. The effects of substrate on the film quality are summarized in Table 2.3.

**Table 2.3 Effects of Substrate on Film Quality**

| Substrate | Film Quality |
|---|---|
| (100)Si, (110) Si and (111)Si | Amorphous or polycrystalline.<br>High Si concentration in the film |
| (111) Sodium Fluoride | Film peeled off due to high level of stains |
| (0001) 6H-SiC, on-axis or 3.5° C off towards (11-20) direction | Double positioning twins |
| *m*-plane15R-SiC | Single-crystalline, twin free |

### *2.2.2.2 Effects of Process Gas*

Instead of using $B_2H_6$-$AsH_3$-$H_2$, Correia *et al* [41] prepared $B_{12}As_2$ thin films with $BBr_3$-$AsCl_3$-$H_2$. The deposition temperature varied from 800 to 1150 ℃. No deposits formed at temperatures less than 1050 ℃ with the $BBr_3$ flow rate less than 6 x $10^{-6}$ mol/s. Amorphous $B_{12}As_2$ films, and polycrystalline $B_{12}As_2$ films were obtained depending on the deposition temperatures and gas flow conditions. The quality of $B_{12}As_2$ films grown by using $BBr_3$-$AsCl_3$ as the reactant gases was not characterized.

### *2.2.2.3 Effects of Temperature*

The growth temperature is an important factor that affects the $B_{12}As_2$ growth rate by the CVD method. Table 2.4 lists the growth rate variations with temperature reported in the literature. The majority of the growth rates reported are several microns per hour between 800-1450 ℃.

**Table 2.4 Growth rate variations with temperature**

| Temperature ℃ | Growth Rate μm/h | Ref. |
|---|---|---|
| 1150 | 36 | [42] |
| 800-850 | 3-4 | [40] |
| 1150 | 0.2 | [5] |
| 1150 | 1.5 | [6] |
| 1400 | 5 | [6] |
| 1450 | 3.3 | [6] |
| 1200 | 3 | [7] |

Nagarajan *et al* [6] reported the growth rate of $B_{12}As_2$ on 6H-SiC at various temperatures with other parameters being constant. The growth rate increased from 1.5 μm/h at 1150 ℃ to 5 μm/h at 1400 ℃ and decreased to 3.3 μm/h at 1450 ℃. The growth rate of 5 μm/h at 1400 ℃ is significantly higher than the value of 1.5 μm/h at 1150 ℃, demonstrating the critical effect of temperature on the growth rate. The maximum growth rate observed at 1400 ℃ might be due to significant desorption of the reactants at higher temperatures. Another possibility is that the SiC starts to decompose at 1400 ℃ or above. According to the plot of logarithm of the growth rate versus the inverse temperature, the activation energy value for the growth of $B_{12}As_2$ on 6H–SiC was calculated to be 95.4 kJ/mol at relative low temperature range (1150-1400 ℃), suggesting that the growth is kinetically controlled.

In this study, we found the growth rate varied slightly with temperatures ranging from 1200 to 1400 ℃. But there was insufficient evidence to confirm that the growth rate was dependent on the temperatures as the measurements of the film thickness exhibited a comparative standard deviation comparable to the mean value.

#### *2.2.2.4 Effects of Reactant Flow Rate*

In some reports on $B_{12}As_2$ deposition, a large arsine to diborane ratio was used to provide sufficient As partial pressure in the vapor phase. The growth rate reported by Wang *et al* [5] at 1150 ℃ was only 0.2 μm/h, which was significantly lower than that of Nagarajan [6] at the same temperature. The As/B ratio used by Wang *et al* [5] was 1:2 while that by Nagarajan *et al* [6] was over 5:1. These results suggest that excess arsine is necessary in this process.

Nagarajan *et al* [6] also evaluated the effect of diborane flow rate on the growth rate. They reported that the growth rate was proportional to the flow rate of diborane under the conditions of excess arsine.

The As/B ratio also affects the $B_{12}As_2$ film's surface morphology. With the increasing of arsine concentration, the films became more and more smooth. At an 8:1 $AsH_2$:$B_2H_6$ ratio and above, no triangular features were observed, resulting in a very smooth mirror-like surface. This is another reason to keep excess arsine in the system.

In summary, SiC is a successful substrate used in the epitaxial growth of $B_{12}As_2$ by CVD. The surface structure of the SiC substrates, determined by polytypes and orientation, has critical effect on the microstructural quality of the films. *m*-plane 15R-SiC is a prospective substrate which can eliminate twins and the improve crystal quality. However, this polytype of SiC substrate is not commercially available. In this study, we found the (0001) 4H-SiC with 4 ° or 7 ° off-axis towards (1-100) direction can also produce twin-free single crystalline $B_{12}As_2$ films. The details can be found in Chapter 4.

The optimal growth temperature lies within 1100-1450 ℃ with $B_2H_6$ and $AsH_3$ as the reactant gases. The activation energy for the growth of $B_{12}As_2$ on 6H-SiC was 95.4 kJ/mol at 100 torr, suggesting that the growth is kinetically controlled. The growth rate was increased with temperature first because it was a reaction rate control process. However, the reactants' desorption became more significant at high temperature, decreasing the growth rate above 1400 ℃. Deposition with excess arsine in the system is beneficial; it produced higher growth rates and smoother surfaces.

## 2.3 Semiconductor electrical properties and measurement

### *2.3.1 Basics of semiconductors and their electrical properties*

A semiconductor is a material which has a conductivity intermediate between that of a conductor and an insulator. Current (charge transport) occurs either by the flow of negative electrons or positive holes. The conductivity of semiconductors may be modified by incorporating impurities into their crystal lattice, in a process referred to as doping. This property is essential for electronic devices. If the incorporated impurity atoms create excess electrons, they are donors, while those that create holes are acceptors. Semiconductors doped with donor impurities are *n*-type, whereas those doped with acceptor impurities are *p*-type. Pure semiconductors, or intrinsic semiconductors, have equal concentrations of electrons and holes. However, *n*-type or *p*-type semiconductors (extrinsic semiconductors), have a majority carrier concentration of electrons or holes, respectively. Charge carrier mobility ($\mu$), electron mobility ($\mu_e$) or hole mobility ($\mu_p$), characterizes how quickly an electon/hole can move through a semiconductor in an electrical field.

Resistivity ($\rho$), carrier type and concentration (*n* or *p*), carrier mobility ($\mu$) are the most important electrical properties of a semiconductor material. All these properties can be obtained by combining resistivity measurement with Hall effect measurement. The details of resistivity and Hall effect measurement are discussed in section 2.4.9.

### *2.3.2 Electrical properties of icosahedral boron arsenide*

There have been few reports on the electrical properties of $B_{12}As_2$; here we review what little has been reported on icosaheral boron-rich solids. Most icosahedral boron-rich solids exhibit exclusively *p*-type conductivity. Prior to the present study, the maximum reported hole mobility of $B_{12}As_2$ was 0.05-2 $cm^2V^{-1}s^{-1}$ [28] and that of an analogous compound, $B_{12}P_2$, was 50-100 $cm^2V^{-1}s^{-1}$[31]. A *p*-type dopant, Si, was demonstrated by Xu *et al* [28]. The resistivity of $B_{12}As_2$ was decreased four orders of magnitude in proportion to the silicon concentration [28]. Emin [33] proposed that the inter-icosahedral bonding maintained when an atom of As is replaced by a group IV element, e.g., Si, thereby producing *p*-type dopant. However, substitutions of group VI elements were predicted to be ineffective in producing *n*-type $B_{12}As_2$.

n-type conductivity in beta-rhombohedral boron was only achieved by interstitial doping with C, Cr, Fe and Ni [44].

At present, there are two competitive mechanisms to describe the electronic transport properties of the icosahedral boron-rich semiconductors [45]:

(1) Quasiamorphous concept

This concept was initially postulated by Berezin [46] and elaborated on by Golikova [31, 47, 48]. Golikova proposed the boron-rich solids represent a new class of quasiamorphous semiconductors, and the degree of amorphisation depended on the number of boron atoms per unit cell. Accordingly, α-boron would behave like crystalline semiconductors, while $YB_{66}$, which has more than 1600 atoms per unit cell, behaves like an amorphous semiconductor.

Most boron-rich solids exhibit low mobility, which was ascribed to the transition from transport in the extended states to transport in the localized states in such compounds [47]. The temperature dependence of the electrical conductivity follows Mott's law, suggesting the conduction is achieved by a variable range hopping mechanism.

$$\sigma = \sigma_0 \exp\left[-\left(\frac{T_0}{T}\right)^{1/4}\right]$$

This conduction mechanism describes the conduction in strongly disordered systems with localized states. Variable range hopping mode is also found in other icosaheral boron compounds, such as beta-rhombohedral boron, tetragonal boron nanobelt and boron carbide [45, 49, 50]. Hirikara *et al* [50] studied the carrier doping in boron nanobelts (BNB) by neutron transmutation.

(1) $^{10}B + n \rightarrow {}^{7}Li\ (0.84\ MeV) + {}^{4}He(1.47\ MeV) + \gamma(0.48\ MeV)$ (94%)

(2) $^{10}B + n \rightarrow {}^{7}Li\ (1.02\ MeV) + {}^{4}He(1.78\ MeV)$ (6%)

Li atoms generated by neutron transmutation were possibly doped into the interstitial sites of the boron crystal. The Li-doping into BNB increased its conductivity and decreased its temperature coefficient. The variable range hopping conduction mode was demonstrated by the temperature dependence of the conductivity, as shown in Figure 2.9. This is qualitatively understood as an increase in the density of localized states near $E_F$ induced by the dropping out of interstitial B atoms and the reappearance of intrinsic acceptor level.

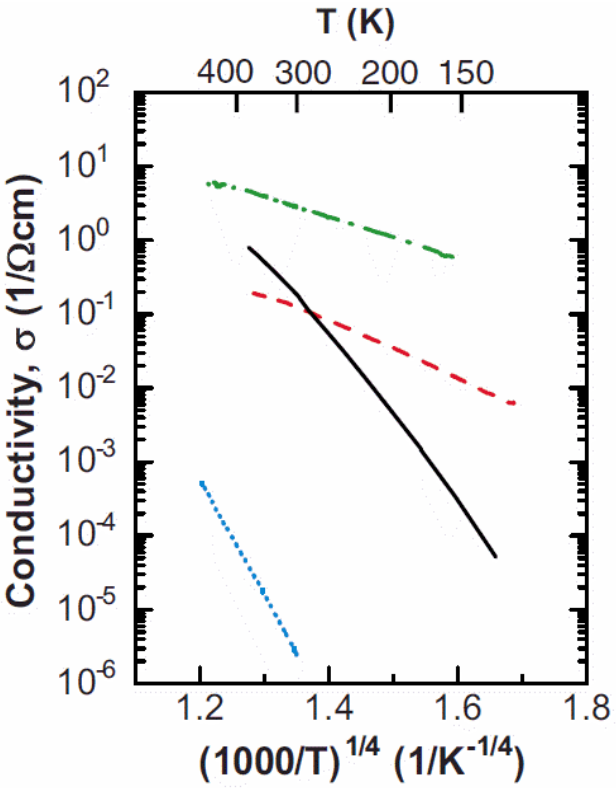


**Figure 2.9 Temperature dependence of σ, shown as log(σ) vs. $T^{-1/4}$ plot. Pristine BNB (black solid line), as-irradiated BNB (blue dotted lines), annealed BNB after irradiation (red broken line), and Li doped BNB by vapor-diffusion doping (green dash-dotted line) [50].**

However, several reliable experimental results contradict this model. For example the electrical properties of boron carbide, which has only 15 atoms per unit cell, is close to the crystalline border-range of the model. Thus, the hole mobility of boron carbide should be similar in range to $B_{12}P_2$, 50-100 $cm^2V^{-1}s^{-1}$[47]. However, the mobility of boron carbide reported was less than 1 $cm^2V^{-1}s^{-1}$ and behaves like an amorphous semiconductor [45].

(2) Hole-bipolaron hypothesis

This hypothesis, initially developed by Howard, Beckel and Emin [51, 52] for boron carbide, assumes hole bipolarons hopping between $B_{11}C$ icosahedra in boron carbide. The only experimental basis for this theory is the very low excited state spin density of boron carbides. Several other explanations are feasible. It seems to be disproved by numerous concrete experimental results [45, 53]. The electrical conductivity maximum occurs at the minimum density of $B_{11}C$ icosahedra in boron carbide; the experimentally determined temperature

dependence of the dynamical conductivity is opposite to that theoretically predicted for bipolarons [45, 53].

Based on current research results, numerous scientific problems remain to be solved, and the electrical properties of the icosahedral boron-rich solids in general are far from being fully understood. This thesis addresses this need and reports our efforts to understand the electrical properties of icosahedral boron arsenide, for the first time.

## 2.4 Characterization methods

The properties of a semiconductor material are highly dependent on the structural quality which is in turn determined by the crystal growth process. Characterization is needed of the structural, chemical and electrical properties of the $B_{12}As_2$ crystals produced, as the resulting information is valuable for optimizing the process conditions. Also fundamental properties of $B_{12}As_2$, of which few have been reported, especially the electrical properties, are essential for fabricating electronic devices.

In the present work, the combined use of SEM, EDS, AFM, Raman, XRD, SWXRT, SAEM, XPS, SIMS and Hall effect measurement was employed for the characterization of crystalline $B_{12}As_2$.

### *2.4.1 Scanning electron microscopy and energy- dispersive x-ray spectroscopy (SEM & EDS)*

SEM provides information about the topography and chemical composition by scanning the sample with a high-energy electron beam and detecting the secondary and/or backscattered electrons. Several signals [54] are produced by the interaction between the incident electrons and the sample atoms, as illustrated in Figure 2.10. (1) Standard SEM images are formed from low-energy secondary electrons ejected from the outermost layer (1-10 nm) of the specimen; (2) high energy backscattered electrons (BSE) are used for BSE imaging; (3) The energy of the x-rays are indicative of the elements present, thus it is utilized in energy-dispersive x-ray spectrometry (EDS) to determine the elemental composition and distribution of the sample surface. (4) Auger electrons, the energy of which is a characteristic of the emitting atom, are used for chemical and composition analysis. This will be discussed in section 2.4.6 in detail.

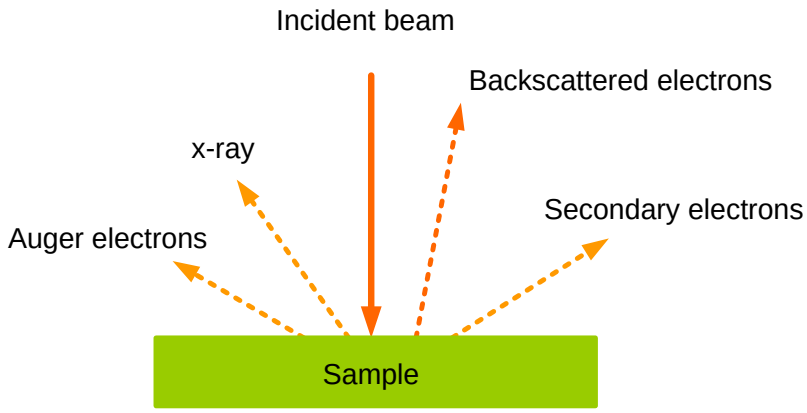


**Figure 2.10 Illustration of signals generated when an electron beam bombards a sample surface.**

The intensity of these signals is determined by the beam current and the resolution of the image depends on the beam diameter. The energy of the incident electrons in the SEM are typically in the 5-30 keV range [55]. Depending on the instrument, the resolution can fall between 1-20nm. By 2009, the highest SEM resolution was 0.4 nm, obtained at 30kV [89].

Energy dispersive x-ray spectroscopy (EDS) are most commonly found on a SEM, which can accurate identify the high atomic weight (Z) elements ($Z \geq 23$), and some low Z ($Z \geq 4$-6) materials. By combining the high spatial resolution, depth of field in the same image, minimal sample preparation and non-destructive measurement, SEM-EDS technique is widely used for examining the microstructure and chemical composition of solid surfaces.

### *2.4.2 Atomic force microscopy (AFM)*

AFM is a high resolution scanning probe microscopy, capable of imaging on the order of fractions of a nanometer. It utilizes a cantilever with a sharp tip to scan the specimen surface. When the tip is brought sufficiently near the specimen surface, force between the tip and the sample lead to a deflection of the cantilever. Measuring and recording the deflection of the cantilever results a topographic image of the sample surface [56].

AFM can operate in either contact or non-contact (tapping mode). Contact mode, also known as static or repulsive mode, was employed for all analysis in this study. This was appropriate because the icosahedral boron arsenide and the silicon carbide substrates have hard flat surfaces that can't be damaged by the probe tip. AFM works by lightly scanning a probe tip or cantilever, typically measuring a couple of nanometers in diameter, over the surface with fixed

contact force. Surface characteristics are measured by changes in the angle of the refracted laser due to repulsive force acting on the probe as it moves toward or away from the surface, as shown in Figure 2.11. The angle of the probe is measured using a focused laser, which refracts off the tip, and is detected by a photodiode. The substrate surface was characterized by AFM before and after hydrogen-etching, to verify the formation of atomically smooth surfaces of the SiC substrates.

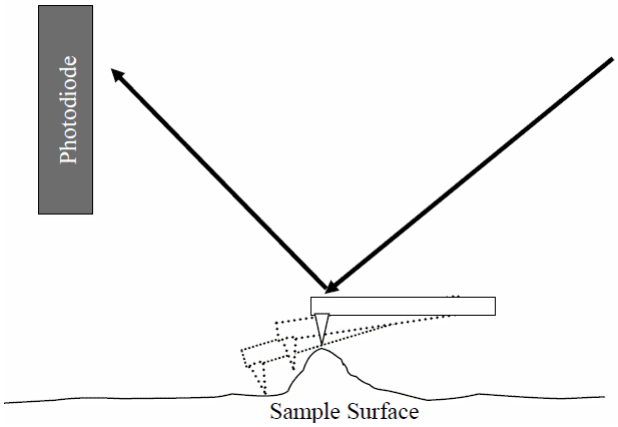


**Figure 2.11 Depiction of a probe in contact mode, for AFM imaging [57]**

### *2.4.3 Raman spectroscopy*

Raman spectroscopy has been widely used in chemistry for molecule identification, structure determination, and changes in chemical bonding, etc. When electromagnetic radiation is incident on a material, most of the scattered radiation retains in its original frequency, but a small fraction is scattered with either slightly lower or higher frequencies. Scattered light that is shifted in frequncy due to vibrations in molecules or optical phonons in solids, is said to have Raman scattered.

With anisotropic crystals, Raman spectroscopy can provide information on the crystal orientation. The polarization of Raman scattered light with respect to the crystal and the polarization of the incident laser light can be used to find the orientation of the crystal. The amount of the polarizability change determines the Raman scattering intensity [58]. Raman scattered light is shifted by as much as 4000 $cm^{-1}$ from the incident light. The pattern of shifted frequencies is determined by the vibrational states of the material. A Raman spectrum shows the intensity of scattered light as a function of shift ($cm^{-1}$) in wavenumbers from the incident light. Raman spectroscopy also indicates the strain levels in a material from shifts in the peak position,

and the crystal quality by the width of the peaks; the narrower the peaks the better the crystal quality.

There is no special sample preparation necessary to collect the Raman spectra. Therefore, Raman spectroscopy was employed in this study to identify the crystal and evaluate the crystal quality.

### *2.4.4 X-ray diffraction (XRD)*

When x-rays interact with a crystalline substance, a diffraction pattern is generated, which is a fingerprint of the substance. XRD is useful to determine the orientation of crystals, measure the average spacing between layers or rows of atoms, indicate the crystal structure of unknown materials and evaluate the size, shape and internal stress of crystalline substances.

In a crystalline material, samples are composed of parallel lattice planes that are spaced at regular intervals. The condition for constructive interference of x-rays is given by Bragg's law [59].

$$\lambda = 2d_{hkl} \sin\theta_{hkl} \tag{2-1}$$

where $\theta$ is the angle between the incident (and diffracted beam) and the atomic planes, $\lambda$ is the wavelength of the incident x-rays and d is the space between lattice planes in crystals.

In this study, XRD was employed to identify the formation of $B_{12}As_2$ crystals and determine the orientation of the epitaxial film. X-ray rocking curve measurements were conducted to evaluate the crystal quality in epitaxial $B_{12}As_2$ thin films.

The width of the rocking curve is a direct reflection of the quality of the crystal. In order to obtain a rocking curve scan, a θ-2θ scan is carried out first. In the next step, the angle θ, and the detector position 2θ, is fixed at the Bragg angle of the corresponding reflection. A rocking curve scan is then acquired by varying the orientation of the sample by an angle Δω around its equilibrium position, while keeping the x-ray source and detector positions fixed. The narrower the rocking curve, the higher the crystal quality. There are various causes of the broadening of the rocking curve such as dislocations, misorientation or residual strain. Therefore, the full-width at half maxium (FWHM) of the rocking curve is used as a gauge of the quality of the film.

### *2.4.5 Synchrotron white beam x-ray topography (SWBXT)*

X-ray topography refers to a family of x-ray diffraction imaging techniques, capable of producing detailed mappings of the physical features of a crystalline solid. This is most readily performed using x-rays from a synchrotron sources. A synchrotron white beam x-ray source has a large-area beam of low divergence and high intensity (50 mm x 5mm), good spatial resolution capability (~ 0.04 μm) and broad wavelength range (0.3~1.6Å). Thus, SWBXT is able to characterize the nature and distribution of structural defects, including dislocations, inclusions/precipitates, stacking faults, growth sector boundaries, twins and low-angle grain boundaries in single crystal materials.

With high strain sensitivity, high intensity, suitable spatial resolution and broad spectral range, SWBXT has been a powerful non-destructive tool to investigate the crystallographic orientations and defect structures of various crystals, such as SiC [60-63]. In this work, SWBXT was utilized to determine the $B_{12}As_2$ film/SiC substrate epitaxial relations, the overall crystal quality and macrostructures of epitaxial samples. There are three main types of SWBXT techniques, consisting of back reflection, transmission (including scanning mode) and grazing incidence geometries. Transmission mode was chosen here to characterize the epitaxial relationship between the $B_{12}As_2$ epilayer and the SiC substrate. The x-ray detecting film is placed behind the sample at the same height to record the diffraction pattern, as depicted in Figure 2.12 [64]. The recorded diffraction patterns are from both substrate and the epilayer.

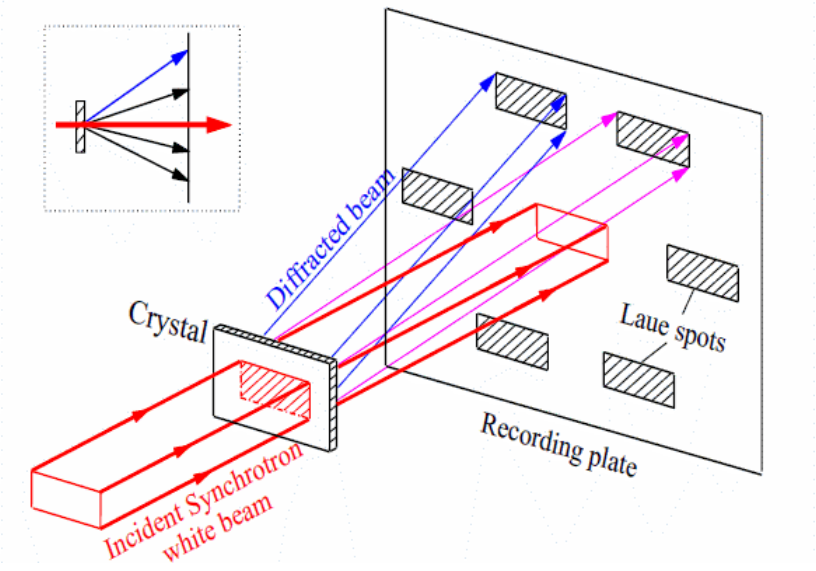


**Figure 2.12 Schematic of transmission SWBXT**

To determine the film/substrate epitaxial relationship, small beam sizes were employed so as to avoid overlapping of diffraction spots and to better facilitate the indexing process. Longer exposure times were employed to increase the intensity and contrast of the $B_{12}As_2$ diffraction patterns. Global views of the quality and structure of the crystals were obtained by recording scanning transmission Laue patterns from the whole crystal volume [64].

### *2.4.6 Auger electron spectroscopy (AES)*

AES is a surface composition analysis technique that measures the energy of electrons emitted from the sample surface when it is bombarded with an electron beam. When incident electrons remove a core electron from a surface atom, the vacancy of the core state is filled by electron de-excitation from an outer shell electron. The relaxation energy is transferred to a third electron, the Auger electron. The kinetic energy of the emitted Auger electrons is a characteristic of the element and is independent of the incident electrons energy [54].

The detection limit for AES is about 0.1 atomic %, but it varies greatly from element to element. Quantitative analysis is difficult due to the low peak-to-background ratio. To improve the accuracy of the technique, a sensitivity factor is introduced to correct the measured peak intensities for each element. Depth profiles can be obtained by alternately sputtering with an inert ion beam and acquiring the Auger signal. Scanning Auger microscopy allows the sample to be mapped for selected elements [54].

In this study, AES was used to analyze the surface composition of the $B_{12}As_2$ epitaxial films produced. Also, depth profiles of composition throughout the whole film were acquired.

### *2.4.7 X-ray photoelectron spectroscopy (XPS)*

XPS is primarily used to analyze the elemental composition and chemical and electrical states of the elements in a material. Irradiating a sample with x-rays, electrons are ejected from the valence band. Measuring the kinetic energy and number of electrons gives the XPS spectra. XPS requires ultra high vacuum and are highly surface sensitive; the emitted photoelectrons originate from the upper 5-50Å of the sample. Generally surface treatment, e.g. ion beam sputtering, on the as-received samples, is required to remove surface contaminations.

The electron binding energy is influenced by its chemical surroundings, thus the chemical states of the bond can be determined. XPS is also a non-destructive method. Depth profiling is achieved by alternately sputtering with an inert ion beam and acquiring the XPS signal. The

detection limit for most of the elements is around 0.1% or 5 x $10^{19}$ atoms $cm^{-3}$[54]. XPS has been widely used in polymer, ceramics, heterogeneous catalyst, metals and alloys, semiconductors, nano-particles and biomaterials, etc [65]. In this study, XPS was used to analyze the surface composition of the $B_{12}As_2$ epitaxial films, as functions of process conditions.

### *2.4.8 Secondary ion mass spectroscopy (SIMS)*

SIMS is one of the most powerful and versatile analytical techniques for characterizing, dopant profiles of implanted and diffused layers in semiconductors. It can determine the trace elements and their concentration with a high sensitivity (to ppm levels).

SIMS is a destructive technique, removing the material from the sample by sputtering and analyzing the ions generated by a mass spectrometer. A time-of-flight SIMS (TOF-SIMS) was utilized in this research to measure the residual impurities and intentional dopant concentrations in the epitaxial $B_{12}As_2$ films. As shown in Figure 2.13, in SIMS, a primary ion beam impinges on the surface, sputtering and ejecting atoms, and ions from the sample. Commonly used primary ions are $Ar^+$, $Cs^+$, $O_2^+$, $Ga^+$, $Au_n^+$, $Bi_n^+$ and $C_{60}^+$. An electrical voltage is applied to the secondary ions (the sputtered material) for acceleration. The mass/charge ratio of different ions reaches the mass spectrometer sequentially, yielding a spectrum of all elements present [66].

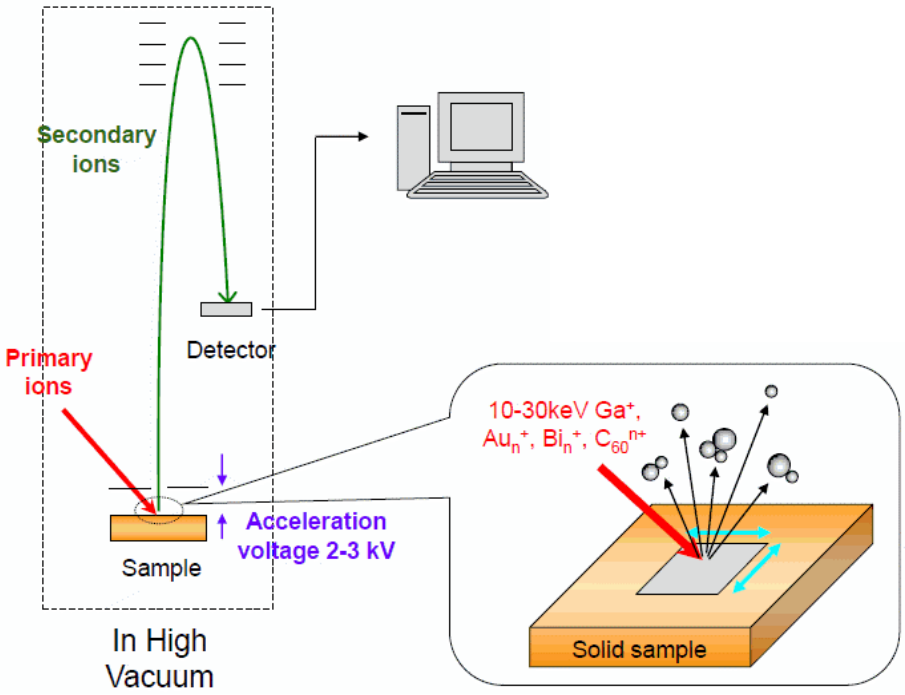


**Figure 2.13 Schematic of TOF-SIMS**

A major strength of SIMS is its ability to do quantitative depth profiling. The conversion of signal intensity to concentration, in principal, can be calculated knowing the primary ion beam current, the sputter yield, the ionization efficiency, the atomic fraction of the ion to be analyzed, and an instrumental factor [54]. However, in practice, some of these factors are poorly known. The common approach to solving this problem is to use a standard sample with a composition identical or similar to the matrices. Calibrated standards make the SIMS measurements more accurate.

In the present work, TOF-SIMS was applied to accurately measure the dopant (Si) and impurities (O, H and C) concentrations in $B_{12}As_2$ [64]. An implanted sample was prepared to serve as a calibration standard for subsequent measurements to obtain the absolute concentrations. An unintentionally doped $B_{12}As_2$ thin film was implanted with known concentrations of carbon, oxygen, hydrogen and silicon. A 25 keV $Bi^+$ beam was used for TOF-SIMS analysis and a 2keV $Cs^+$ beam was used for sputtering.

### *2.4.9 Hall effect measurement*

The charge carrier concentration and the mobility are two primary parameters representing the basic electrical properties of a semiconductor. Hall effect and resistivity measurements have been widely used to characterize the charge transport properties of semiconductors [54, 67, 68]. The Hall effect measurement is a relative simple and fast way to determine the majority carrier type and concentration of charge carriers in a semiconductor.

When an electric current flows through a semiconductor in a magnetic field, the magnetic field exerts a transverse force on the moving charge carriers which tends to push the positive and negative charges to opposite sides of the semiconductor. A build up of charge at the sides of the semiconductor will balace this magnetic influence, producing a measurable voltage between two sides of the semiconductor. This voltage is called the Hall voltage, $V_H$, and is depicted in Figure 2.14.

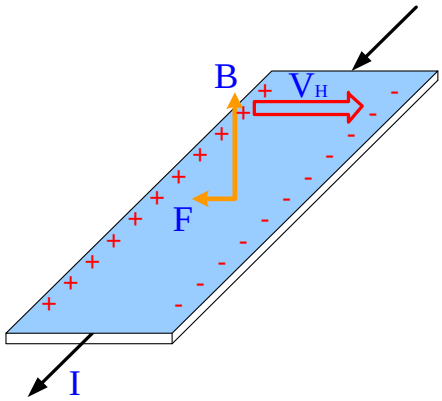


**Figure 2.14 Depiction of the Hall effect. B is the magnetic field , F is the Lorenz force, I is the current and $V_H$ is the Hall voltage.**

A commonly used configuration for resistivity and Hall-effect measurements is the Van der Pauw geometry [69, 70]. This geometry is applicable to samples of arbitrary shape with four small Ohmic contacts (point contact) on the periphery of the sample. In practice, there are two commonly used contact patterns utilizing Van der Pauw geometry: cloverleaf and square samples with small contacts on the corners, as illustrated in Figure 2.15. The cloverleaf geometry satisfies the requirement of point contacts and provides a large area for the formation of contacts. However, the process of sample preparation is complicated and difficult for brittle samples. In comparison, the square or rectangle configuration is easy to obtain.

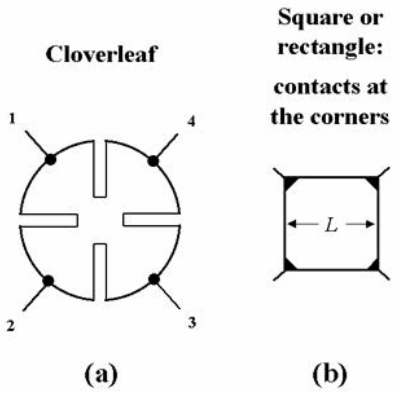


**Figure 2.15 Practical examples of the application of the Van der Pauw configuration for Hall effect measurement (a) cloverleaf, and (b) square or rectangle sample [54, 71]**

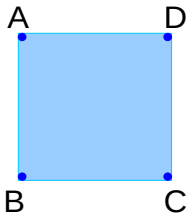


**Figure 2.16 A square sample with four point contacts A, B, C and D**

The free carrier concentration and mobility can be obtained based on the following theory [54]. Shown in Figure 2.16, for resistivity measurement, a dc current $I_{AB}$ is passed from contact A to contact B and the voltage between contacts C and D, $V_{CD}$ is measured. A characteristic resistance, based on van der Pauw theory, $R_{AB,\,CD}$ is defined

$$R_{AB,\,CD}= (V_D-V_C)/\, I_{AB} \tag{2-2}$$

Similary, we can define

$$R_{BC,AD}= (V_A-V_D)/\, I_{BC} \tag{2-3}$$

The characteristic resistances $R_{AB,\,CD}$ and $R_{AB,\,CD}$ should satisfy the following equation:

$$\exp\left(-\frac{\pi R_{AB,CD}\cdot t}{\rho}\right)+\exp\left(-\frac{\pi R_{BC,AD}\cdot t}{\rho}\right)=1 \tag{2-4}$$

where t is the thickness of the sample, and ρ is the resistivity. Therefore, the resistivity can be calculated by Eq. (2-4).

For Hall effect measurements, a dc current $I_{AC}$ is passed from contact A to contact C and the voltage between contacts B and D, $V_{BD}$ is measured. A characteristic resistance, based on van der Pauw theory, $R_{AC,\,BD}$ is defined

$$R_{AC,\,BD}= (V_D-V_B)/\, I_{AC} \tag{2-5}$$

Then, a uniform magnetic field $B$ is applied, perpendicular to the sample surface, and the above procedure repeated to obtain $R'_{AC,\,BD}$. The Hall coefficient, $R_H$, and thus the carrier concentration and mobility can be obtained by the following equations:

$$R_H = t\cdot(R'_{AC,BD}-R_{AC,BD})/B \tag{2-6}$$

$$p = 1/e\cdot\left|R_H\right| \tag{2-7}$$

$$\mu = \frac{R_H}{\rho} \tag{2-8}$$

where $e$ is the electron charge and $p$ is the carrier concentration.

If the Hall coefficient is negative, the majority carriers are electrons, if positive, the majority carriers are holes.

In this dissertation, we measured the electrical properties of $B_{12}As_2$ epitaxial films using this technique. Also we employ temperature variable Hall effect measurement to reveal the transport mechanism and thermal activation energies of charge carriers of the semiconductor for the first time.

## 2.5 Radioisotope Batteries

The demand for improved battery performance in durability and lifetime are increasing for consumer and military applications. Radioisotope batteries, e.g. alphavoltaics and betavoltaics have superior energy capacities and extraordinary long lifetime in comparison to traditional chemical batteries. As shown in Figure 2.17, the power density of batteries using alpha particles can be $10^4$~$10^6$ (for beta particles, $10^2$~$10^4$) higher than conventional chemical batteries, hydrogen conversion and photovoltaics [72]. Alpha-emitting radioisotopes have an advantage in power density of 1–2 orders of magnitude over beta-emitting isotopes with similar half lives; however, the advantage in power output is often negated by the greater rate of degradation caused by high energy alpha-particles. Thus, we will only review the betavoltaics here.

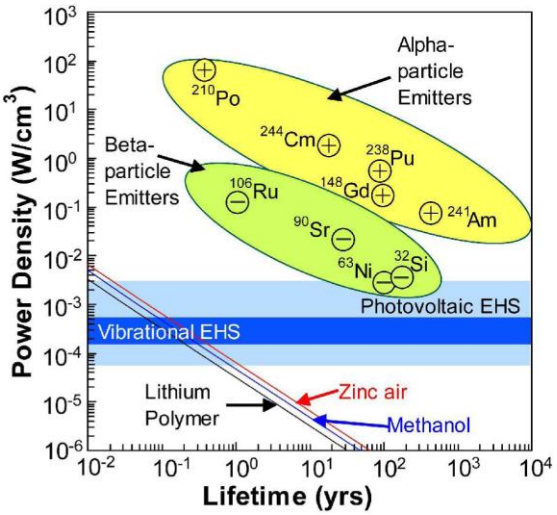


**Figure 2.17 Theoretical power density versus operating lifetime for various forms of electrochemical cells, energy harvesting and scavenging devices (EHS), and devices based on alpha- and beta-particle emitting radioisotopes [72].**

Betavoltaics, i.e. beta-cells, have a lifetime from 10 to 100 years, depending on the radiation source and the solid-state materials [73]. Such long-lived batteries can power remotely located, difficult to maintain environmental sensors. They also find applications in the biomedical field, such as cardiac pacemakers for heart patients and telemetry and monitor devices [74].

Beta particles are high energy electrons emitted from beta decay, when a neutron decays into a proton. The energy of beta particles ranges from 0.018 ($^{3}_{1}H$) to 16.4 MeV ($^{12}_{7}N$), depending on the radioactive sources [75]. A schematic of a simple beta cell based on $B_{12}As_2$ is depicting in Figure 2.18 [74, 76]. When the high energy beta particles passing through the semiconducting $B_{12}As_2$ layer a portion of the kinetic energy is lost to the lattice and the remainder creates electron-hole pairs. These electron-hole pairs can be effectively separated by the electrical field applied on a Schottky diode or a *p-n* junction, producing a current through this device.

However, the lifetime of beta cells is limited by accumulated radiation damage. As early as 1956, Rappaport *et al* [77] studied beta cells and the effects of radiation damage on Ge and Si *p-n* junctions. When high energy beta particles strike and pass through the semiconductor materials, Frenkel defects are created. Such defects serve as the recombination centers for electons and holes, reducing the power conversion efficiency. A Si beta cell bombarded by beta particles from a 50-millicurie $Sr^{90}$-$Y^{90}$ source degraded rapidly in 43 hours, much shorter than the half-life of the radioactive sources, which is 20 years. To avoid radiation damage, only very low energy radiation sources have been employed in current beta cells, such as $^{3}$H-5.7 keV, $^{147}$Pm-62 keV and $^{63}$Ni-67 keV [77, 78, 79]. Obviously, the energy density available in those low energy radiation sources is much lower, yielding low power output.

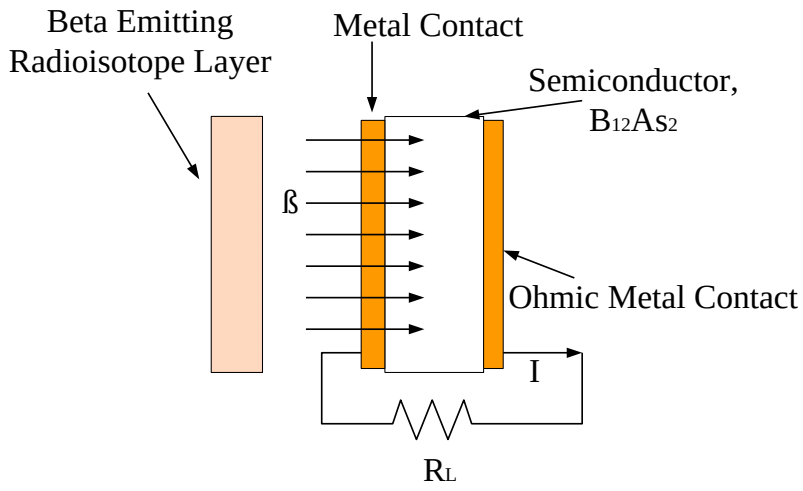


**Figure 2.18 A schematic of a planar betavoltaic cell. When beta particles with high energy bombard a semiconductor, electron-hole pairs are created. These electon-hole pairs are separated by the electrical field of the $B_{12}As_2$ Schottky diode. A current, *I*, is produced in this device.**

To reduce or eliminate the radiation damage and improve the device performance, semiconductor materials with high radiation tolerance are desired. Distinctively, icosaheral boron compounds, such as $B_{12}As_2$ and $B_{12}P_2$, have high radiation resistance due to their self-healing properties [33]. High resolution transmission electron microscopy images proved the absence of defect clusters or amorphization after radiation with 400 keV electrons of $10^{23}$ electrons/cm$^2$, a dose at which most metal borides degraded [33]. Therefore, beta cells made with $B_{12}As_2$ or $B_{12}P_2$ should have the unique advantage of using higher energy beta particle emitters, e.g. $^{90}$Sr-900 keV, as sources. Such devices are capable of producing more power for a wide range of applications. This is one motivation for conducting the research reported in this dissertation.

Besides the challenge of finding an alternative semiconductor which is highly resistant to radiation damage, cost and safety are the other concerns for the wide-scale applications of beta-cells and other radioisotope batteries [75, 77, 79]. Pre-requirements for wide-scale applications of beta cells include (1) both semiconductor and radioisotope source are abundantly available, (2) radiation is permanently sealed inside the battery, and (3) radioisotope batteries will not have too many regulatory restrictions. Under these requirements, beta cells are suited for devices such as GPS satellites, sensor data transmission, and military devices where cost is less of a concern [79, 80].

## 2.6 Neutron detectors

Neutron detectors with improved detection efficiencies are highly desirable since neutrons are a highly specific indicator of fissile materials. Currently, the standard neutron detectors are made from $^{3}$He, an isotope of helium. $^{3}$He is formed as a daughter product when tritium ($^{3}$H) decays, which was produce to be part of the trigger mechanism in nuclear bombs. However, the demand (65,000 L/year) of this isotope is far beyond its production (20,000 L/year) [81]. In addition, $^{3}$He tube based detectors are bulky, hard to configure and difficult to transport via air shipment. Thus, there is an urgent need to develop a new generation of solid state detectors that are not only more sensitive, but are more compact, operate on minimal power, and are low in cost.

There are three most commonly used elements in neutron detectors, $^{3}$He, $^{10}$B and $^{6}$Li. $^{10}$B has the second largest thermal neutron capture cross section, 3840 barns, orders of magnitude higher than most elements (typically ≤1 barn) [82]. The thermal neutron capture cross section of $^{3}$He and $^{6}$Li are also high, 5400 and 937 barns, respectively. Therefore, thin layers of $^{10}$B can absorb all incident thermal neutrons (100% efficiency). When a $^{10}$B atom captures a neutron, it undergoes a nuclear reaction that produces energetic Li ions and alpha particles [82]:

(1) $^{10}B + n \rightarrow {}^{7}Li\ (0.84\ MeV) + {}^{4}He(1.47\ MeV) + \gamma(0.48\ MeV)$ (94%)

(2) $^{10}B + n \rightarrow {}^{7}Li\ (1.02\ MeV) + {}^{4}He(1.78\ MeV)$ (6%)

For each neutron captured, approximately 1.5 x $10^{6}$ electron-hole pairs can be produced as the energetic $^{7}$Li and $^{4}$He ions pass through a semiconductor material. This charge is sufficiently large to be detected directly without further amplification. Thus, a thermal neutron detector could be based on a boron-rich semiconductor Schottky, *pn*, or *pin* diodes. Boron-based semiconductor devices have the potential to be 100% efficient in detecting thermal neutrons. In addition to their high efficiency, like most solid state devices, boron-based semiconductor devices can be robust, compact, and long-lived.

Currently, solid-state neutron detectors based on boron compounds have three configurations. (1) A boron conversion layer on top of a silicon *pn*-junction diode, as shown in

Figure 2.19 (a). Li ions and α particles produced in the boron layer generate electrons and holes in the semiconductor (left). Signal is lost if the neutron does not react in the boron layer (middle) or if the ions created do not reach the semiconductor (right). (2) Alternating B and Si pillars created on a substrate, shown in

Figure 2.19 (b). The signal is improved over a simple B conversion layer, since the energetic ions have a shorter distance to travel through the boron to reach the semiconductor. Nevertheless, some signal is still lost by energy absorption from the ions in the matrix [83, 84, 85]. (3) A *pn*-junction made from boron-rich semiconductors, as shown in

Figure 2.19 (c). The efficiency of solid state neutron detectors can be greatly improved by combining neutron capture and charge collection layers together in a single material.

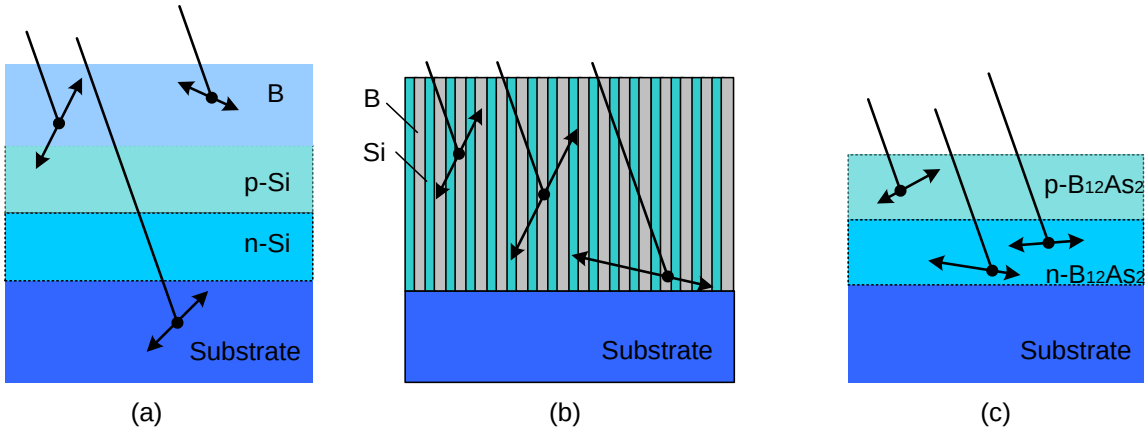


**Figure 2.19. Schematics of three types of boron-based solid-state neutron detectors: (a) boron conversation layer on top of a *p-n* junction made of Si, (b) pillared structure with alternating columns of B and Si, (c) combined conversion semiconductor device**

Several attempts to make neutron detectors from boron-based semiconductors have been reported in the literature [86-88]; however, the success of these studies was limited, as the device efficiency is quite low. Universally, this can be attributed to the material's disordered polycrystalline nature and high residual impurities concentrations.

$B_{12}P_2$ and $B_{12}As_2$ semiconductors are good candidates for solid-state neutron detectors because of several clear advantages over other boron-rich compounds. In $B_{12}P_2$ and $B_{12}As_2$, hole mobilities are relatively high, on the order of 50-100 $cm^2V^{-1}s^{-1}$ compared to the low hole mobilities of boron carbide and β-boron (<1 $cm^2V^{-1}s^{-1}$) [31]. The mobility is sufficiently high that electrons and holes created by absorption of thermal neutrons of $^{10}B$ can reach the external metal contacts of the device. This is essential for good charge collection efficiencies in neutron detectors. High mobility can only be achieved on high quality crystalline materials.

Both $B_{12}P_2$ and $B_{12}As_2$ can self-heal from radiation damage. A distinguishing feature of icosahedral boron compounds is that they are highly resistant to radiation damage. Additionally,

the wide bandgap (>3 eV), high thermal stability, the ability to dope of $B_{12}P_2$ and $B_{12}As_2$ are all benefits for the efficiency and resolution of neutron detection. Therefore, $B_{12}P_2$ and $B_{12}As_2$ are promising semiconductors for high efficiency, high resolution neutron detectors. The goal of this research was to produce single crystalline $B_{12}As_2$ with controlled resistivity, low defects and low impurities concentrations for neutron detectors and beta cells.

## Reference


[1] D. Emin, *Phys. Today*, 55, January (1987)

[2] D. Emin, *J. Solid. State. Chem.*, 177, 1619 (2004)

[3] D. Emin and T. L. Aselage, *J. Appl. Phys.*, 97, 013529 (2005)

[4] S. Bakalova, Y. Gong, C. Cobet, N. Esser, Y. Zhang, J. H. Edgar, Y. Zhang, M. Dudley, and M. Kuball, *Phys. Rev. B*, 81, 075114 (2010)

[5] R. H. Wang, D. Zubia, T. O'Neil, D. Emin, T. Aselage, W. Zhang and S.D. Hersee, *J. Electron. Mater.*, 29, 1304 (2000)

[6] R. Nagarajan, Z. Xu, J. H. Edgar, F. Baig, J. Chaudhuri, Z. Rek, E. A. Payzant, H. M. Meyer, J. Pomeroy and M. Kuball, *J. Cryst. Growth* , 273, 431 (2005)

[7] X. Zhou, J. H. Edgar and S. Speakman, *J. Cryst. Growth*, 293, 162 (2006)

[8] Y. Zhang, H. Chen, M. Dudley, Y. Zhang, J. H. Edgar, Y.Gong, S. Bakalova, M. Kuball, L. Zhang, D. Su, K. Kisslinger, Y. Zhu, *Mater. Res. Soc. Symp. Proc.* 1246, B04-2 (2010)

[9] C.E. Whiteley, Y. Zhang, Y. Gong, S. Bakalova, A. Mayo, J.H. Edgar, M. Kuball, *J. Cryst. Growth*, 318, 1, 553(2011)

[10] G.V. Tsagareishvili and F.N. Tavadze, *Prog. Cryst. Growth and Charact. Mater.*, 16, 341 (1988)

[11] P. Yang, and T. L. Aselage, Proc. 11th Int. Symp. Boron, Borides and related Compounds, Tsukuba, 1993, JJAP Series 10, 130 (1994)

[12] J. A. Boyer, U.S. Patent, 2,124,538, (1938)

[13] T. L. Aselage, S. B. Vandeusen and B. Morosin, *J. Less-Common Metals*, 166, 29 (1990)

[14] Akira Masago,Koun Shirai, and Hiroshi Katayama-Yoshida, *Phys. Rev. B* 73,104102-1(2006).

[15] B. Morosin, A. W. Mullendore, D. Emin, and G. A. Slack, American Inst. of Phys., Conference Proceedings, 86, 70 (1986)

[16] T. L. Aselage, D. R. Tallant, and D. Emin, *Phys. Rev. B.* 56, 3122 (1997)

[17] G. A. Slack, T. F. McNelly, and E. A. Taft, *J. Phys. Chem. Solids*, 44, 1009 (1983)

[18] H. K. Clark and J. L. Hoard, *J. Am. Chem. Soc.*, 61, 11, 2115 (1943)

[19] F. Thevenot, *J. Eur. Ceram. Soc.* 6, 205 (1990)

[20] N.N. Greenwood and A. Earbsgaw, Chemistry of the Elements, edited by Thomas E. Albrecht-schmitt, Pergamon Press, Oxford, UK, (1984).

[21] H. Lee and R. F. Speyer, *J. Am. Ceram. Soc.*, 86, 9, 1468-73 (2003)

[22] D. Li, and W. Y. Ching, *Phys. Rev. B*, 52, 17073 (1995)

[23] W. Y. Ching, and D. Li, *Phys. Rev. B*, 57, 3737 (1998)

[24] F. Perrot, *Phys. Rev. B*, 23, 2004 (1980)

[25] R. A. Burmeister, and P. E. Greene, *Bull. Amer. Phys. Soc.*, 10, 1184 (1965)

[26] S. Lee, J. Mazurowski, G. Ramseyer, P. A. Dowben, *J. Appl. Phys.*, 72, 10, 4925 (1992)

[27] F. H. Horn, *Appl. Phys.* 30, 1611 (1959).

[28] Z. Xu, J. H. Edgar, D.C. Look, S. Baumann, R. J. Bleiler, S. H. Wang and S. E. Mohney, *J. Appl. Phys.*, 101, 053710 (2007)

[29] Y. Kumashiro, H. Yoshizawa, and K. Shirai, Proc. 11th Int. Symp. Boron, Borides and Related Compounds, Tsukuba, 1993, JJAP Series 10, 166 (1994)

[30] A. O. Sezer and J. I. Brand, *Mater. Sci. Eng. B* 79, 191 (2001)

[31] O. A. Golikova, *Chemtronics*, 5, 3 (1991).

[32] Y. Zhang, and J. H. Edgar, unpublished, data from chapter 4 in this dissertation

[33] D. Emin, *J. Solid State Chem.*, 179, 2791 (2006)

[34] T. Stoto, L. Zuppiroli, J. Pelissier, *Radiat. Eff. Defects Solids* 90, 161 (1985)

[35] T. Stoto, N. Houssean, L. Zuppiroli, B. Kryger. *J. Appl. Phys.* 68, 3198 (1990).

[36] M. Carrard, D. Emin, L. Zuppiroli, *Phys. Rev. B*, 51, 11270 (1995).

[37] F. V. Williams, and R. A. Ruehrwein, *J. Am Chem. Soc.*, 82, 1330 (1960)

[38] S. M. Ku, *J. Electrochem. Soc.*, 113, 813 (1966)

[39] T. L. Aslage, *Mat. Res. Soc. Symp. Proc.*, 97, 101(1987)

[40] T. L. Chu, and A. E. Hyslop, *J. Electrochem. Soc.*, 121, 412 (1974)

[41] L. A. Correia, R. C. Van Oort, and P. J. Van der Put, *React. Solids*, 2 , 203(1986)

[42] M. Hirayama, and K. Shohno, *Jpn. J. Appl. Phys.*, 12, 1960(1973)

[43] H. Chen, G. Wang, M. Dudley, Z. Xu, J. H. Edgar, T. Batten, M. Kuball, L. H. Zhang and Y. M. Zhu, *Mater. Res. Soc. Symp. Proc.*, 1069 (2008)

[44] R. Schmechel, H. Werheit, V. Kueffel and T. Lundstrom, *Proc., Intl. Conf. Thermoelectrics* , 26, 219(1997)

[45] H. Werheit, Material Science of Carbides, Nitrides, and Borides, 65 (1999)

[46] A. A. Berezin, O. A. Golikova, M. M. Kazanin, T. Khmidov, M. M. Mirlin, A. V. Petrov, A. S. Umanov, V. K. Zaitsev, *J. Non-Cryst. Solids*, 16, 237 (1974)

[47] O. A. Golikova, *Phys. Status. Solidi A*, 51, 11 (1979)

[48] O. A. Golikova, *MRS. Symp. Proc.*, 97 (1987)

[49] H. Werheit, Electronic Transport in Boron-rich Solids, Springer, Netherland (2005)

[50] K. Kirihara, Y. Shimizu, Y. Yamada, F. Esaka, T. Sasaki, N. Koshizaki, H. Yamamoto, S. Shamoto, and K. Kimura, *Appl. Phys. Lett.*, 97, 212105 (2010)

[51] I. A. Howard, C. L. Beckel, D. Emin, *Phys. Rev. B*, 35, 2929(1987)

[52] D. Emin, Proc. 10th Int. Symp. Boron, Borides and Related Compounds, 65 (1987)

[53] R. Schmechel and H. Werheit, *J. Phys.: Condens. Matter*, 8, 7263 (1996)

[54] D. K. Schroder, Semiconductor Material and Device Characterization, New Jersey: John Wiley & Sons, (2006)

[55] W. R. Runyan and T. J. Shaffner, Semiconductor Measurements and Instrumentation, New York: McGraw-Hill, (1998)

[56] H. Butt, B. Cappella, M. Kappl , *Surf. Sci. Rep.* 59, 1 (2005).

[57] K. Swanson, Epitaxial Growth of Silicon Carbide on Low Angle Silicon Carbide using Methyltrichlorosilane Chemical Vapor Deposition, Master thesis, 22 (2007)

[58] D. J. Gardiner, Practical Raman Spectroscopy, Springer-Verlag. (1989)

[59] Azároff, L. V.; R. Kaplow, N. Kato, R. J. Weiss, A. J. C. Wilson, R. A. Young. X-ray Diffraction, McGraw-Hill, (1974)

[60] M. Dudley and X. Huang, *Mater. Sci. Forum* 338, 431 (1998)

[61] X. R. Huang, M. Dudley, W. M. Vetter, *J. App. Crystallogr.*, 32, 516 (1999)

[62] M. Dudley, X. R. Huang and W. Huang, *J. Phys. D: App. Phys*., 32, A139 (1999)

[63] X. R. Huang, M. Dudley, J. Y. Zhao, *Philosophical Transactions of the Royal Society of London. A*, 357, 2659 (1999)

[64] Y. Zhang, Growth Mechanism and Defect Structures of $B_{12}As_2$ Epilayers Grown on 4H- and 6H-SiC Substrates, PhD Dissertation (2011)

[65] J. Riviere, Handbook of Surface and Interface Analysis Methods for Problem-Solving, 2nd Ed. Boca Raton FL: Taylor and Francis, (2009)

[66] Z. Zhu, *A Brief Introduction of ToF-SIMS in EMSL*, tutorial presentation, 2010.

[67] P. Blood and J.W. Orton, Electrical Characterization of Semiconductors: Majority Carriers and Electron States, London: Academic Press, (1992)

[68] Look, D.C., Electrical characterization of GaAs Materials and Devices, New York: Wiley, (1989)

[69] L.J. van der Pauw, *Philips Res. Rept.*, 13, 1(1958)

[70] L.J. van der Pauw, *Philips Tech. Rev.*, 20, 220(1958)

[71] The van der Pauw technique and Hall effect measurement, online information: http://www.nist.gov

[72] C. D. Cress, B. J. Landi, and R. P. Raffaelle, *Transactions on Nucl. Sci.* 55, 1736 (2008)

[73] E. M. Baum, H. D. Knox, T. R. Miller, Nuclides and Isotopes; Chart of the Nuclides, 16th Ed. Lackheed Martin, (2002)

[74] M. M. El-Wakil, Nuclear Energy Conversion, Intext Educational Publishers, (1971)

[75] K. E. Bower, Y. A. Barbanel, Y. G. Shreter and G. W. Bohnert, Polymers, Phosphors, and Voltaics for Radioisotope Microbatteries, Boca Raton: CRC Press, (2002)

[76] T. L. Aselage, D. Emin, US Patent 6479919, (2002)

[77] R. Rappaport, J. Loferski, and E. G. Linder, *RCA Rev.* 17, 100 (1956)

[78] T. Kosteski, N. P. Kherani, F. Gaspari, S. Zukotynski, W. T. Shmaayda, *J. Vac. Sci. and Technol. A*, 16, 893 (1998)

[79] C. Cress. Effect of Ionizing Radiation on Nano-materials and III-V Semiconductors. PhD Dissertation, (2008)

[80] C. Whiteley, Advanced Crystal Growth Techniques with III-V Boron Compound Semiconductors, PhD Dissertation, (2011)

[81] M. Wald, Shortage Slows a Program to Detect Nuclear Bombs, online information, http://www.nytimes.com/2009/11/23/us/23helium.html (2009).

[82] N. Tsolfanidis, Measurement and Dectection of Radiation, 2nd E., Bristol: Taylor & Francis, (1995)

[83] D. S. McGregor, S. M. Verno, and H. K. Gersch, *IEEE Trans. on Nucl. Sci.*, 47, 1364 (2000)

[84] D. S. McGregor, T. C. Unruh, and W. J. McNeil, *Nucl. Instrum. Methods. Phys. Res.* , 591, 530 (2008)

[85] D. S. McGregor, and J. K. Shultis, *Nucl. Instr. Meth. Phys. Res.* A, 517, 180 (2004)

[86] J. D. Buckley and J. A. Cooley, *Mater. Sci. Res.* 5, 547 (1971)

[87] L. Vel. G. Demazeau, and J. Etourneau, *Mater. Sci. Eng.* B, 10, 149 (1991)

[88] Y. Kubata, K. Watanabe, and T. Taniguchi, *Jpn J. Appl. Phys.*, 46, 311 (2007)

[89] Scanning Electron Microscopy, online information, http://en.wikipedia.org/wiki/Scanning_electron_microscope

# Chapter 3 - Experimental Procedures

## 3.1 CVD system, substrates and growth conditions

### *3.1.1 The CVD system*

The CVD system utilized in this research to produce epitaxial $B_{12}As_2$ thin films and nanowires consists of a gas manifold, a cold wall quartz reactor, an induction heating system, valve controllers, a toxic gas monitor and exhaust/pressure control. Figure 3.1 is the process flow diagram for this CVD reaction system. The gas manifold controls the flow rates and sequence of the reactants, dopants and carrier gas entering the reactor. The induction heater could heat up the susceptor which was contained in the quartz reactor, to the designated experimental temperatures. The system is purged and evacuated by mechanical and turbomolecular pumps to minimize the impurities from ambient gases (especially oxygen). The system pressure can be controlled at a constant pressure by a butterfly valve and controller.

The reactants, arsine ($AsH_3$) and diborane ($B_2H_6$), are highly toxic gases. The TLV value of arsine on the basis of a 8h/day, 40h/week work schedule is 0.05ppm and that of diborane is 0.1ppm. Threshold Limit Value (TLV) of a chemical substance is defined as a level to which it is believed a worker can be exposed day after day for a working lifetime without adverse health effects. Thus, many precautions have been taken so they are safely handled. First, the reactants were supplied as mixtures with hydrogen as 1% $AsH_3/H_2$ and 1%$B_2H_6/H_2$. These diluted mixtures were less toxic than the pure gases. Second, a sensitive toxic gas monitor was used to detect and measure the concentrations of $AsH_3$ and $B_2H_6$ at these points: the point right after the reactor, the outlets of the exhaust and fume hood, ensuring no toxic gases were present outside of the system. The detection limit of the monitor is 0.1 ppb. Third, two tanks of activated carbon were used to absorb the residual reactant gases, $AsH_3$ and $B_2H_6$, so they were not exhausted to the hood. Fourth, the system was checked for leaks before opening the toxic gases for the first time. Lastly, the operator used a self-contained breathing apparatus when opening the toxic gas cylinders for the first time. Figure 3.2 displays the actual CVD reactor.

The process conditions employed to produce $B_{12}As_2$ thin films were as follows. $AsH_3$ and $B_2H_6$ were the reactant gases. 0.01% $SiH_4$ diluted in $H_2$ was used as the doping gas. Their flow

rates were varied during different experiments. Palladium membrane purified $H_2$ was the carrier and purge gas during the deposition. The flow rate of $H_2$ was kept at 3.5 SLM.

A tantalum carbide-coated susceptor was utilized to hold and heat the substrate. The substrate temperature was monitored by a thermocouple. The thermocouple was calibrated by melting Si and comparing the measured temperature with the Si melting point. The errors between the measured and actual temperatures were $\pm 1$ ℃.

SiC was the main substrate used in this research. Before deposition, it was cleaned by the following procedure to remove the dust, grease and other surface contaminations. The substrates were placed in a beaker with trichloroethylene (TCE) for 5 minutes and scrubbed with paper wipes. Then the substrates were sequentially rinsed with acetone and methanol in the ultrasonic bath for 5 minutes. Lastly, they were rinsed with deionized water and blown dry with nitrogen.

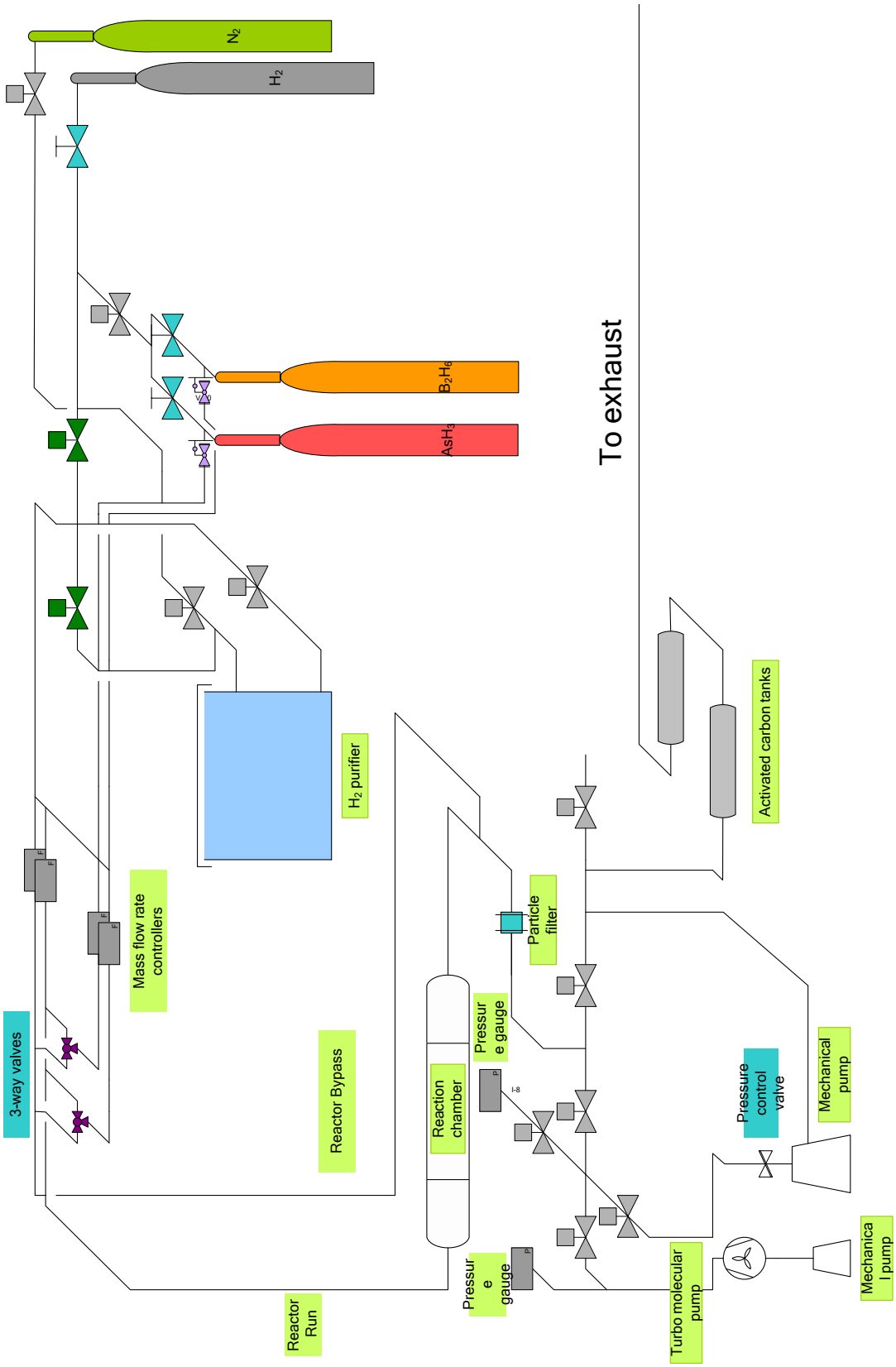


**Figure 3.1 The process flow diagram for the CVD system**

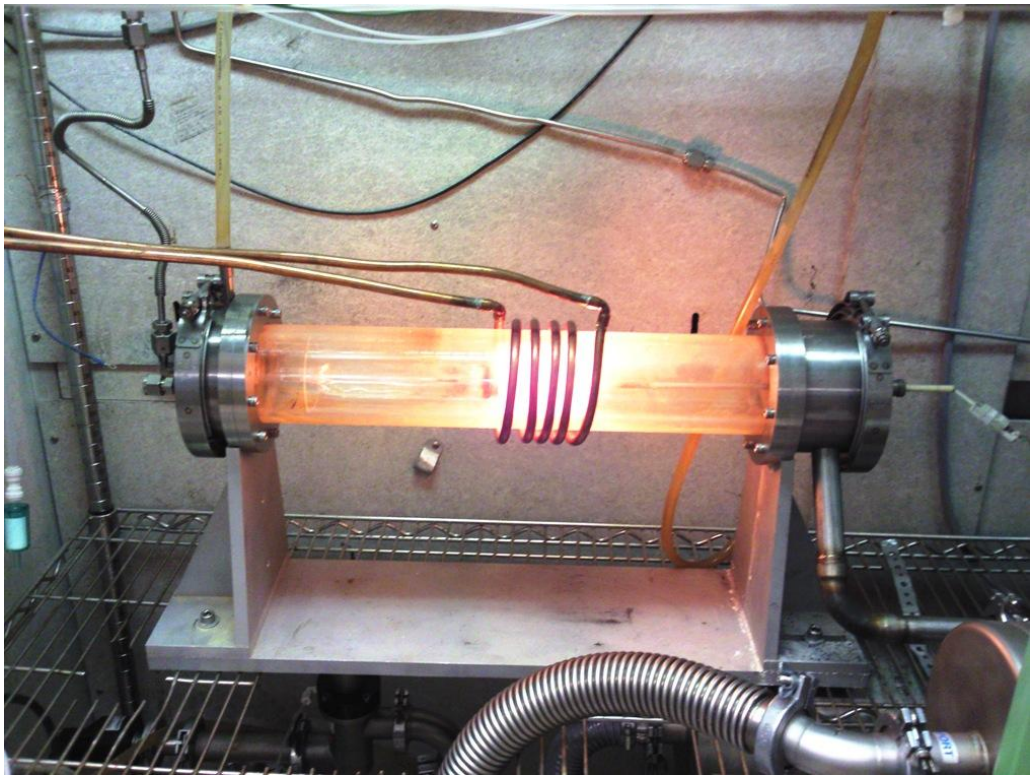

**Figure 3.2 The quartz reactor in the CVD system during reaction**

### *3.1.2 Substrates and growth conditions of heteroepitaxy*

Different polytypes and orientations of SiC exhibit different surface structures, which will influence $B_{12}As_2$ nucleation and its ultimate crystal quality. Thus, five substrates were utilized in this study to evaluate the effect of substrate on the crystal quality: on-axis *c*-plane 6H-SiC, on-axis *c*-plane 4H-SiC, *c*-plane 4H-SiC with 7 °off towards [1-100], *c*-plane 4H-SiC with 4 ° off towards [1-100] and on-axis *m*-plane 15R-SiC.

All the films were deposited at a temperature range of 1200-1400 ℃, and a total pressure of 100 torr. The flow rates of $B_2H_6$ and $AsH_3$ were varied from 40 to 80 sccm and 20 to 400 sccm, respectively. Si doping was achieved by adding a certain amount of $SiH_4$ simultaneously during epitaxy. The flow rate varied from 10 sccm to 90 sccm to achieve different dopant concentrations. Before depositing $B_{12}As_2$, the substrate was *in situ* etched in hydrogen at 1650 ℃ for 15 min to remove the polishing scratches on the SiC and to attain an atomically smooth surface.

### *3.1.3 Substrates and growth conditions of nanowires*

The substrates utilized to produce $B_{12}As_2$ nanowires include (1) a Si wafer with a 20 nm Ni coating, (2) a Si wafer with 12 nm thick Ni dots of diameters of 200 μm, and (3) platinum powder randomly dispersed on SiC wafer. All the nanowires were deposited at a temperature range of 700-1200 ℃, and a total pressure of 100 torr. The flow rate of $B_2H_6$ and $AsH_3$ were fixed at 40 and 400 sccm, respectively.

## 3.2 Hall effect measurement

The resistivity measurements utilize Van der Pauw geometry; square samples with four point contacts at corners. First of all, ohmic contacts to the $B_{12}As_2$ are required to obtain accurate measurement of electrical properties by Hall effect. For most field variable Hall effect measurements, four points indium contacts were soldered to the $B_{12}As_2$. The linear I-V curves confirmed the formation of ohmic contacts. However, indium is not suitable for high temperature measurement duo to its low melting point (156.5 ℃). Therefore, for temperature variable measurement, we choose Cr/Pt contacts. They were formed by depositing 50nm Cr and 100nm Pt via e-beam evaporation, followed by annealing at 600 ℃ for 10 minutes in an argon ambient.

Prior to each measurement, I-V curves between contacts pairs were measured to ensure ohmic contacts were formed. For field variable measurements, the magnetic field was varied from 500 to 8000 Gauss with a step of 500 Gauss. Measurements were taken at both positive and negative magnetic fields and the average value can minimize the test errors that were dependent on magnetic fields. For films grown on semi-insulating SiC substrates, we obtain the resistivity, mobility, carrier type and concentration directly. However, for films grown on n-type SiC substrates, we need to consider the effect of carriers in the substrates. Using the field variable Hall effect results, and a software named QMSA, we could separate results from different charge carriers and thus obtain the mobility and carrier concentrations of the $B_{12}As_2$ epilayer.

Temperature dependent Hall effect measurements provided information of the transport mechanism and thermal activation energies of charge carriers. In those measurements, the temperature was varied from 300 to 500K or 77 to 293 K for different tests. The magnetic field was fixed at 6000 Gauss. The injected current was usually set between 100 nA to 1 μA.

# Chapter 4 - Heteroepitaxy and Characterization of Icosahedral Boron Arsenide ($B_{12}As_2$) on SiC Substrate

## 4.1 Introduction

$B_{12}As_2$ is a semiconductor with a wide bandgap ($E_g$=3.2eV at room temperature) [1], similar to SiC, AlN, GaN and ZnO. Distinguishing it from other semiconductors is its extraordinary resistance to radiation damage, a consequence of its unique structure and bonding configurations [2, 3, 4]. Vacancies and interstitials caused by radiation tend to spontaneously recombine due to strong Coulombic attractions between positive boron ions and negative degraded icosahedra, in a process referred to as self-healing [2, 3, 5-8]. Such a semiconductor could be useful in electronic devices that operate in a high irradiation environment. One such device is the betavoltaic cell, a device which directly converts nuclear energy from radioisotopes to electrical power [5-9]. Gong *et al* [9] demonstrated a possible device structure, a heterojunction based on $B_{12}As_2$ and SiC. In the past, the performance of Si and Ge betavoltaics, i.e. beta cells, rapidly degraded from radiation damage, hindering their development. As a semiconductor that can self-heal from radiation damage, $B_{12}As_2$, can maintain its electrical properties for times comparable with the half life of the nuclear source and may make betavoltaic cells feasible.

Previous studies demonstrated that chemical vapor deposition (CVD) is successful at producing high-purity $B_{12}As_2$ thin films on Si and SiC substrates [10-14]. The crystalline quality of $B_{12}As_2$ thin films was better on SiC than Si because the in-plane lattice parameter of the basal plane of SiC (3.080 Å) is nearly half that within the (111) plane of $B_{12}As_2$ (6.149 Å) [11], resulting in a closer lattice constant match. In addition, the higher thermal stability of SiC over Si reduces the propensity for film-substrate reactions. However, structural variants, such as rotational twins, were observed in the epitaxial $B_{12}As_2$ films on on-axis (0001) 6H-SiC; these are expected to detrimentally affect its electrical properties and device performance.

The goal of this research was to establish pathways to reduce the structural variants and improve the crystal quality of $B_{12}As_2$ epitaxial films grown on the SiC substrates by CVD. The major parameters affecting the crystal quality studied included substrate polytypes and orientations, growth temperatures and reactants (boron and arsenic) ratios in the feed. Surface

and interface morphologies, crystal out-plane and in-plane orientations, defects and strain levels, and charge carrier mobility were characterized to evaluate the effects of those parameters on the crystal quality. The ultimate goal of this research was to fabricate electronic devices based on high quality $B_{12}As_2$ films.

Structural variants arise because there are several ways to match the rhombohedral structure $B_{12}As_2$ on the (0001) plane of hexagonal structure SiC heteroepitaxially. The symmetric step-terrace structure on the *c*-plane, i.e. (0001) plane, 6H-SiC surface after hydrogen etching provides two equivalent nucleation sites for $B_{12}As_2$ to adopt. Both theoretical predictions and experimental observations [15, 16] confirm the presence of twins after hydrogen etching of the substrate and $B_{12}As_2$ film deposition. For the various polytypes of SiC- for instance 4H-SiC, 6H-SiC and 15R-SiC- different step-terrace structures (exposed facets, step heights, and terrace widths) form depending on the polytype, and crystallographic plane and misorientations from the major planes, including the magnitude of the misorientation and the tilt direction.

The crystal planes of the SiC substrates in a hexagonal cooridinate are illustrated in Figure 4.1(a) and (b). If a wafer is sliced from the boule with the surface normal along the [0001] direction, it is an on-axis (0001) 4H-SiC substrate (Figure 4.1(b)). When the surface normal has an "a" degree tilt towards the [1-100] direction, the resulting wafer is (0001) 4H-SiC with a ° off-axis towards [1-100], as depicted in Figure 4.1(c). Similarly, if the surface normal has a "b" degree tilt towards the [11-20] direction, the resulting wafer is (0001) 4H-SiC with b ° off-axis towards [11-20] (Figure 4.1(d)).

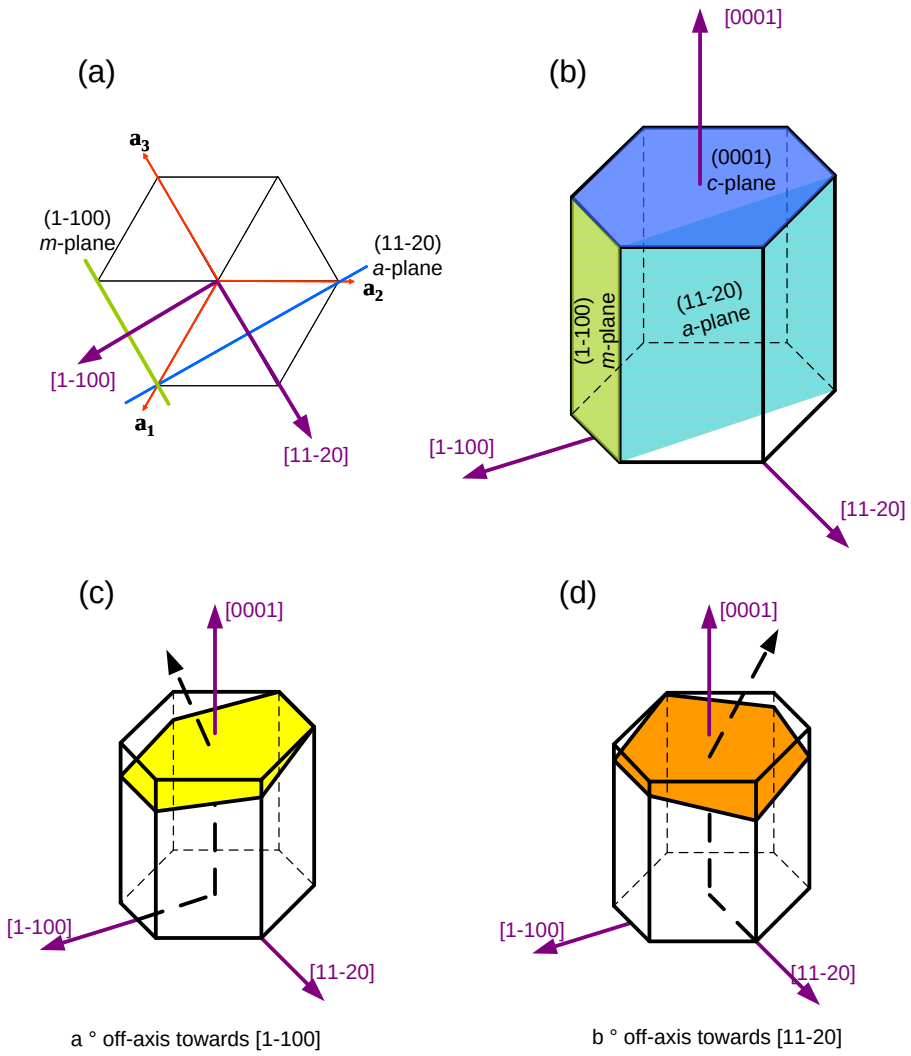


**Figure 4.1 Illustration of the tilt directions of the misorienations from major crystal planes. (a) Th projection of *a*-plane and *m*-plane in a hexagonal coordinate on the (0001) plane; (b) *a*-plane, *c*-plane and *m*-plane in a hexagonal coordinate; (c) (0001) plane with a ° off-axis towards [1-100]; (d) (0001) plane with b ° off-axis towards [11-20]**

In previous studies, $B_{12}As_2$ films were grown on on-axis *c*-plane 6H-SiC, off-axis 6H-SiC with 3.5 ° offcut towards [11-20] and *m*-plane, i.e. (1-100), 6H-SiC, a high density of twins was observed. However, films grown on *m*-plane 15R-SiC and 4H-SiC with 7 ° offcut towards [1-100], were twin-free [18, 19]. In the present study, we hypothesized a slight off-axis towards [1-100] created asymmetric regular step-terrace surface structures on the (0001) 4H-SiC substrates, yielding twin-free $B_{12}As_2$ epitaxial layers.

*c*-plane 4H-SiC, *c*-plane 6H-SiC and *m*-plane 15R-SiC with or without misorientations were employed as substrates for $B_{12}As_2$ growth, to determine pathways to reduce or eliminate the twins, leading to improved film quality and ultimately device performance. The film quality was assessed by x-ray diffraction techniques and electrical property measurements. Lastly, the impact of the B/As reactant ratio on the film composition was also examined.

## 4.2 Experimental procedure

$B_{12}As_2$ films were synthesized via CVD in an inductively heated horizontal quartz reactor, employing 1% $B_2H_6$ in $H_2$ and 1% $AsH_3$ in $H_2$ as source gases. The substrate was held inside a hollow tantalum carbide-coated graphite susceptor. The carrier gas was purified hydrogen with a constant flow rate of 3.5 SLM. All the films were deposited in a temperature range of 1200-1400 ℃, and a total pressure of 100 torr. The flow rate of the reactant gas $B_2H_6$ was varied from 40 to 80 sccm and that of $AsH_3$ was varied from 20 to 400 sccm. To remove the polishing scratches from the SiC and to attain an atomically smooth surface, before deposition of $B_{12}As_2$, the substrate was *in situ* etched in hydrogen at 1650 ℃ for 15 min.

Five substrates were utilized in this study: on-axis *c*-plane 6H-SiC, on-axis *c*-plane 4H-SiC, *c*-plane 4H-SiC with 7 ° off-axis towards [1-100], *c*-plane 4H-SiC with 4 ° off-axis towards [1-100] and on-axis *m*-plane 15R-SiC. Note that a misorienting tilt in the [1-100] direction is relatively unusual; tilting toward the [11-20] direction is the most common direction provided by SiC substrate vendors. Except for the on-axis *c*-plane 6H-SiC, all the other substrates were conductive, doped by nitrogen, with a conductivity on the order of $10^2$/ohm cm. The on-axis *c*-plane 6H-SiC was semi-insulating with a conductivity of approximately $10^{-3}$/ohm cm.

The surface morphologies were characterized by optical and scanning electron (SEM) microscopes. Synchrotron white beam x-ray topography (SWBXT) was carried out to determine the in-plane orientation of the epilayer. The crystal quality was evaluated by Raman spectroscopy. X-ray rocking curves of the (0003) plane were employed to reveal the epitaxial $B_{12}As_2$ film quality and defect densities. The electrical properties of the $B_{12}As_2$ films were assessed by Hall effect measurements over the temperature range of 300-500K at 5000 Gauss. Ohmic contacts to the $B_{12}As_2$ were formed by depositing 50 nm Cr and 100 nm Pt via e-beam evaporation, followed by annealing at 600 ℃ for 10 minutes in an argon ambient [9, 17].

Auger microanalysis of the sample compositions was performed at the High Temperature Materials Laboratory at Oak Ridge National Laboratory, using a Phi 680 Scanning Auger Nanoprobe. The primary electron beam was provided by a field emission source operated at a beam energy of 20 kV and beam current of 10 nA. This probe beam was focused to a spot size of ~20 nm and the Auger electrons emitted from the sample were detected using a cylindrical mirror analyzer. X-ray photoelectron spectroscopy was carried out using Thermo Scientific K-alpha spectrophotometer at the Shared Research Equipment (SHaRE) User Facility at the Oak Ridge National Laboratory. A spot size of 400 microns (maximum allowable) was used to scan the surface of the samples so as to account for surface variations and obtain an averaged signal.

## 4.3 Results and discussion

### *4.3.1 $H_2$ in-situ etching*

As-received SiC substrates have many particles and polishing scratches as shown in Figure 4.2 (a). The particles can be removed by classic solvent cleaning methods, but the polishing scratches are difficult to remove via wet etching due to their stable chemical properties. Hence high temperature, dry hydrogen etching was used, as has been widely employed in other studies, to remove the scratches [18, 19, 20]. Clear step-terrace structures were observed on the 4H-SiC substrate after hydrogen etching at 1650℃ for 15 minutes, as shown in Figure 4.2 (b). This process provides a step-terrace structure for subsequent epitaxial growth.

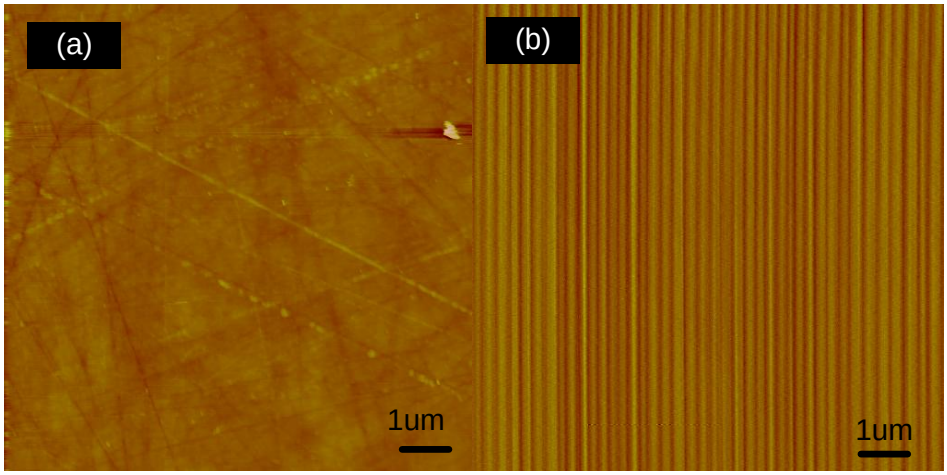


**Figure 4.2 AFM images of on-axis (0001) 4H-SiC substrate (a) before $H_2$ etching (b) after $H_2$ etching.**

### *4.3.2 Crystal identification and orientation*

A typical x-ray diffraction pattern of an epitaxial $B_{12}As_2$ film grown on (0001) 4H-SiC is shown in Figure 4.3, confirming a single crystalline $B_{12}As_2$ film was formed. The $B_{12}As_2$ epitaxial film adopted only one out-plane orientation, the (003) (at 2θ= 22.5 °) and (006) (at 2θ= 45.7 °), belonging to the same family of crystal planes <001>.

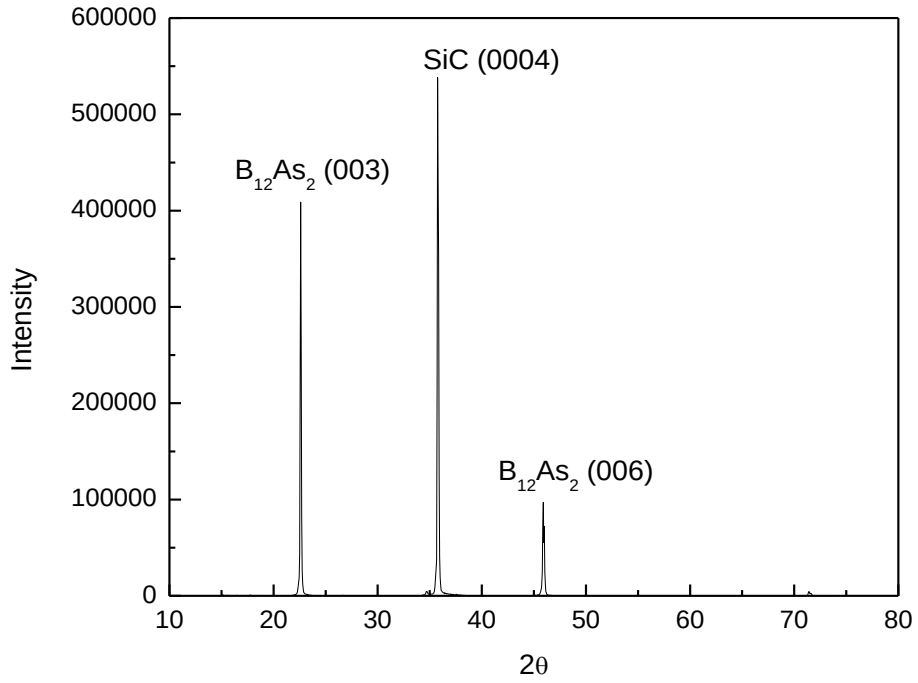


**Figure 4.3 General XRD pattern of epitaxial $B_{12}As_2$ grown on (0001) 4H-SiC.**

### *4.3.3 Substrate effect*

Figure 4.4 (a) and (b) show the surface morphologies of heteroepitaxial $B_{12}As_2$ thin films grown on on-axis *c*-plane 6H- and 4H-SiC, respectively. A high density of twins was observed for the film grown on on-axis 6H-SiC. The film grown on the on-axis 4H-SiC was smoother compared to that on 6H-SiC. However, equilateral triangles rotated 180 ° (or equivalently 60 °) relative to each other- a morphology that is characteristic of rotational twinning-were observed, as shown in Figure 4.4 (b). The enlarged image of two triangular grains showed they were 180 ° rotated relative to each other. Triangular features are indicative of rotational twins, especially when the triangles are rotated relative to each other. SWBXT also revealed that there were two in-plane orientations of $B_{12}As_2$ grown on on-axis *c*-plane 4H-SiC [21].

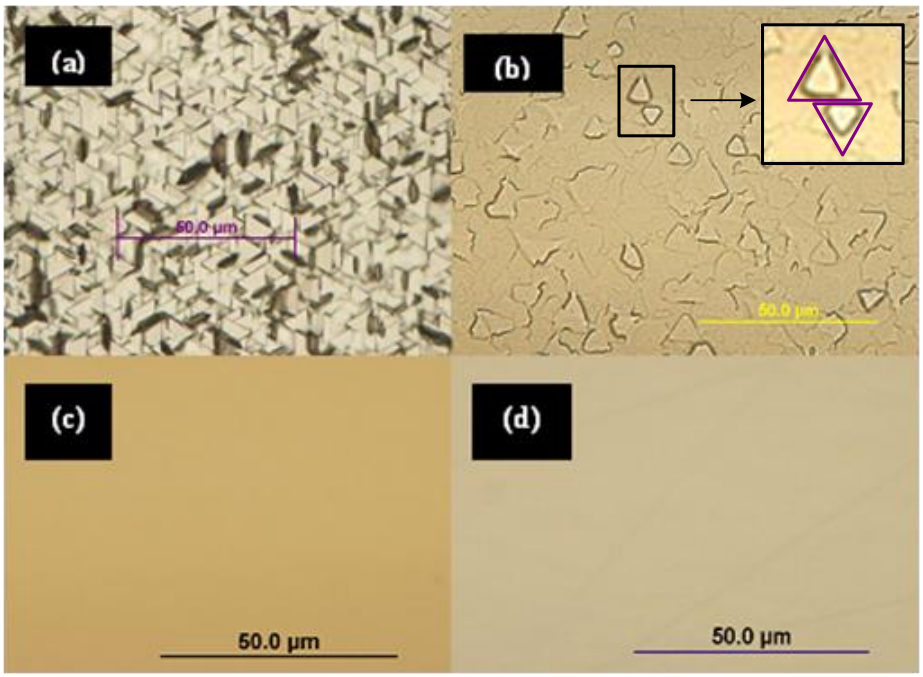


**Figure 4.4 Optical images of $B_{12}As_2$ grown on (a) on-axis c-plane 6H-SiC, (b) on-axis c-plane 4H-SiC, (c) c-plane 4H-SiC with 7 °off towards (1-100) and (d) m-plane 15R-SiC.**

In contrast to the rough surfaces on on-axis substrates, films grown on *c*-plane 4H-SiC with 7 ° offcut towards (1-100) and *m*-plane 15R-SiC, were much smoother and almost featureless, suggesting low densities of twins, as shown in Figure 4.4 (c) and (d). It has been proposed that *m*-plane 15R-SiC is potentially a good substrate choice for the growth of untwined $B_{12}As_2$ epilayers [19]. However, 15R-SiC substrates are presently not commercially available. The *m*-plane 15R-SiC substrate used here had inclusions of 6H-SiC (the insertion in Figure 4.5). This illustrates the improvement in growth which can be achieved in *m*-plane 15R-SiC, as only in those areas was a smooth $B_{12}As_2$ film achieved, while in the 6H-SiC regions, the $B_{12}As_2$ was rough (Figure 4.5).

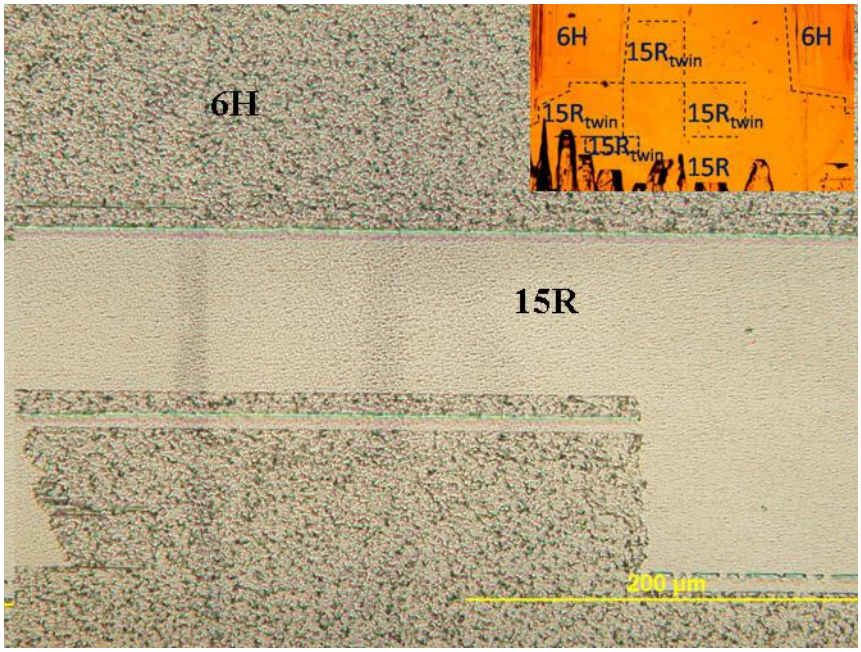


**Figure 4.5 Optical micrographs of the surface morphologies of $B_{12}As_2$ grown on *m*-plane 15R-SiC with 6H-SiC inclusions, the insert shows the polytypes distribution on the substrate before deposition.**

Films grown on the 15-SiC region had smaller, less obvious grain boundaries and smoother surfaces. From the SEM image of the film grown on *m*-plane 15R-SiC and on-axis *c*-plane 4H-SiC, shown in Figure 4.6 (a) and (b), the former has a uniform microstructure, small grains and single orientation. SWBXT revealed that it was untwinned $B_{12}As_2$, confirming *m*-plane 15R-SiC is a good substrate for twin-free heteroepitaxy of $B_{12}As_2$. However, the difficulty of growing pure 15R-SiC hinders the application of this substrate.

The SEM images of $B_{12}As_2$ films grown on 7 ° and 4 ° off-axis towards [1-100], shown in Figure 4.6 (c) and (d), also confirmed the improved microstructures and reduced defect densities on those off-axis substrates.

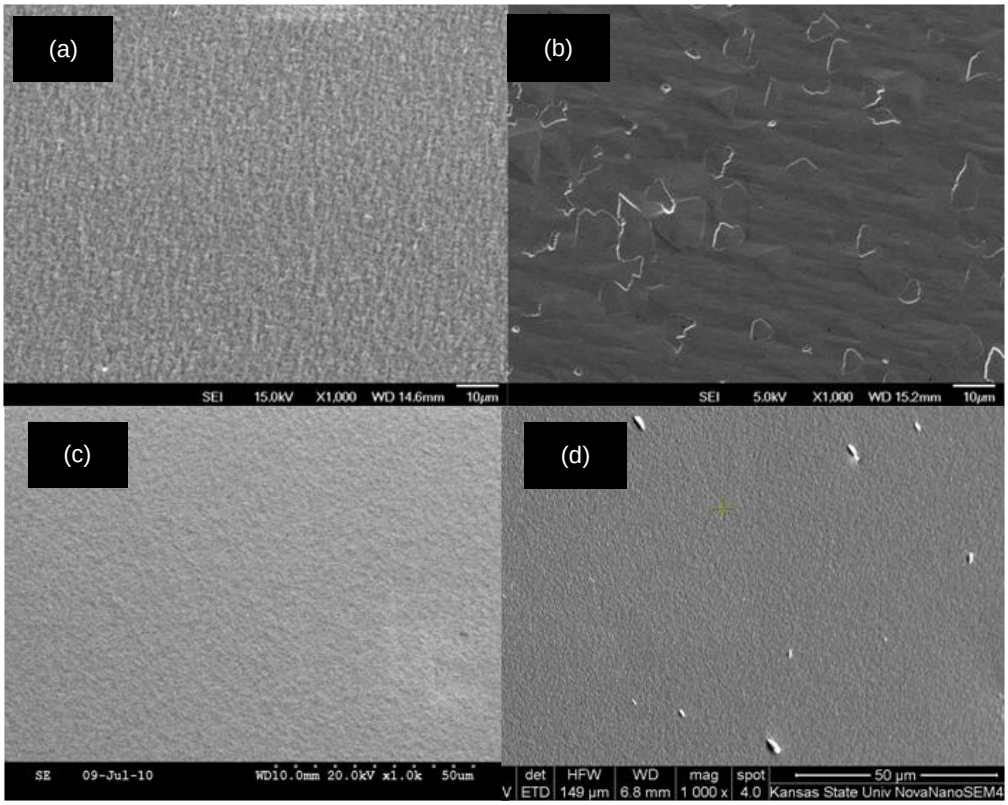


**Figure 4.6 SEM images of $B_{12}As_2$ grown on (a) *m*-plane 15R-SiC, (b) on-axis *c*-plane 4H-SiC, (c) (0001) 4H-SiC with 7 °off-axis towards [1-100], and (d) (0001) 4H-SiC with 4 °off-axis towards [1-100].**

The x-ray Laue patterns obtained via SWBXT of $B_{12}As_2$ films grown on on-axis (0001) 4H-SiC and 7 °off-axis towards [1-100] revealed the in-plane orientations of the epilayer. Detailed indexing analysis of the Laue patterns for the film grown on on-axis substrate, shown in Figure 4.7 (a), confirmed the epitaxial relationship between the epilayer and the substrate is (0001)$B_{12}As_2$<1-100>$B_{12}As_2$||(0001)4H-SiC<1-100>4H-SiC. However, the $B_{12}As_2$ was present in two distinct orientations related by a 180 °twin (or equivalently 60 °) rotation about the (0001) $B_{12}As_2$ plane normal. The well-defined, intense 4H-SiC diffraction spots are labeled with "SiC" while the more diffuse $B_{12}As_2$ spots are labeled with "$B_{12}As_2$ I" and "$B_{12}As_2$ II" corresponding to the matrix or twin orientation.

A detailed indexing analysis of the Laue patterns recorded from the film grown on off-axis 4H-SiC with 7° off from (0001) toward [1-100], shown in Figure 4.7 (b), revealed the expected epitaxial relationship between the epilayer and the substrate, which was

(0001)$B_{12}As_2$<1-100>$B_{12}As_2$||(0001)4H-SiC<1-100>4H-SiC. The well-defined, intense 4H-SiC diffraction spots are labeled with "SiC" while the $B_{12}As_2$ spots are labeled with $B_{12}As_2$. The Laue pattern indicated the single crystalline nature of $B_{12}As_2$, lacking any evidence for the existence of twins. The $B_{12}As_2$ produced much stronger and better-defined diffraction spots compared to the $B_{12}As_2$ grown on other substrates, suggesting improved crystal quality and decreased strain level.

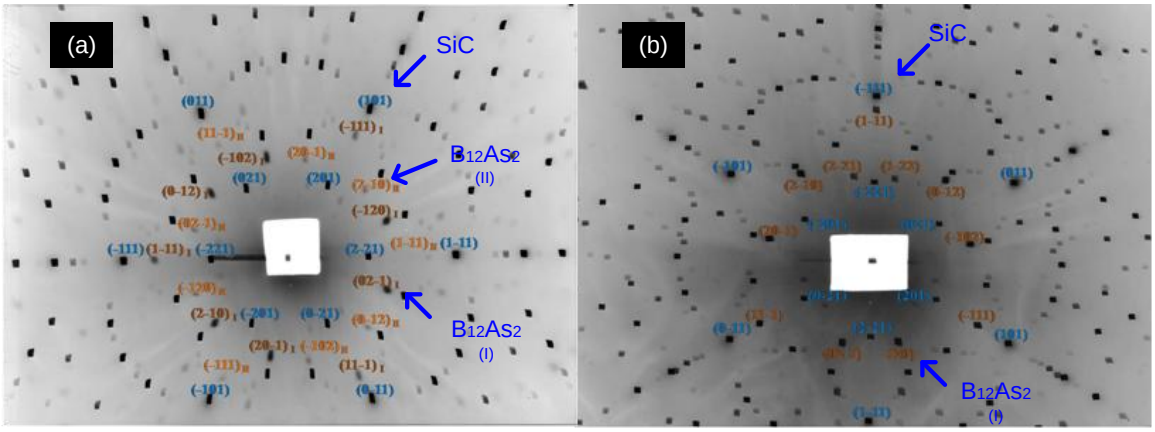


**Figure 4.7 X-ray Laue pattern $B_{12}As_2$ grown on (a) on-axis c-plane 4H-SiC (b) 7° off-axis towards [1-100].**

The improved crystal quality and elimination of twins resulting from using off-axis SiC substrate with specific [1-100] offcut direction were also apparent in the HRTEM micrographs. Figure 4.8 (a) shows the interface between the $B_{12}As_2$ and the on-axis (0001) 4H-SiC. The film grew from a transition layer, approximately 20nm thick disordered mosaic layer, to a more ordered structure. The transition layer arose from the coalescence of translational and rotational variants nucleated at the various nucleation sites on the on-axis (0001) 4H-SiC surface, and rotational twins still existed in the epilayer.

In contrast, the interface appeared abrupt and clean in the film grown on the off-axis substrate, without any transitional layer in between, as displayed in Figure 4.8 (b). Combining the SWBXT result, excellent quality of epitaxial $B_{12}As_2$ films without a transition layer or rotational twins were attained by using an off-axis SiC substrate with specific [1-100] offcut direction.

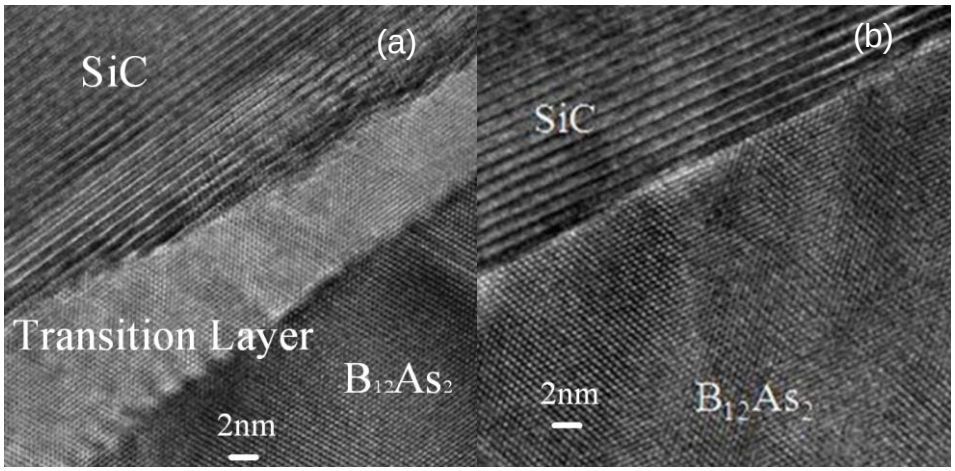


**Figure 4.8 (a) HRTEM image taken along the [10-1] zone axis (equivalent to [11-20] in the hexagonal system) showing a transition layer at an $B_{12}As_2$/on-axis 4H-SiC interface (b) HRTEM image taken along the [10-1] zone axis showing a sharp $B_{12}As_2$/7°off-axis 4H-SiC interface and perfect $B_{12}As_2$ single crystal.**

Raman spectra analysis provides additional evidence that *c*-plane 4H-SiC with 7 ° off-cut towards [1-100] produces excellent crystal quality and eliminates the twinning problem. Comparing the Raman spectra of films grown on *c*-plane 4H-SiC with 7 ° off-cut towards [1-100] and that on on-axis substrate, as shown in Figure 4.9, the former substrate led to the higher $B_{12}As_2$ film crystal quality because the peak line-width was narrower and intensity was significantly stronger.

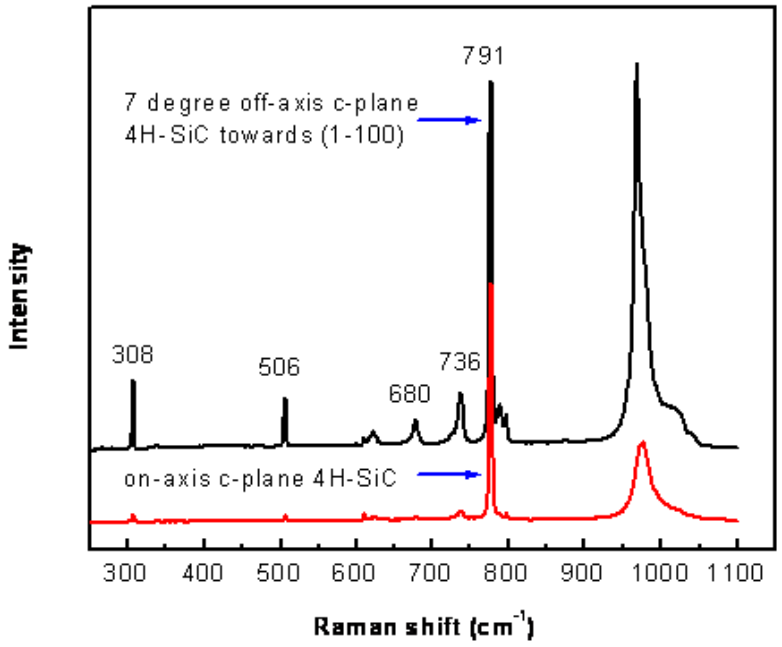


**Figure 4.9 Raman spectra recorded from a $B_{12}As_2$ film grown on on-axis *c*-plane 4H-SiC with a thickness of 2.9 μm and *c*-plane 4H-SiC with 7 °offcut towards [1-100] with a thickness of 2.6 μm.**

The full width at half maximum (FWHM) of the x-ray rocking curves is another direct measure of crystal quality: the narrower the rocking curve width, the higher the crystal quality. Misorientation, dislocation and residual strain are all the factors that can cause the broadening of the diffraction peak. The FWHM of films grown on the 4 ° and 7 ° off-axis substrates were 743 and 865 arcsec, smaller than that of film grown on on-axis substrate, which was 990 arcsec, as shown in Table 4.1. These results confirmed that the defect densities were reduced and the crystal quality was improved by using off-axis substrates.

**Table 4.1 FWHM of x-ray rocking curves with reflection of (0003) $B_{12}As_2$ grown on on-axis *c*-plane 4H-SiC and *c*-plane 4H-SiC with 4 ° or 7 ° off towards [1-100] at 1300 ℃**

| Substrate | FWHM (arcsec) |
|---|---|
| on-axis *c*-plane 4H-SiC | 990 |
| *c*-plane 4H-SiC with 4° offcut towards [1-100] | 743 |
| *c*-plane 4H-SiC with 7° offcut towards [1-100] | 865 |

The electrical properties of the $B_{12}As_2$ on SiC were also studied. We obtained the resistivity, carrier type and concentration and Hall mobility of $B_{12}As_2$ grown on various substrates as shown in Table 4.2, via Hall effect measurement and resistivity measurement. These are all key factors for the design and performance of electronic devices [22].

The resistivity measurements utilized the Van der Pauw geometry, square samples with four point metal contacts at the corners. For room temperature measurements, four-point indium contacts were soldered to the $B_{12}As_2$ layer. The linear I-V curves confirmed the formation of ohmic contacts. Field variable Hall effect measurements were taken at both positive and negative magnetic field and the average value eliminated the effects from the magnetic field. For films grown on the on-axis 4H-SiC, which were semi-insulating substrates, we obtain the resistivity, mobility, carrier type and concentration directly. However, for films grown on the 4 ° and 7 ° off-axis substrates, which were n-type SiC, the effect of carriers in the substrates must be eliminated. Using the field variable Hall effect results, and a software named Quantitative Mobility Spectrum Analysis, we separated the measurement results from different charge carriers and thus obtain the mobility and carrier concentrations in the $B_{12}As_2$ epilayer.

All the $B_{12}As_2$ films exhibited *p*-type conductivity, thus, the majority carriers were holes. The resistivity of undoped films was on the order of $10^3$-$10^4$ ohm cm. The hole concentrations ranged from $10^{14}$ to $10^{15}$ at room temperature. The Hall mobilities of $B_{12}As_2$ films grown on on-axis *c*-plane 4H-SiC were only near 1 $cm^2V^{-1}s^{-1}$. In contrast, those of films grown on *c*-plane 4H-SiC with 4 ° or 7 ° offcut towards [1-100] were between 40 and 50 $cm^2V^{-1}s^{-1}$. The high mobility in the film grown on off-axis substrates was also a reflection of the improved $B_{12}As_2$ crystal quality in comparison to the films on on-axis SiC substrates.

**Table 4.2 Electrical properties of $B_{12}As_2$ film grown on on-axis *c*-plane 4H-SiC and *c*-plane 4H-SiC with 4 ° or 7 ° tilt towards [1-100] at 1350 ℃.**

| Substrate | Resistivity (ohm cm) | Carrier Concentration ($cm^{-3}$) | Hall Mobility ($cm^2V^{-1}s^{-1}$) |
|---|---|---|---|
| on-axis *c*-plane 4H-SiC | $1.5\times10^4$ | $4.4\times10^{14}$ | 0.96 |
| *c*-plane 4H-SiC with 4 °offcut towards [1-100] | $6.6\times10^3$ | $2.0\times10^{15}$ | 46.2 |
| *c*-plane 4H-SiC with 7 °offcut towards [1-100] | $3.8\times10^4$ | $4.8\times10^{14}$ | 44.5 |

### *4.3.4 Temperature effect*

#### *4.3.4.1 Temperature effect on growth rate*

Growth temperature is the most important process parameter, as it determines the growth rate, surface morphology and crystal quality. In this study, the temperature employed to produce $B_{12}As_2$ film on SiC substrate ranged from 1150 to 1450 ℃ in 50 ℃ steps, with fixed flow rates of $B_2H_6$ and $AsH_3$ of 8.96 x $10^{-3}$ mol/min and 8.96 x$10^{-2}$ mol/min, respectively. No deposits formed below 1200 ℃. At 1450 ℃, boron films formed instead of icosahedral boron arsenide, as revealed by Auger electron microscopy. The average growth rates were calculated from the weigh change per unit area over the reaction time.

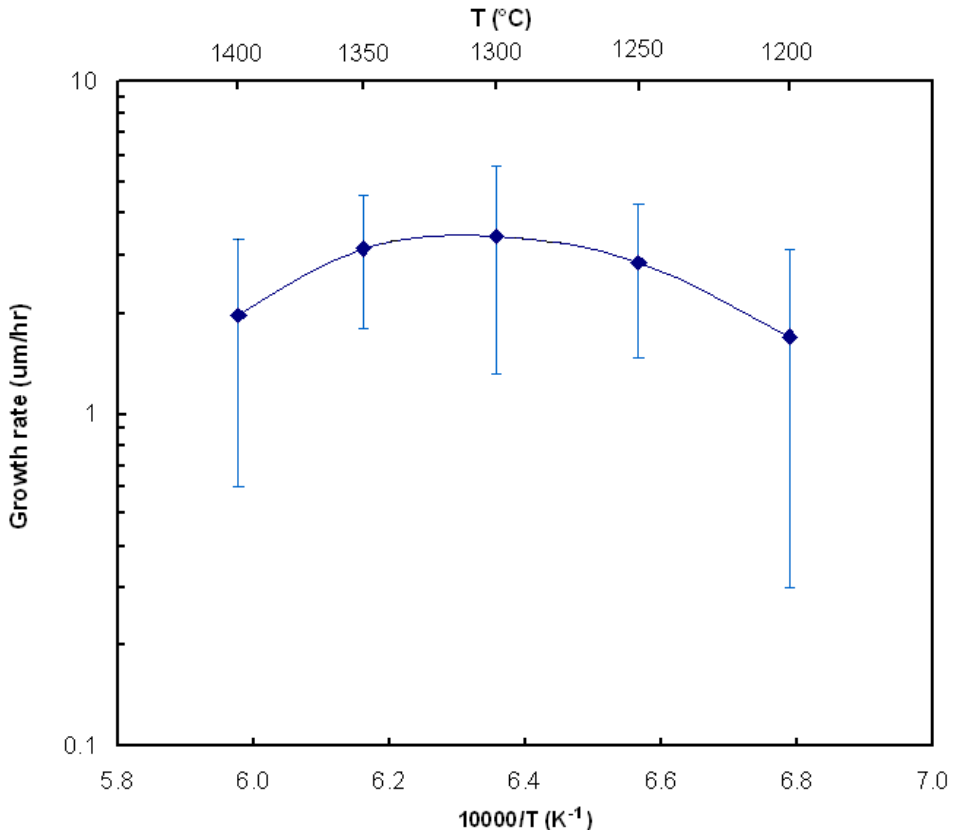


**Figure 4.10 Plot of the logarithm of the growth rate versus the reciprocal temperature for the $B_{12}As_2$ grown on *c*-plane 4H-SiC with 4 ℃offcut towards [1-100] at a total pressure of 100 torr.**

Figure 4.10 shows the temperature dependency of the growth rate. The mean growth rate of $B_{12}As_2$ increased from 1.70 μm/h at 1200 ℃ to 3.42 μm/h at 1300 ℃ and decreased to

1.98μm/h at 1400° C. However, the measured growth rates have high standard deviations, 1.4~2.0 μm/h. Thus, it is possible that the growth rate is simply invariant with the temperature.

### *4.3.4.2 Film quality by FWHM of x-ray rocking curves*

As discussed above, the FWHM of x-ray rocking curves reflects the film quality and residual strains. FWHM of x-ray rocking curves of $B_{12}As_2$ grown at different temperatures are depicted in Figure 4.11, as well as those of films grown on different 4H-SiC substrates.

The FWHM increased from 730 to 815 arcsec as the temperature increased from 1200 to 1350 ℃, similar to the values Nagarajan *et al* [14] obtained on on-axis (0001) 6H-SiC substrates-760-880 arcsec. At 1400 ℃, the FWHM is over 3000 arcsec, suggesting the $B_{12}As_2$ film has a high density of defects and a high level of strain. At relatively high temperatures, the decomposition of reactant gases, $B_2H_6$ and $AsH_3$, are more significant, increasing the possibility of the formation of boron or arsenic solids in the gas phase. As a result, B, As or B-As particles fall down on the substrate and cause defects or strains.

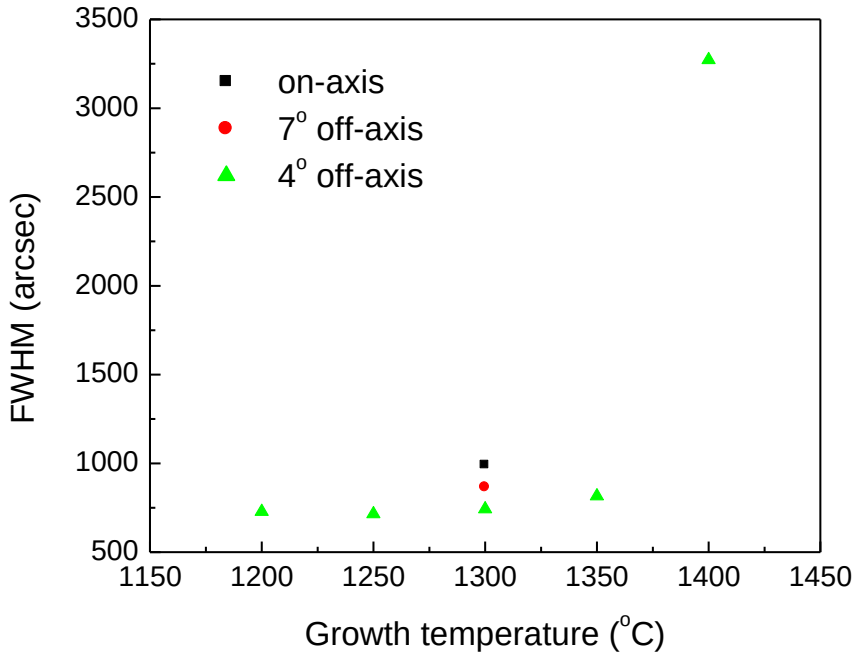


**Figure 4.11 FWHM of x-ray rocking curves with reflection of the (0003) $B_{12}As_2$ plane, recorded from $B_{12}As_2$ film grown on *c*-plane 4H-SiC with 4 °offcut towards [1-100]**

The (0003) plane reflection was insensitive to the in-plane rotational twins, and this could account for the similar values of the FWHM for all substrates, as shown in Figure 4.11.

#### *4.3.4.3 Temperature effect on Hall mobility*

Hall effect measurements which determine the majority charge carrier type, concentration, and mobility is another means of assessing the film quality. In semiconductor materials, the carrier mobility is characteristic of how quickly the charge carriers can move within the semiconductor when an electrical field is applied. Its value is reduced in the presence of defects and impurities. The majority carrier mobility obtained by Hall effect measurements, is the Hall mobility. Stated simply, the higher the mobility, the lower the defect density. All as-grown $B_{12}As_2$ films exhibited *p*-type conductivity. The Hall mobility of $B_{12}As_2$ film grown at 1200-1400 ℃ on *c*-plane 4H-SiC with 4 ° offcut towards [1-100] is shown in Figure 4.12.

The Hall mobility was higher than 10 $cm^2V^{-1}s^{-1}$ for all samples grown at temperatures below 1400 ℃. This is one order of magnitude higher than previous reported values (1 $cm^2V^{-1}s^{-1}$) [22]. The maximum mobility was 80 $cm^2V^{-1}s^{-1}$ for the film grown at 1300 ℃. This suggests this temperature produced the best film quality with the lowest densities of structural defects. Also, with increasing temperature, the mobility first increased, reaching a maximum value at 1300 ℃, and then decreased. This scheme is possibly due to the desorption of the reactant species, B and As, at high temperatures. In the CVD process, $B_2H_6$ and $AsH_3$ decomposed to B and As at elevated temperatures, adsorbed on the SiC substrates and then formed $B_{12}As_2$ when the chemical reaction took place. Higher crystal structural quality was attained because the atoms have sufficient activities for surface diffusion as temperatures increased from 1200 to 1300 ℃. However, when the temperature was increased further, from 1300 to 1400 ℃, desorption of reactants from the substrate surface was more significant, causing less reaction sites and more structural defects in the epilayer, or gas phase nucleation was a problem as previously noted. This trend is also consistent with the conclusion obtained by the x-ray rocking curve technique.

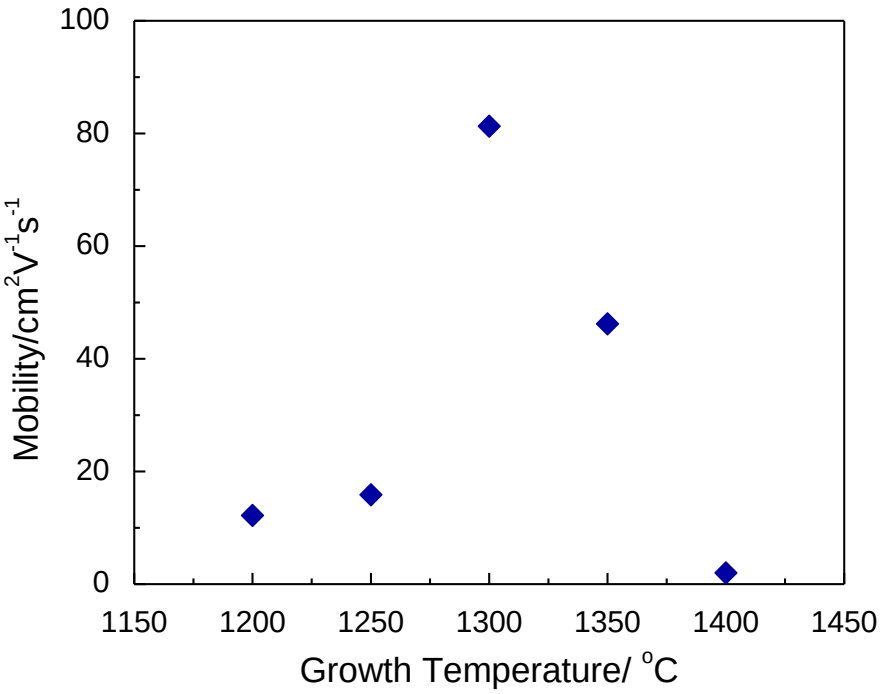


**Figure 4.12 Hall mobility of $B_{12}As_2$ film grown at 1200-1400 ℃ on *c*-plane 4H-SiC with 4 ° offcut towards [1-100]**

Considering the temperature dependence of the growth rate, the FWHM of the epitaxial layer, and the Hall mobility of films grown at different temperatures, we can draw the conclusion that 1300 ℃ is the optimal temperature for depositing $B_{12}As_2$ films with the lowest defect densities, smallest residual strains, highest hole mobility and with the highest growth rate.

### *4.3.5 Feed reactant concentration effect*

In the CVD process, $B_{12}As_2$ is formed by the following chemical reaction.

$$6B_2H_6 + 2AsH_3 \rightarrow B_{12}As_2 + 21H_2$$

From the stoichiometry, the flow rate ratio of $B_2H_6$ to $AsH_3$ should be 1:0.33. However, previous research showed excess $AsH_3$ is required, and the higher the $AsH_3$ concentration the higher crystal quality [14]. But whether the flow rate ratio of $B_2H_6$ to $AsH_3$ in the feed affects the composition of the epitaxial layer was not previously reported. We analyzed the chemical composition of the $B_{12}As_2$ film grown at various flow rate ratio of $B_2H_6$ to $AsH_3$ in the feed via Scanning Auger Microscopy (SAM). It is a surface composition analysis technique, but a depth profile of the composition can be obtained by taking measurements while sputtering through the epilayer, as shown in Figure 4.13.

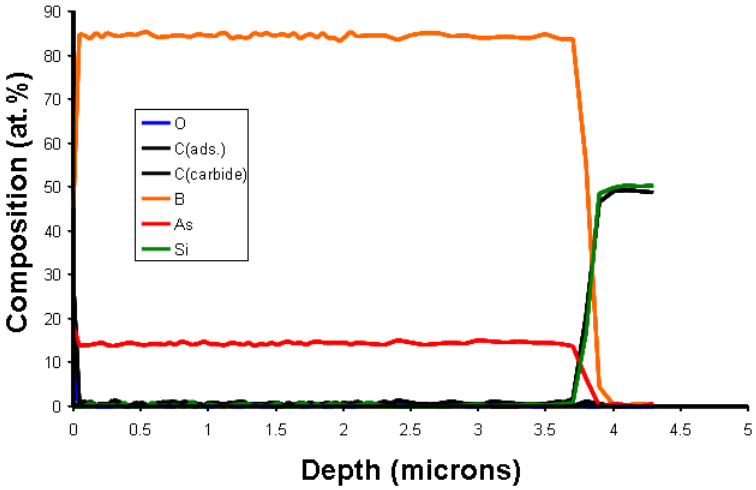


**Figure 4.13 Composition of $B_{12}As_2$ film grown on on-axis *c*-plane 4H-SiC at 1300 ℃ with thickness of 3.68μm and flow rate ratio of $B_2H_6$ to $AsH_3$ of 1:2.**

The B/As ratio present in the $B_{12}As_2$ layer was consistently 6:1 throughout the whole film, confirming the formation of icosahedral boron arsenide only: there was no evidence for cubic boron arsenide (BAs) which exhibits a 1:1 B/As ratio. The boron and arsenic concentrations drop sharply at the interface between $B_{12}As_2$ layer and SiC substrates. No pure boron phase was observed at the interface. Trace amount of oxygen and carbon were also detected, at concentrations that were less than 1 atomic%. The composition in the epilayer of films grown with different feed flow rate ratios was analyzed by AEM and XPS (x-ray photoelectron spectroscopy); the results are listed in Table 4.3

**Table 4.3 Composition analysis of $B_{12}As_2$ grown at different flow rate ratio of $B_2H_6$ to $AsH_3$ at 1350 ℃ via AEM and XPS**

| Flow rate ratio of $B_2H_6$ to $AsH_3$ | B/As in epilayer AEM | B/As in epilayer XPS |
|---|---|---|
| 1:2 | 6:1 | 6.5:1 |
| 1:1.6 | 6:1 | 6.2:1 |
| 1:1 | 6:1 | 6.4:1 |
| 1:0.6 | 6.5:1 | 6.3:1 |
| 1:0.2 | 305:1 | No arsenic |

Even with $AsH_3$ concentration greater than the stoichiometry value, the B/As ratio in the film was approximately 6:1. Notice that both the SAM and XPS technique needs a standard sample with known composition to determine the correction factors for different elements.

However, the film grown with an enriched diborane flow rate and an arsine flow rate smaller than the stoichiometry value, produced boron instead of icosahedral boron arsenide. No arsenic was detected by either techniques. Thus, excess $AsH_3$ is necessary and the B/As ratio in the film was 6:1 when the $B_2H_6$ to $AsH_3$ ratio was great than the 1:0.33. No phase separation occurred with excess $AsH_3$. Nevertheless, a high $AsH_3$ concentration creates a high arsenic concentration in the gas phase that prevents the loss of arsenic via thermal decomposition.

## 4.4 Conclusions

First, SiC substrates that are capable of eliminating twinning defects in heteroepitaxial $B_{12}As_2$ films include *m*-plane 15R-SiC and *c*-plane 4H-SiC with 4 ° or 7 °off-cut towards [1-100]. With these substrates, the surface roughness is also greatly reduced and the microstructure is more uniform. Probably the best practical substrate for $B_{12}As_2$ devices is *c*-plane 4H-SiC with 7 °off-cut towards [1-100], since 15R-SiC substrates are not commercially available. On these substrates, the diffraction spots recorded from SWXRT are better-defined and have stronger intensity; no transition layer was observed via HRTEM; the Raman peaks exhibits narrower line-width and higher intensity; the FWHM of x-ray rocking curve is smaller; and the Hall mobility is one order of magnitude higher. Therefore, the defect densities of $B_{12}As_2$ films are reduced, the strain level are decreased and not only the crystal quality is increased but also the electrical properties are improved.

Second, temperature is the most important parameter which can affect the crystal quality and the strain level. The growth rate varies only slightly with temperatures between 1200 and 1400 ℃. But there is insufficient evidence to confirm the growth rate was in dependent of temperature: measurements of the film thickness exhibited a standard deviation that was comparable to the mean value. The defect densities and residual strains, reflected by the FWHM of the x-ray rocking curves, increased with growth temperatures. In the CVD process, $B_2H_6$ and $AsH_3$ decomposed to B and As at elevated temperatures, adsorbed on the SiC substrates and then formed $B_{12}As_2$ when the chemical reaction took place. Higher crystal structural quality was attained because the atoms have sufficient activities for surface diffusion and bulk diffusion as temperatures increased from 1200 to 1300 ℃. However, when the temperature was increased further, from 1300 to 1400 ℃, desorption of reactants from the substrate surface was more significant, causing less reaction sites and more structural defects in the epilayer.

The maximum room temperature hole mobility of the $B_{12}As_2$ was 80 $cm^2V^{-1}s^{-1}$, obtained on films produced at 1300 ℃. This is the optimal temperature to deposit $B_{12}As_2$ film because the epitaxial layer has the lowest defect densities, smallest residual strains, highest hole mobility and highest growth rate. Higher hole mobilities may be possible with further reductions in defects and lower residual impurity concentrations.

Third, the epilayer grew with a consistent composition of B/As = 6:1 only when the $B_2H_6$ to $AsH_3$ ratio in the feed exceeds 1:0.33. And no phase separation occurred at the interface between $B_{12}As_2$ and SiC with excess $AsH_3$. With the $B_2H_6$ to $AsH_3$ ratios smaller than the 1:0.33, the epitaxial layer is only boron. Therefore, a high $AsH_3$ concentration is advantageous because it can create a high arsenic concentration in the gas phase that prevents the loss of arsenic by thermal decomposition.

## References


[1] S. Bakalova, Y. Gong, C. Cobet, N. Esser, Y. Zhang, J. H. Edgar, Y. Zhang, M. Dudley, and M. Kuball, *Phys. Rev. B*, 81, 075114 (2010)

[2] D. Emin, *Phys. Today*, 55, January (1987)

[3] J.R. Michael, T. L. Aselage, D. Emin and P.G. Kotula, *J. Mater. Res.*, 20 , 3004 (2005).

[4] H. Chen, G. Wang, M. Dudley, L. Zhang, L. Wu, Y. Zhu, Z. Xu, J.H. Edgar and M. Kuball, *J. Appl. Phys.*, 103, 123508 (2008)

[5] M. Carrard, D. Emin and L. Zuppiroli, *Phys. Rev. B*, 51, 11270 (1995).

[6] D. Emin, *J. Solid. State. Chem.*, 177, 1619 (2004)

[7] D. Emin and T. L. Aselage, *J. Appl. Phys.*, 97, 013529 (2005)

[8] D. Emin, *J. Solid. State. Chem.*, 179, 2791 (2006)

[9] Y. Gong, M. Tapajna, S. Bakalova, Y. Zhang, J.H. Edgar, Y. Zhang, M. Dudley, M. Hopkins, and M. Kuball., *Appl. Phys. Lett.*, 96, 223505(2010)

[10] R.H. Wang, D. Zubia, T. O'Neil, D. Emin, T. Aselage, W. Zhang and S.D. Hersee, *J. Electron. Mater.* , 29, 1304 (2000)

[11] X. Zhou, J. H. Edgar and S. Speakman, *J. Cryst. Growth*, 293, 162 (2006)

[12] M. Hirayama, K. Shohno, *Jpn. J. Appl. Phys.* 12, 1960, (1973)

[13] L. A. Correia, R. C. Van Oort, P. J. Vander Put, *Reactivity of Solids*, 2, 203, (1986)

[14] R. Nagarajan, Z. Xu, J. H. Edgar, F. Baig, J. Chaudhuri, Z. Rek, E. A. Payzant, H. M. Meyer, J. Pomeroy and M. Kuball, *J. Cryst. Growth*, 273, 431 (2005)

[15] W.M. Vetter, R. Nagarajan, J. H. Edgar and M. Dudley, *Mater. Lett.*, 58, 1331 (2004)

[16] H. Chen, G. Wang, M. Dudley, L. Zhang, L. Wu, Y. Zhu, Z. Xu, J.H. Edgar and M. Kuball, *J. Appl. Phys.*, 103, 123508 (2008)

[17] S. H. Wang, E. M. Lysczek, Bangzhi Liu, S. E. Mohney, Z. Xu, R. Nagarajan and J. H. Edgar, *Appl. Phys. Lett.*, 87, 042103 (2005)

[18] J.D. Hartman, A.M. Roskowski, Z.J. Reitmeier, K.M. Tracy, R.F. Davis, R. J. Nemanich, *J. Vac. Sci. & Tech. A*, 21, 394 (2003)

[19] F. Dulot, L. Mansor, A. Elycuras, W. Wulfhekel, D. Sander, F. A. d'Avitaya, M. Hanbuchen, *Appl. Surf. Sci.*, 197, 319 (2002)

[20] A. Kawasuso, K. Kojima, M. Yoshikawa, H. Itoh, K. Narumi, *Appl. Phys. Lett.*, 76, 1119 (2000)

[21] Y. Zhang, H. Chen, M. Dudley, Y. Zhang, J. H. Edgar, Y.Gong, S. Bakalova, M. Kuball, L. Zhang, D. Su, K. Kisslinger, Y.Zhu, *Mater. Res. Soc. Symp. Proc.* 1246, B04-2 (2010)

[22] Z. Xu, J. H. Edgar, D.C. Look, S. Baumann, R. J. Bleiler, S. H. Wang and S. E. Mohney, *Appl. Phys.*, 101, 053710 (2007)

[23] H. Chen, G. Wang, M. Dudley, Z. Xu, J. H. Edgar, T. Batten, M. Kuball, L. Zhang, and Y. Zhu, *Appl. Phys. Lett.*, 92 (23), 231917 (2008)

# Chapter 5 - Electrical Transport Properties and Controlled Doping of Heteroepitaxial $B_{12}As_2$ layers on SiC substrates

## 5.1 Introduction

Icosahedral boron arsenide ($B_{12}As_2$) is a rarely studied wide bandgap (3.2 eV) semiconductor, which has two unusual and distinguishing properties: it has an extraordinary resistance to radiation damage and for an isotope of one of it elements, boron-10, its thermal neutron capture cross-section is exceptionally large (~4000 barns, orders of magnitude larger than that of most elements) [1]. The chemical bonding in $B_{12}As_2$ is unusual; two valence electrons are shared between three boron atoms [2, 3, 4, 5]. In contrast, in general for most materials, chemical bonds are formed by the sharing of more than one electron per atom between only two atoms. As a consequence of this electron-deficient bonding and the small size of boron ions, $B_{12}As_2$ actually *self-heals* from radiation damage; interstitials and degraded boron icosahedra caused by radiation spontaneously recombine and the material is repaired [4, 5]. This property in a semiconductor would be very useful in electronic devices that operate in radiation intense environments, such as alphavoltaic or betavoltaic cells, devices which directly convert the energy available from radioisotopes to electrical power. The high B-10 thermal neutron capture cross-section makes $B_{12}As_2$ a good candidate for solid-state neutron detectors. Such devices based on boron-10 enriched $B_{12}As_2$ would be more sensitive, more compact, operate on minimal power, and be lower cost in comparison to conventional gas-filled detectors.

$B_{12}As_2$ has been successfully produced by chemical vapor deposition (CVD) on (0001) 6H- or 4H-SiC substrates with or without misorientation [6, 7, 8, 9]. The $B_{12}As_2$ epilayers grown on on-axis 6H-SiC contain a high density of translational and rotational variants as a consequence of the different lattice constants and symmetries of the film and the substrate.

For semiconductor materials, the electrical transport properties are the basis for designing and fabricating electronic devices. Nevertheless, there have been few studies on the electrical transport properties of $B_{12}As_2$ [10, 11]. Also, for semiconductor devices, control of the electrical properties is essential, and is achieved by intentionally doping with impurities. Emin [3] predicted that it should be possible to modulate the resistivity of $B_{12}As_2$ by doping it with silicon. Silicon is believed to substitute for an arsenic atom which has one more valence electron than

silicon. Thus, doping with silicon removes an electron from a bonding state and introduces a hole. Thus the hole concentration should increase with Si doping and consequently the resistivity of $B_{12}As_2$ should decrease in this way. Xu *et al* [10] proved that Si was an effective *p*-type dopant. They showed the resistivity of $B_{12}As_2$ films decreased from $10^5$ to 10 ohm cm by adding an Si concentration of $7 \times 10^{21}$ $cm^{-3}$.

Therefore, the goals of this research were to determine the basic electrical transport properties of unintentionally doped and silicon-doped $B_{12}As_2$. The electrical properties of the $B_{12}As_2$ layers were modulated by intentionally doping with silicon. The conductivity, the majority carrier concentrations and mobilities were measured by temperature variable Hall effect measurements, revealing the charge carrier transport mechanism in this unusual semiconductor. These results were also correlated with both the residual impurities and intentionally added silicon concentrations.

## 5.2 Experimental Procedures

$B_{12}As_2$ films were synthesized via CVD in an inductively heated horizontal quartz reactor, employing 1% $B_2H_6$ in $H_2$ and 1% $AsH_3$ in $H_2$ as the source gases. The carrier gas was purified hydrogen with a constant flow rate of 3.5 SLM. All the films were deposited over a temperature range of 1200-1400 ℃, and a total pressure of 100 torr. The flow rates of $B_2H_6$ and $AsH_3$ were fixed at 40 and 400 sccm, respectively. Si doping was achieved by adding a fixed amount of $SiH_4$ simultaneously with epitaxy. The source gas was 0.1% $SiH_4$ diluted in $H_2$ and its flow rate was varied from 10 sccm to 90 sccm to achieve different dopant concentrations. Before deposition, the SiC substrate was *in situ* etched in hydrogen at 1650 ℃ for 15 min to prepare a pristine surface. Three different substrates were utilized in this study: semi-insulating on-axis (0001) 6H-SiC, *n*-type (0001) 4H-SiC with 4 ° off-axis towards [1-100], and *n*-type (0001) 4H-SiC with 7 ° off-axis towards [1-100].

The concentrations of Si and the residual impurities were measured by time-of-flight secondary ion mass spectroscopy (TOF-SIMS). The absolute concentrations of these impurities could not be determined without a standard calibration. Therefore, an unintentionally doped $B_{12}As_2$ thin film was implanted with known concentrations of carbon, oxygen, hydrogen and silicon, to serve as the standard. To achieve a peak impurity concentration at a certain depth and high signal-to-noise ratio, a TRIM calculation was carried out, to determine the energy and dose

required of each implanted element. This implanted sample serves as a calibration standard for subsequent measurements so absolute concentrations could be measured. In TOF-SIMS analysis, a 25 keV $Bi^+$ beam was used as the primary ion beam bombarding on the sample surface and a 2keV $Cs^+$ beam was utilized for sputtering.

Field and temperature variable Hall effect measurements were taken to evaluate the majority carrier type, concentrations and mobility of the $B_{12}As_2$ film. The temperature was varied from 300 to 500K or 77 to 293 K for different tests. The magnetic field was varied from 500 to 8000 Gauss. The Hall effect and resistivity measurement utilize a Van der Pauw geometry; square samples with four point contacts at the corners. Prior to the measurement, ohmic contacts to the $B_{12}As_2$ were formed by depositing 50nm Cr and 100nm Pt via e-beam evaporation, followed by annealing at 600 ℃ for 10 minutes in an argon ambient [12, 13]. For the samples grown on the semi-insulating substrates, the electrical properties were obtained by the Hall effect measurement directly. For the samples grown on the n-type substrates, the electrical properties were calculated by a software package, Quantitative Mobility Spectrum Aanlysis (QMSA), to cancel the contribution from the substrates.

## 5.3 Results and Discussion

### *5.3.1 Temperature dependence of conductivity*

The temperature dependence of electrical conductivity is essentially determined by the actual transport mechanism [14, 15]. The $B_{12}As_2$'s conductivity varied with temperature, as shown in

Figure 5.1. At low temperatures (77-253 K) and high temperatures (300-500 K), the conductivity varies in accordance with Mott's law,

$$\sigma = \sigma_0 \exp\left[-\left(\frac{T_0}{T}\right)^{1/4}\right],$$

$$T_0 = \frac{60}{\pi k_B l^3 N(E_F)}, \qquad \textbf{Eq. 5-1}$$

where $l$ is the localization length of the carrier's wave function, $N(E_F)$ is the electron density of localized states (DOLS) at the Fermi level, $E_F$, $k_B$ is the Boltzmann constant and $\sigma_0$ is a constant [16].

The linear correlation coefficients are 1 and 0.99, respectively. This result suggests that the conduction follows a variable range hopping mechanism, which has been used to describe the conduction in strongly disordered systems with localized states. Variable range hopping mode has also been found in other icosaheral boron compounds, such as beta-rhombohedral boron [16], boron carbide [17] and tetragonal boron nanobelts [18].

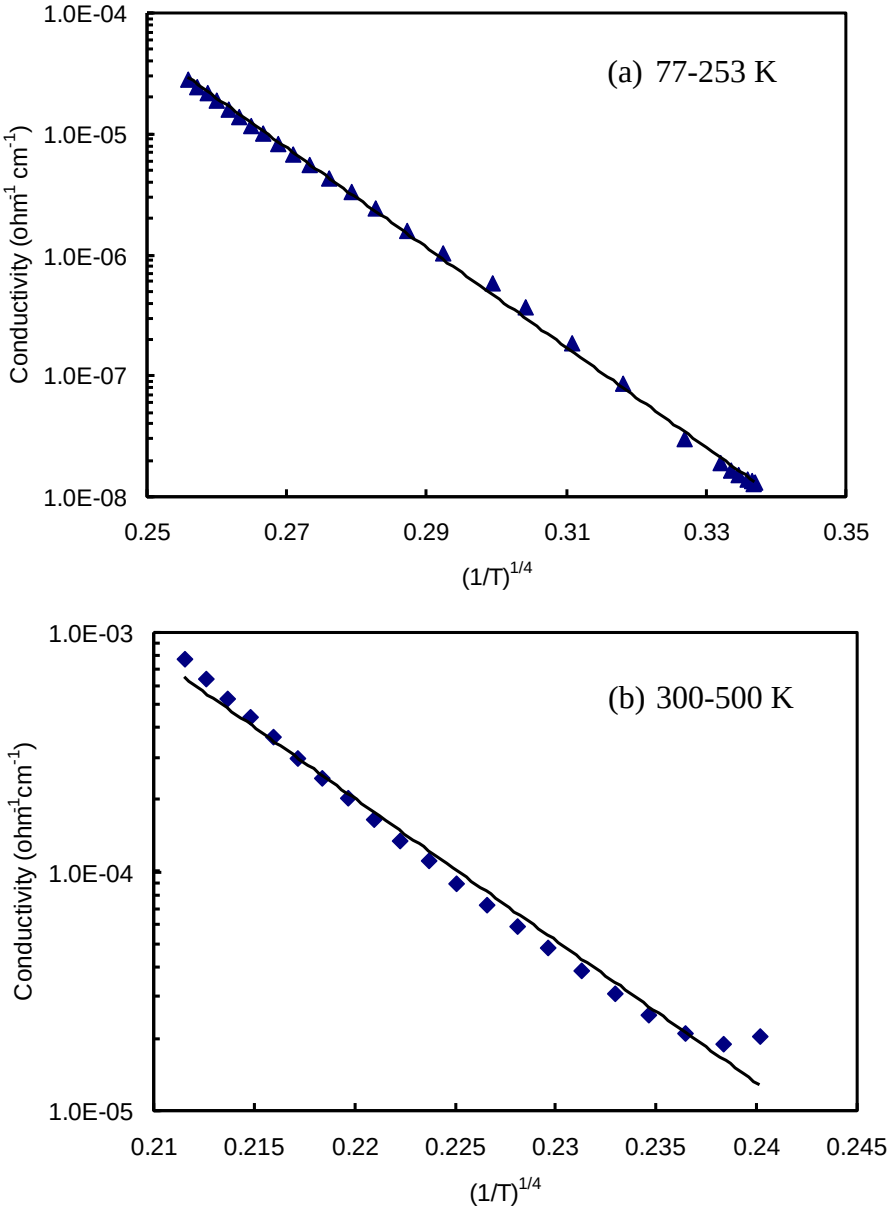


**Figure 5.1 (a) Conductivity of $B_{12}As_2$ versus $(1/T)^{1/4}$ at 77~253K from a $B_{12}As_2$ layer grown at 1300 ℃ with a thickness of 4.2 μm; (b) Conductivity of $B_{12}As_2$ versus $(1/T)^{1/4}$ at 300~500K from a $B_{12}As_2$ layer grown at 1350 ℃ with a thickness of 5.2 μm**

The variable range hopping phenomenon was observed not only in intrinsic $B_{12}As_2$ films, but also in the intentionally Si-doped samples. The fitting parameter $N(E_F)$ was analyzed based on Eq. (5-1) with the assumption that $l$ is on the order of the atomic radius of boron (0.1 nm). The results are listed in Table 5.1. The value of the $N(E_F)$ of the Si-doped samples is nearly 8 times greater than that of pristine $B_{12}As_2$. This result might be explained by speculating that the distribution of the density of localized states is modified by Si doping into interstitial sites of $B_{12}As_2$. Icosahedral boron arsenide is electron deficient, whereas the empty orbitals for electrons to fill in possibly become the intrinsic acceptor levels (IALs). IALs create localized states, between which variable range hopping occurs. However, in the pristine $B_{12}As_2$, the IALs are compensated by the interstitial boron atoms, and the density of localized states becomes quite small. The compensation of electrons by interstitial boron atoms was observed in β-rohmbohedral boron and α-tetragonal boron [18, 19, 20]. Silicon doping may prevent the interstitial boron atoms from compensating the IALs, thus the density of localized states increase and the IALs reappear [18].

**Table 5.1 Fitting parameters based on variable range hopping conduction for $B_{12}As_2$**

| Si Concentration | $T_0$ | $N(E_F)$ |
|---|---|---|
| $cm^{-3}$ | $10^8$ K | States/eV unit cell |
| $6.5 \times 10^{18}$ | 3.51 | 0.082 |
| $1.1 \times 10^{20}$ (intentionally doped) | 0.468 | 0.616 |

An alternate explanation for *p*-type doping was that silicon atoms substitute for arsenic sites. Si has one less electron than As, thus introducing a hole. However, these experiments were not capable of determining which mechanism was most likely.

### *5.3.2 Acceptor carrier concentration and activation energy level*

The pristine $B_{12}As_2$ films were *p*-type with a room temperature hole concentration on the order of $10^{12}$ - $10^{15}cm^{-3}$. This possibly results from the intrinsic acceptor levels due to the electron deficiency. A typical carrier concentration profile for temperature ranging from 300 to 500 K is shown in Figure 5.2. The hole concentration increased with temperature.

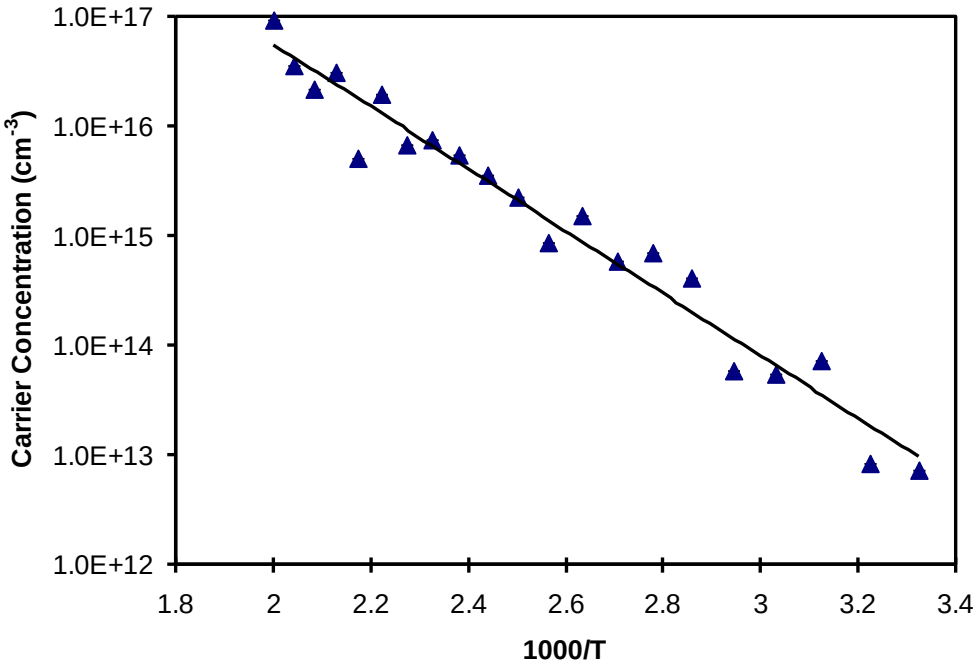


**Figure 5.2 Carrier concentrations of an undoped $B_{12}As_2$ films on 6H-SiC versus reciprocal temperature.**

The activation energy of the acceptor can be extracted from a plot of the logarithm carrier concentration versus reciprocal temperatures by the following equation.

$$p = \sqrt{\frac{N_A - N_D}{g}} \exp(-\frac{Ea}{2kT}) \qquad \textbf{Eq. 5-2}$$

where k is Boltzmann's constant [21].

**Table 5.2 Values of the 300K free hole concentration and the activation energy of acceptors**

| Sample | Carrier Concentration $p$ ($cm^{-3}$) | Activation Energy $Ea$(eV) | Thickness μm |
|---|---|---|---|
| 1 | $7.4 \times 10^{12}$ | 1.12 | 5.17 |
| 2 | $8.1 \times 10^{15}$ | 0.15 | 3.27 |
| 3 | $1.1 \times 10^{13}$ | 0.26 | 2.88 |
| 4 | $4.4 \times 10^{14}$ | 0.33 | 3.36 |

The activation energy of acceptors varied from 0.15 eV to 0.33 eV on $B_{12}As_2$ films with thicknesses less than 3.5μm, as shown in Table 5.2. It fell in a similar range to other wide

bandgap semiconductors; for example, the activation energies of acceptor levels in GaN varies from 0.12 to 0.21 eV [22]. But the apparent activation energy of $B_{12}As_2$ film with thickness over 3.5μm was much higher, 1.12eV, possibly due to cracks in this thicker film.

### *5.3.3 Temperature dependence of the hole mobility*

The Hall mobility as a function of temperature in the low temperature range (77-300 K) is shown in Figure 5.3. The mobility has a peak value of about 327 $cm^2V^{-1}s^{-1}$ at 137K. The temperature dependence of mobility between 77 and 107 K was approximately $T^{1.5}$. Therefore, the low temperature mobility was probably dominated by impurity scattering [23, 24]. Between 137 and 300 K, the mobility varies roughly as $T^{-1}$, which is attributed to polar phonon scattering [23, 24].

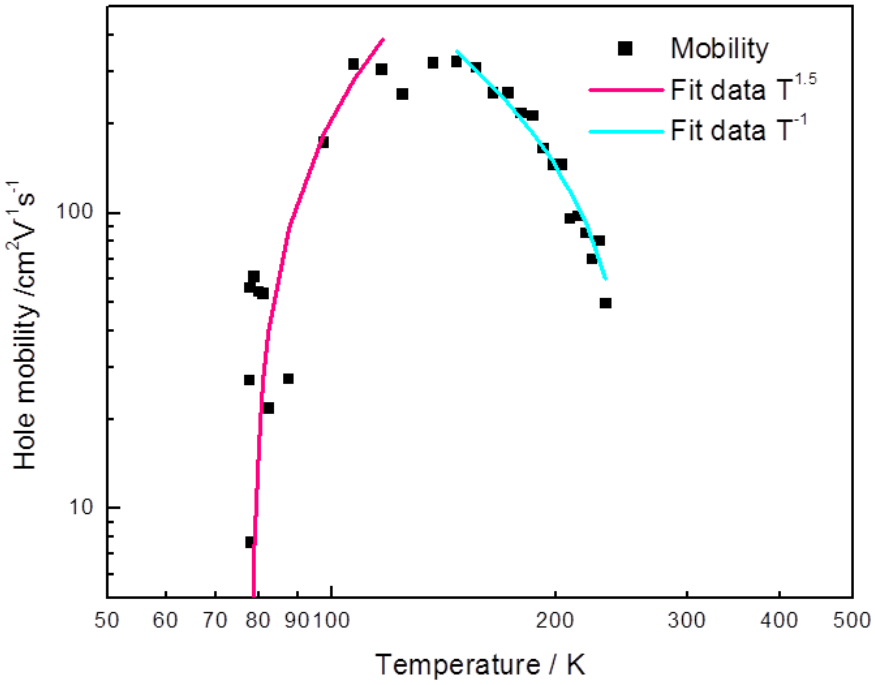


**Figure 5.3 Hole mobilities of undoped $B_{12}As_2$ films versus reciprocal temperature.**

### *5.3.4 Silicon incorporation and residual impurities concentration in pristine and Si-doped $B_{12}As_2$ films*

The major impurities present in the epitaxial $B_{12}As_2$ films were H, C, O and Si. The sources of H included the carrier gas, the $H_2$ diluent in reactant gases, and the decomposition of

the reactant gases. C and Si originated from the SiC substrates and O came from the residual ambient in the reactor.

Figure 5.4 shows the SIMS depth profiles of H, C, O and Si impurities in an undoped $B_{12}As_2$ film. The detection was stopped when the impurities concentrations were stable, usually 100~200nm. The H, C, O and Si concentrations were plotted with a logarithmic concentration scale versus depth. The concentrations of H, C and O were approximately 2.9 x $10^{19}$, 3.7 x $10^{19}$ and 1.3 x $10^{19}$ $cm^{-3}$, respectively. The background Si concentration was about 6.5 x $10^{18}$ $cm^{-3}$. Figure 5.5 shows the SIMS depth profiles of H, C, O and Si in a Si-doped sample. The concentrations of H and C remained at the same level as the undoped sample, 1.8 x $10^{19}$ and 2.0 x $10^{19}$ $cm^{-3}$. But the O concentraction dropped from 1.3 x $10^{19}$ to 4 x $10^{18}$ $cm^{-3}$. The Si concentration increased to 9.7 x $10^{19}$ $cm^{-3}$ in the doped sample, as shown in Figure 5.5, approximately 15 times higher than the pristine $B_{12}As_2$ films. The previous study showed a linear increase of the Si concentration in the $B_{12}As_2$ film with $SiH_4$ flow rate in the gas phase [10].

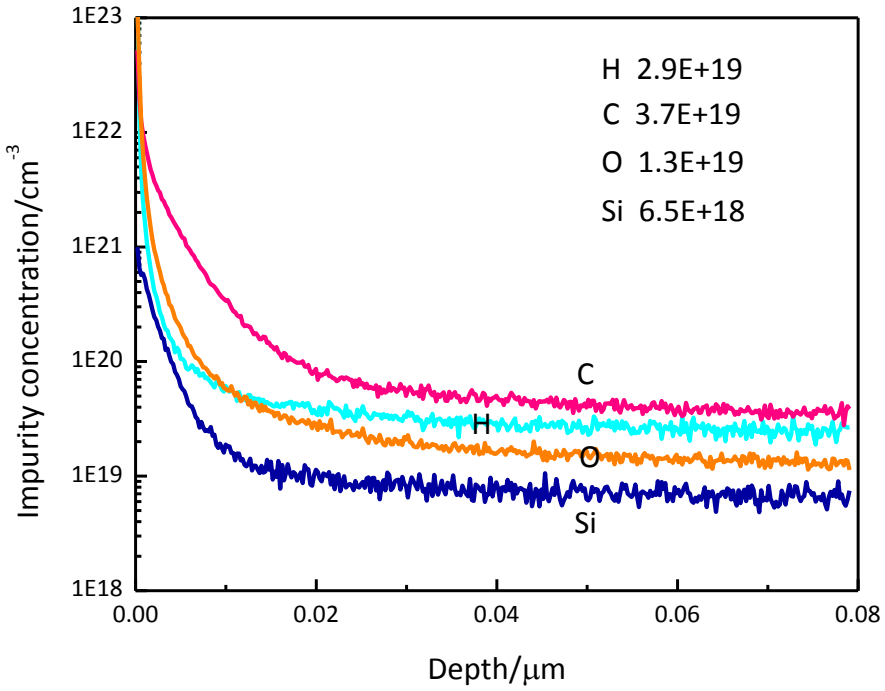


**Figure 5.4 Major impurities concentration in an undoped epitaxial $B_{12}As_2$ film grown at 1200 ℃**

Such high concentrations of Si and C in an undoped epitaxial $B_{12}As_2$ film possibly resulted from autodoping, where silicon and carbon enter the gas phase from the substrate and then re-incorporate into the depositing film.

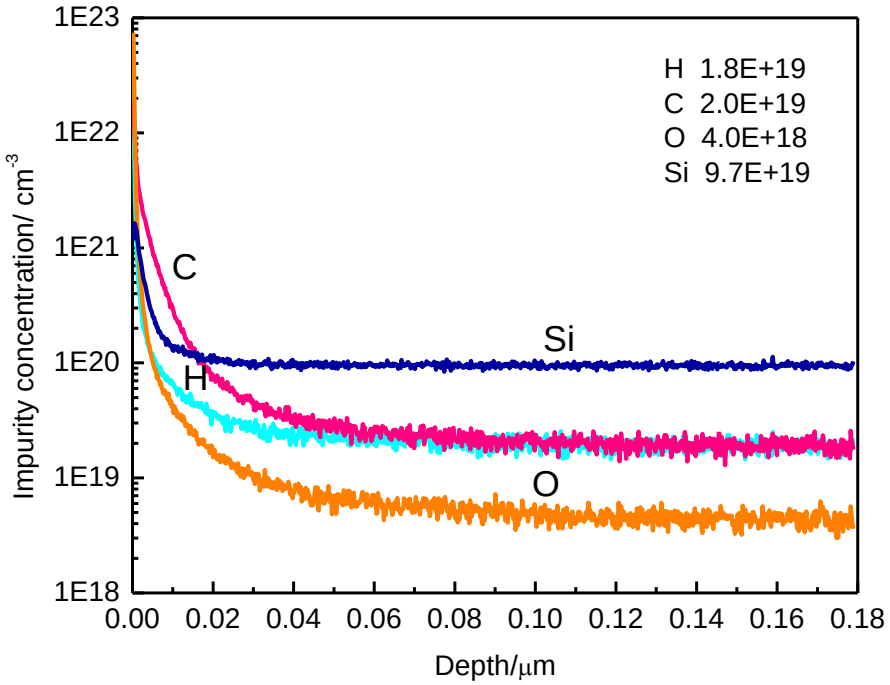


**Figure 5.5 Major impurities concentration in a Si-doped $B_{12}As_2$ grown at 1350 ℃ with a $SiH_4$ flow rate of 50 sccm**

The Si concentration in the $B_{12}As_2$ film also depended on the growth conditions and crystal quality. The effect of growth temperature and substrate orientations on the Si concentrations in doped $B_{12}As_2$ epilayers, is depicted in Figure 5.6. As the temperature increased from 1225 ℃ to 1375 ℃, the Si concentration in the epilayer increased from 7.5 x $10^{18}$ $cm^{-3}$ to 3.6 x $10^{19}$ $cm^{-3}$. When the temperature increased, the diffusion coefficient of Si into the epilayer increased, and the boron interstitials tend to drop out. Thus, more residual Si was incorporated as the growth temperature was increased.

From Figure 5.6, the Si concentration present in the $B_{12}As_2$ film grown on the on-axis *c*-plane 4H-SiC was higher than that of the sample grown on the *c*-plane 4H-SiC with 7 ° offcut towards [1-100]. This difference could be attributed to the higher crystal quality resulting from the off-axis substrate. A major defect, twins are eliminated on this specific off-axis substrate, yielding lower defect densities and levels of strain. Consequently, Si diffusion and incorporation in $B_{12}As_2$ is more difficult with higher crystal quality. Silicon incorporation can increase in

higher defect density films, as the silicon can decorate the defects. There are more opportunities for Si to react with and combine with dangling bonds at defects compared to lower defect density films.

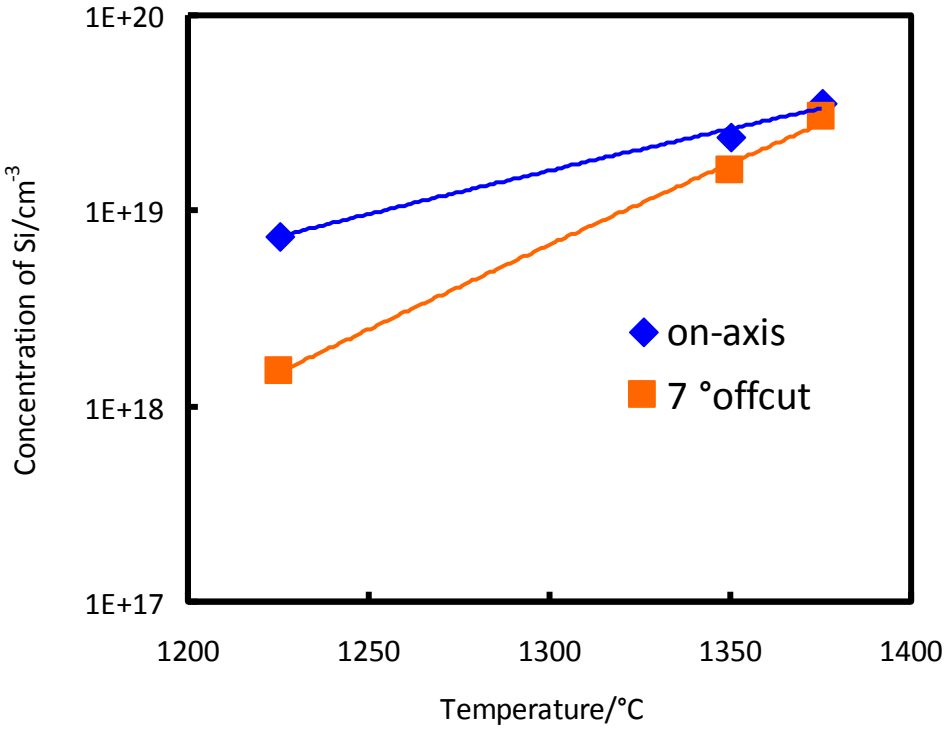


**Figure 5.6 Si concentrations in $B_{12}As_2$ grown at 1225~1375 ℃ with $SiH_4$ flow rate of 20 to sccm on on-axis *c*-plane 4H-SiC and 7 °off-axis towards [1-100]**

The correlation between the residual impurities, C, H and O, and the dopant, Si, was analyzed in a $B_{12}As_2$ film grown at 1375 ℃ with several layers doped with different Si concentrations. The first layer in this sample was an undoped $B_{12}As_2$ layer, the second was doped with 20 sccm $SiH_4$, the third layer with 40 sccm $SiH_4$, the fourth layer with 60 sccm $SiH_4$, the fifth layer with 80 sccm $SiH_4$, the sixth layer with 100 sccm $SiH_4$, and the last layer was another undoped $B_{12}As_2$ layer. The $SiH_4$ flow rate scheme and the result concentration profiles of H, C, O and Si are illustrated in Figure 5.7. The SIMS detection went through the entire $B_{12}As_2$ layer with a total thickness of 4.6 μm and reached the interface between $B_{12}As_2$ and SiC.

The Si, C and H concentrations changes with the $SiH_4$ flow rate. But O concentration remained at the same value of 1 x $10^{18}$ $cm^{-3}$ throughout all layers. This suggests that the O concentration is not related to the Si doping, and it only originates from the background ambient. The Si concentrations were changed five times in the gas phase, however, only three peaks are

observed in the solid phase. During the $SiH_4$ flow rate of 20 and 40 sccm growth periods, the Si concentrations in the solid phase didn't change. In the $SiH_4$ flow rate of 60, 80 and 100 sccm step, the Si concentrations exhibit bell distributions and the mean concentration is nearly the same. This trend does not follow the designed Si profile in the gas phase. It is possibly due to the growth and doping temperature is high, 1375 ℃, at which the Si diffusion coefficient is sufficient high to cause the redistribution of Si in the $B_{12}As_2$ film. The Si concentration in the solid phase following that in the gas phase was observed at lower growth temperature, 1250 ℃ by Xu *et al* [10].

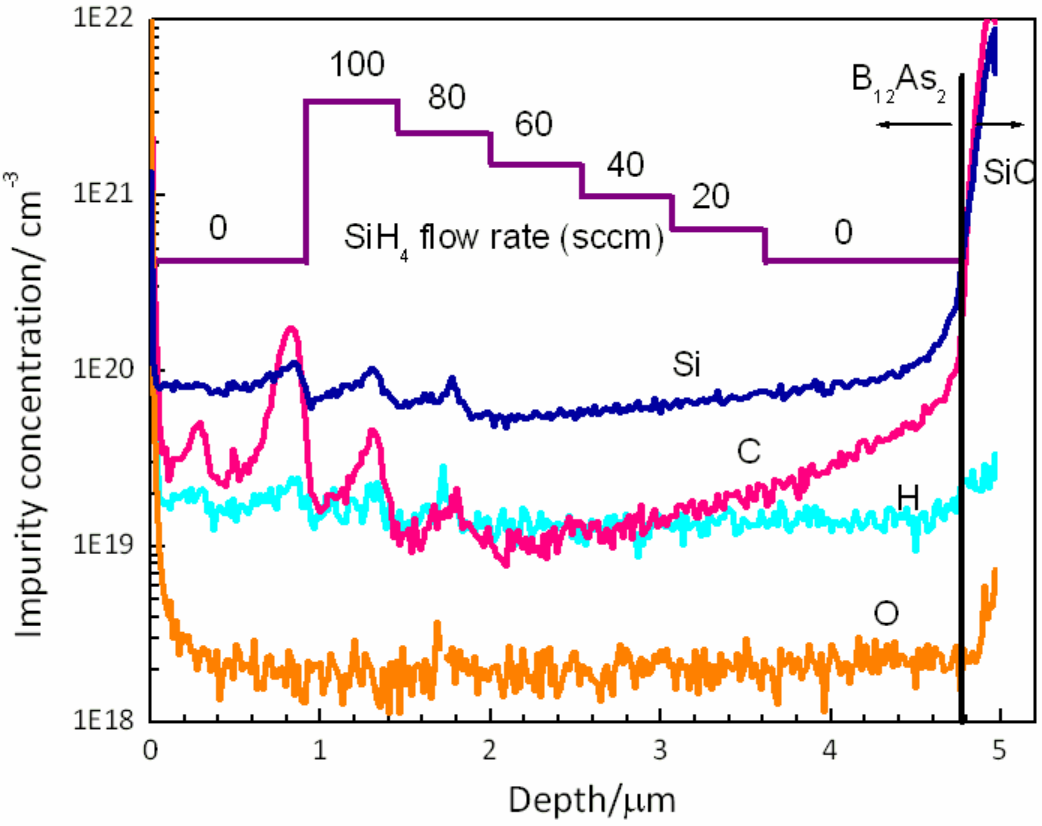


**Figure 5.7 SIMS depth profiles of H, C and Si in a layer-doped $B_{12}As_2$ grown at 1375 ℃ with $SiH_4$ flow rate varies from 20 to 100 sccm**

The H concentrations have a similar trend as the Si concentration. Peaks in the H concentration correspond to peaks in the Si concentration. This phenomenon is similar to the behavior of hydrogen in carbon doped p-type GaAs [25, 26]. The same trend was also seen by Xu et al [10] the Si-doped $B_{12}As_2$ film. Hydrogen is believed to form a Si-H complex as the

absence of reduction or redistribution of H after annealing. However, the carbon concentrations in this example also tracked the Si concentration. It may be that carbon forms complexes with Si and H in the doped epilayer, but further evidence is needed to prove this speculation.

### *5.3.5 Electrical properties in Si-doped $B_{12}As_2$ films*

As demonstrated, the Si concentration in the $B_{12}As_2$ film can be tuned by varying the $SiH_4$ flow rate and thereby its electrical properties can be controlled. The resistivity decreased two orders of magnitude when the Si concentration was increased by two orders of magnitude, as shown in Table 5.3. Si is a *p*-type dopant and the holes Si generates in the icosahedral internal-bonding states reduce the resistivity. The resistivity of $B_{12}As_2$ film is also significantly reduced by thermal annealing. Several samples were annealed at 600 ℃ in an Ar ambient for 5 minutes. The resistivity dropped one order of magnitude by thermal annealing, consistent with the observations in previous reports [6, 10].

**Table 5.3 Resistivity of $B_{12}As_2$ film with different Si concentration at 300 K**

| Si Concentration ($cm^{-3}$) | Resistivity (ohm cm) | Resistivity After Annealing (ohm cm) |
|---|---|---|
| $6.5 \times 10^{18}$ | $3.80 \times 10^{4}$ | N/A |
| $3.6 \times 10^{19}$ | $1.27 \times 10^{3}$ | N/A |
| $9.1 \times 10^{19}$ | $5.68 \times 10^{2}$ | 83.6 |
| $1.8 \times 10^{20}$ | $4.57 \times 10^{2}$ | 23.2 |

Doping with Si also reduced the hole mobility, as determined by Hall effect measurements. Figure 5.8 depicts the mobility variations with the Si concentrations. The mobility was 42.4 $cm^2V^{-1}s^{-1}$ at a Si concentration of $6.5 \times 10^{18}$ $cm^{-3}$, and dropped to 3.5 $cm^2V^{-1}s^{-1}$ at a Si concentration of $1.1 \times 10^{20}$ $cm^{-3}$. As Si replaces As, this may also create As intersitials within the crystals and structural defects in the epilayer, leading to the reduction of Hall mobility. This trend is typical from the charged impurity Coulomb scattering as well as the free carrier interaction, similar to the behavior of mobility versus doping concentrations in Ge, Si and GaAs at room temperature [27]. For Si, the hole mobility drops from 450 to 100 when the impurity concentration increased from $1 \times 10^{16}$ $cm^{-3}$ to $3 \times 10^{18}$ $cm^{-3}$ [27].

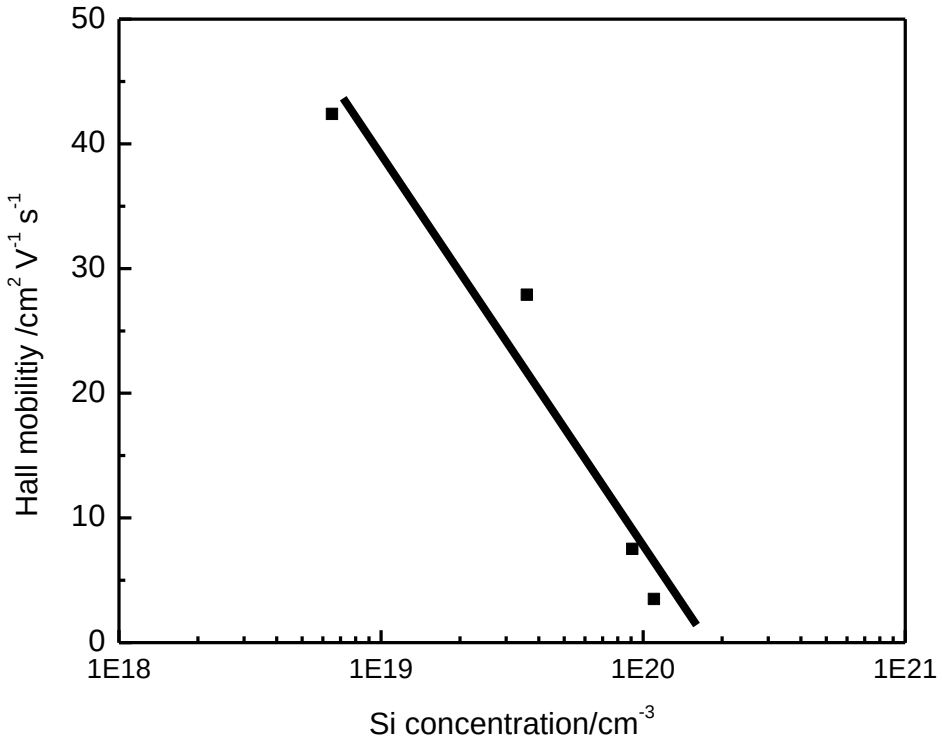


**Figure 5.8 Room temperature hole mobility of $B_{12}As_2$ on 4H-SiC grown at 1350 ℃ versus Si dopants concentrations as measured by SIMS.**

The hole mobility is also related to the hole concentration present in the $B_{12}As_2$ films (Figure 5.9). The mobility decreased when the carrier concentration increased in the Si-doped samples. Also, the arsenic interstitials resulting from Si doping provides more scattering centers for the charge carriers.

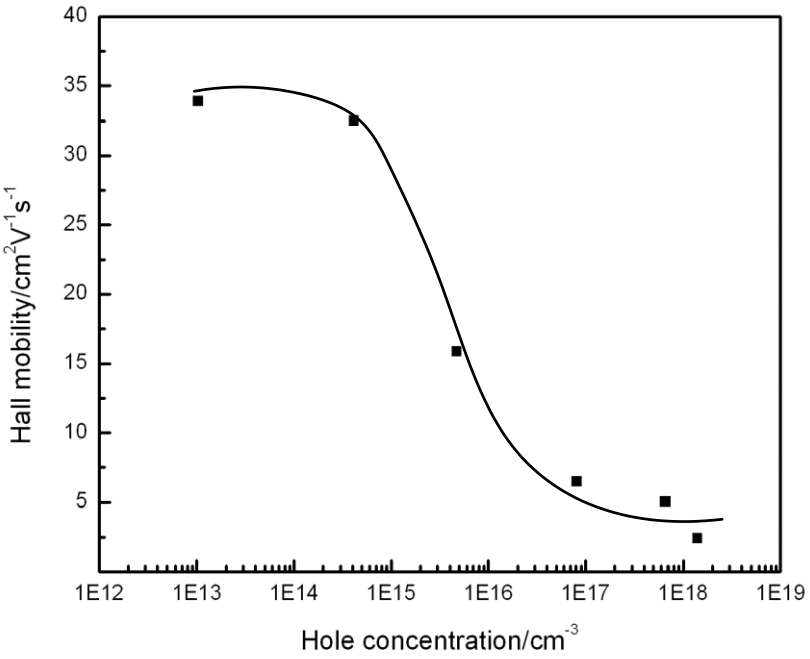


**Figure 5.9 Room temperature Hall mobility of $B_{12}As_2$ on 4H-SiC versus hole concentrations**

## 5.4 Conclusion

In conclusion, intrinsic $B_{12}As_2$ exhibits a variable-range-hopping conduction mode which is commonly observed in a highly disordered system. The density of localized states is quit small in the pristine $B_{12}As_2$, as the intrinsic acceptor levels are compensated by the interstitial boron atoms. However, in Si-doped $B_{12}As_2$, Si may prevent the interstitial boron atoms from compensating the intrinsic acceptor levels, yielding a decreased density of localized states.

The pristine $B_{12}As_2$ films are *p*-type with a room temperature hole concentration on the order of $10^{12}$ - $10^{15}$cm$^{-3}$. The thermal activation energy of acceptors varies from 0.15 eV to 0.33 eV, on $B_{12}As_2$ films of thickness less than 3.5μm, which also depends on the crystal quality of the epitaxial film. The Hall mobility is dominated by impurity scattering at low temperatures, and by polar phonon scattering at high temperatures.

H, C, O and Si are the major impurities present in the epitaxial $B_{12}As_2$ films. The concentrations of H, C and O are on the order of $10^{19}$ cm$^{-3}$and the background Si concentration is on the order of $10^{18}$ cm$^{-3}$. The Si concentration can be controlled by changing the Si concentration in the gas phase, and are affected by the growth temperature and substrate

orientation. The H and C concentrations track the change of Si concentrations possibly due to the formation of the Si-C-H complex.

The resistivity in the $B_{12}As_2$ films can be tuned by Si doping and annealing. It decreases two orders of magnitude by doping, as well as annealing. The Hall mobility of $B_{12}As_2$ epilayer was significantly reduced with increasing dopant concentration due to the creation of As intersitials and structural defects within the crystals. The mobility decreased when the carrier concentration decreased in the Si-doped samples.

# Reference


[1] N. Tsolfanidis, Measurement and Detection of Radiation, 2nd Ed.; Talyor & Francis: Bistal, (1995)

[2] M. Carrard, D. Emin and L. Zuppiroli, *Phys. Rev. B*, 51(17), 11270 (1995)

[3] D. Emin, *J. Solid State Chem.*, 177, 1619 (2004)

[4] D. Emin and T. L. Aselage, *J. App. Phys.*, 97, 013529 (2005)

[5] D. Emin, *J. Solid State Chem.*, 179, 2791 (2006)

[6] R.H. Wang, D. Zubia, T. O'Neil, D. Emin, T. Aselage, W. Zhang and S.D. Hersee, *J. Electron. Mater.*, 29 (11), 1304 (2000)

[7] R. Nagarajan, Z. Xu, J. H. Edgar, F. Baig, J. Chaudhuri, Z. Rek, E. A. Payzant, H. M. Meyer, J. Pomeroy and M. Kuball, *J. Cryst. Growth*, 273, 431 (2005)

[8] X. Zhou, J. H. Edgar and S. Speakman, *J. Cryst. Growth*, 293, 162 (2006)

[9] Y. Zhang, H. Chen, M. Dudley, Y. Zhang, J. H. Edgar, Y.Gong, S. Bakalova, M. Kuball, L. Zhang, D. Su, K. Kisslinger, Y.Zhu, *Mater. Res. Soc. Symp. Proc.* 1246, B04-2 (2010)

[10] Z. Xu, J. H. Edgar, D.C. Look, S. Baumann, R. J. Bleiler, S. H. Wang and S. E. Mohney, *Appl. Phys.*, 101, 053710 (2007)

[11] O.A.Golikov, *Phys. Status Solidi* A 51, 11 (1979)

[12] Y. Gong, M. Tapajna, S. Bakalova, Y. Zhang, J.H. Edgar, Y. Zhang, M. Dudley, M. Hopkins, and M. Kuball., *Appl. Phys. Lett.*, 96(22), 223505(2010)

[13] S. H. Wang, E. M. Lysczek, B. Liu, S. E. Mohney, Z. Xu, R. Nagarajan and J. H. Edgar, *Appl. Phys. Lett.*, 87, 042103 (2005)

[14] H. Werheit, H. G. Leis, *Phys. Status Solidi* 41, 247(1970)

[15] A. Szadkowski, *J Less-Common Metals*, 67, 551(1979)

[16] O.A.Golikov, *Chemtronics*, 5, 3(1991)

[17] H. Werheit, Electronic Transport in Boron-rich Solids, Springer, Netherland (2005)

[18] K. Kirihara, Y. Shimizu, Y. Yamada, F. Esaka, T. Sasaki, N. Koshizaki, H. Yamamoto, S. Shamoto, and K. Kimura, *Appl. Phys. Lett.*, 97, 212105 (2010)

[19] M. J. van Setten, M. A. Uijttewaal, G. A. de Wijs, and R. A. de Groot, *J. Am. Chem. Soc.*, 129, 2458 (2007).

[20] T. Ogitsu, F. Gygi, J. Reed, Y. Motome, E. Schwegler, and G. Galli, *J. Am. Chem. Soc.*, 131, 1903 (2009)

[21] D. K. Schroder, Semiconductor Material and Device Characterizations, 3rd edition, John Wiley & Sons, New Jersey, (2006)

[22] Y. Gong, Investigation of Wide Bandgap Semiconductors: Electrical, Optical, and Structural Properties, PhD Thesis, (2007)

[23] D. A. Anderson, N. Apsley, *Semicond. Sci. Technol. UK*, 1, 187 (1986)

[24] J. H. Edgar, Properties of Group III Nitrides, INSPEC, London, (1994)

[25] B. Clerjaud, F. Gendron, M. Krause, and W. Ulrici, *Phys. Rev. Lett.* 65, 1800 (1990)

[26] J. Mimilar-Arroyo and S. W. Bland, *Mod. Phys. Lett. B*, 15, 585 (2001)

[27] S. M. Sze, Physics of Semiconductor Devices, 2nd ed. , Wiley, New York, (1981)

# Chapter 6 - Growth of Icosahedral Boron Arsenide ($B_{12}As_2$) Nanowires by Chemical Vapor Deposition

## 6.1 Introduction

Motivated by the extensive research on graphene and carbon nanotubes (CNTs), interest has been stimulated in low-dimensional boron and its compounds for potential applications in nanodevices and nanotechnologies due to their extraordinary properties [1]. In recent years, boron nanowires (BNWs) and boron carbide nanowires (BCNWs) have been successfully synthesized through a variety of methods, including radio frequency (RF) – magnetron sputtering [2], chemical vapor deposition (CVD) [3], laser ablation [4], thermal vapor transport process [5, 6], solid state chemical reaction [7], and CNT template assisted growth [8, 9]. However, nanowires of icosahedral boron arsenide, $B_{12}As_2$, sharing the same structure with α-boron and boron carbide, has not previously been reported.

$B_{12}As_2$ is a wide bandgap (3.2 eV) semiconductor, with high melting point, hardness, and resistance to radiation damage. Its unusual structure and bonding configuration enable $B_{12}As_2$ to self-heal from radiation damage [10, 11, 12]. Thus, the high radiation tolerance makes it a good candidate for long-lived nuclear batteries, such as alpha- or beta-voltaic cells, devices that directly convert nuclear energy into electrical power. Also, the high thermal neutron capture cross-section of the B-10 isotope makes $B_{12}As_2$ promising for solid-state neutron detectors, potentially resolving the shortage of current He-3 gas detectors. Unlike beta-boron and boron carbide which have inherently low charge carrier mobilities ($<1 cm^2V^{-1}s^{-1}$), the hole mobility for $B_{12}As_2$ is relatively high (~80 $cm^2V^{-1}s^{-1}$). This property is beneficial to electronic device performance.

A potential motivation for the present study is the possibility of producing defect-free $B_{12}As_2$. This is very difficult to achieve with either broad epitaxial films or bulk crystals. For example, thin films of epitaxial $B_{12}As_2$ have been produced by chemical vapor deposition (CVD) on (0001) 6H- or 4H-SiC substrates with or without misorientation [13, 14, 15, 16]. The $B_{12}As_2$ epilayers grown on on-axis 6H-SiC contain a high density of translational variants and rotational twins as a consequence of the different lattice constants and symmetries of the film and the substrate. Recently, twin-free $B_{12}As_2$ epilayers were achieved on (0001) 4H-SiC with 7 °

misorientated towards [1-100]. However, translation variants and dislocations still exist in those films. Bulk $B_{12}As_2$ crystals were synthesized by the solution growth method [17], but they also suffered from high densities of defects (as indicated by etch pit densities on the order of $10^7 cm^{-2}$) and impurities. Consequently, dislocations, traps, impurities and strains detrimentally limit the electrical transport properties of $B_{12}As_2$.

In present work, we hypothesize that $B_{12}As_2$ nanowires grown by vapor-liquid-solid method are defect-free. Since the nanowires are grown by precipitation from the liquid, boron-metal eutectic, and arsenic is fed from vapor phase, a screw dislocation is unnecessary, implying the nanowires are dislocation free. Thus, better charge carrier transport properties can be expected of the nanowires. Previously, defect-free boron carbide and silicon nanowires were produced using VLS growth [18, 19].

Another potential motivation of producing $B_{12}As_2$ nanowires is to realize different properties due to quantum mechanical effects. Synthesis and characterization of $B_{12}As_2$ nanowires will provide valuable information for constructing nano-semiconductor devices based on icosahedral borides compounds.

Therefore, we study the growth of $B_{12}As_2$ nanowires on various substrates and at a variety of temperatures to determine their growth mechanism and physical properties. As discussed above, the VLS growth required a metal catalyst, which could form a eutectic phase with boron. Nickel (Ni) and platinum (Pt) were selected in this study as they both dissolve high concentration of boron and both have relatively low eutectic temperatures. The lowest melting points of the eutectic phase roughly span the temperatures of interest, approximately 820 ℃ for B/Pt system, and 1030 ℃ for the B/Ni systems [20].

## 6.2 Experimental Procedures

$B_{12}As_2$ nanowires were synthesized via CVD in an inductively heated horizontal quartz reactor, employing 1% $B_2H_6$ in $H_2$ and 1% $AsH_3$ in $H_2$ as the source gases. The carrier gas was purified hydrogen with a constant flow rate of 3.5 SLM. All the nanowires were deposited at a temperature range of 700-1200 ℃, and a total pressure of 100 torr. The flow rate of $B_2H_6$ and $AsH_3$ were fixed at 40 and 400 sccm, respectively. The substrates utilized to produce $B_{12}As_2$ nanowires included (1) a 20 nm Ni layer on a Si wafer, (2) 12 nm thick, 200μm diameter Ni dots on a Si wafer, and (3) Pt powder randomly dispersed on a (0001) 4H-SiC with 7 ° off-axis

towards (1-100). The Ni was despersed on the Si wafer in two ways: (1) as a continuous film 20nm thick, and (2) as 12 nm thick dots with diameters of 200μm. Pt powder was dissolved in acetone and loaded on a SiC wafer after air drying.

The surface morphologies of the $B_{12}As_2$ nanowires were characterized by optical microscopy and FE-SEM operated at 5-15kV. Their chemical compositions were analyzed by EDS, and their crystal structures were identified by XRD.

## 6.3 Results and Discussion

### *6.3.1 $B_{12}As_2$ nanowires grown on various substrates*

The morphologies of the resulting nanowires grown at 850 ℃ are shown in Figure 6.1. On the 20 nm Ni coat Si substrate, $B_{12}As_2$ nanowires covered the entire surface with random orientations (Figure 6.1(a)). Some were straight wires with sharp tips, others were bent and formed branches. The wire diameters ranged from 50 to 500 nm and their lengths varied from 5 to 15 μm.

On the patterned substrates, $B_{12}As_2$ nanowires grew only on the 12 nm Ni dots, not on the bare Si. However, the diameters of the $B_{12}As_2$ wires, 2-5μm, were much larger than those found on Ni completely covering the silicon surface (Figure 6.1(b)).

A high density of very small diameter $B_{12}As_2$ nanowires grew on Pt powder on SiC substrates, as shown in Figure 6.1 (c). The $B_{12}As_2$ nanowires grew out of the Pt particles with diameters of 25 to 300 nm. The majority were straight with a sharp tip. Thus, 20 nm Ni layer on a Si wafer and Pt powder on SiC wafer were promising substrates for the growth of $B_{12}As_2$ nanowires.

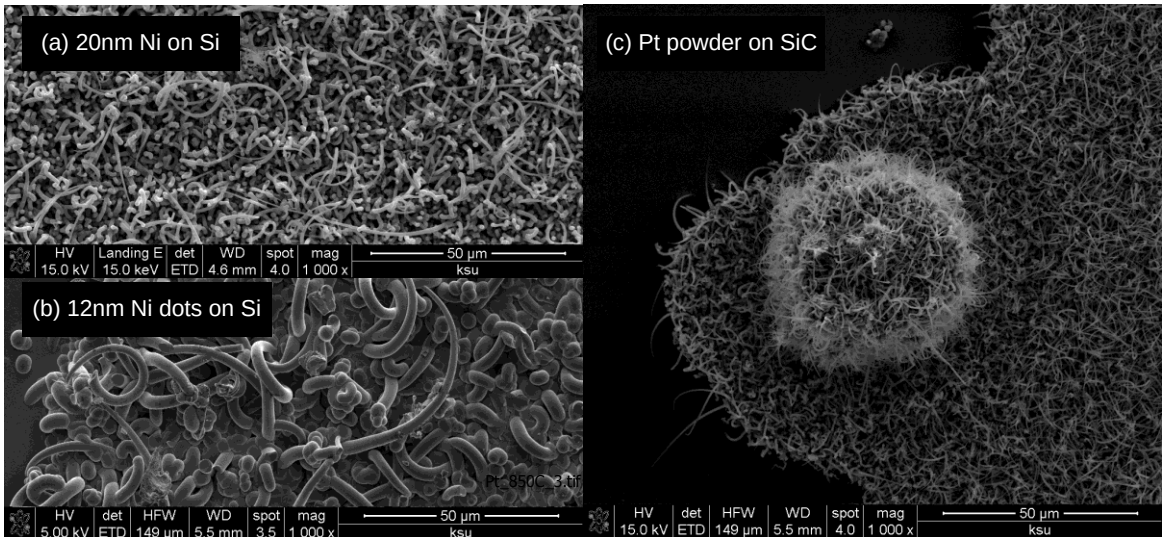


**Figure 6.1 SEM micrographs of $B_{12}As_2$ nanowires grown on various substrates at 850 ℃ (a) 20 nm Ni coating on Si wafer, (b) 12 nm thick Ni dots on Si wafer, and (c) Pt powder on SiC wafer.**

### *6.3.2 Growth mechanism of $B_{12}As_2$ nanowires*

The deposition temperature was varied to study the growth mechanism of $B_{12}As_2$ nanowires. Figure 6.2 displays the different morphologies of nanowires grown on the 20 nm Ni layer on Si at temperatures ranging from 700 to 1200 ℃. At 700 ℃, only a few short and large-diameter (~3μm) wires formed. On heating, the Ni film broke up into individual clusters, several microns in diameter, thus large-diameter wires grew out the melt Ni clusters. When temperature was increased to 850 ℃ and 900 ℃, the melt Ni clusters were smaller, yielding smaller (50-500nm) $B_{12}As_2$ nanowires. However, at 950 ℃, $B_{12}As_2$ form crystals on the substrates instead of growing out of the Ni. The density of $B_{12}As_2$ wires was relatively low, and continued to be at locations with metal particles. At 1200 ℃, polycrystalline $B_{12}As_2$ was deposited over the entire substrate. The XRD pattern of the sample grown at 1200 ℃, illustrated in Figure 6.3, confirmed the formation of polycrystalline $B_{12}As_2$.

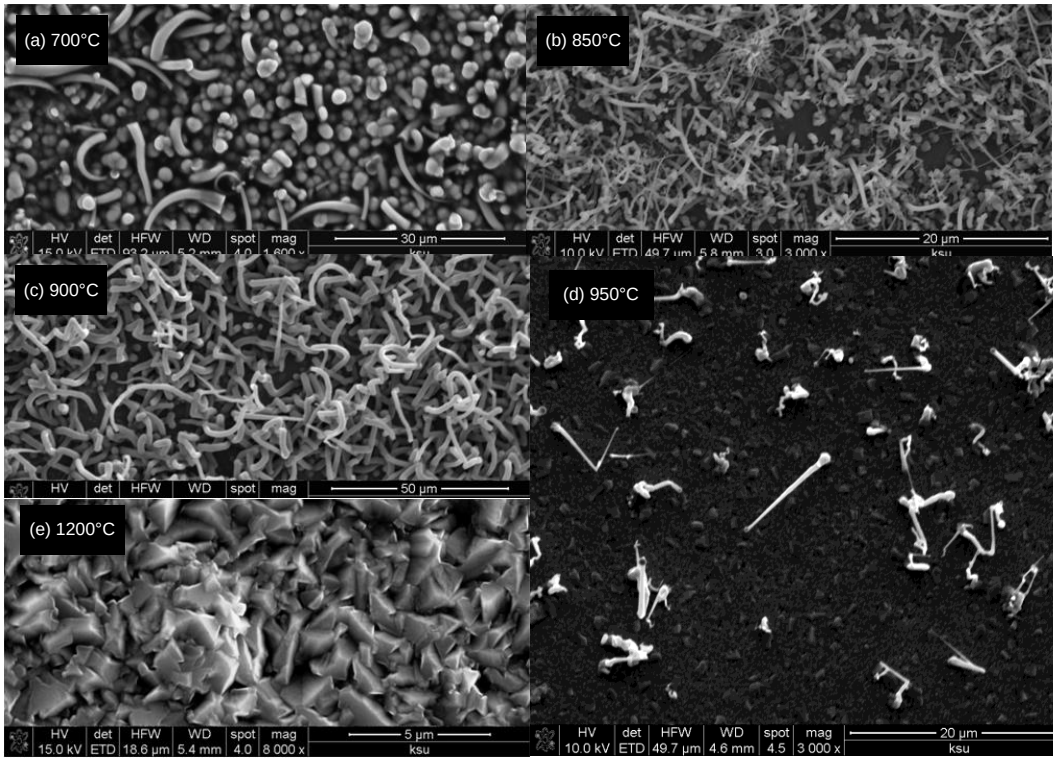


**Figure 6.2 SEM micrographs of $B_{12}As_2$ nanowires grown on 20 nm Ni coating on Si wafer at various temperatures (a) 700 ℃, (b) 850 ℃ , (c) 900 ℃, (d) 950 ℃ and (e) 1200 ℃**

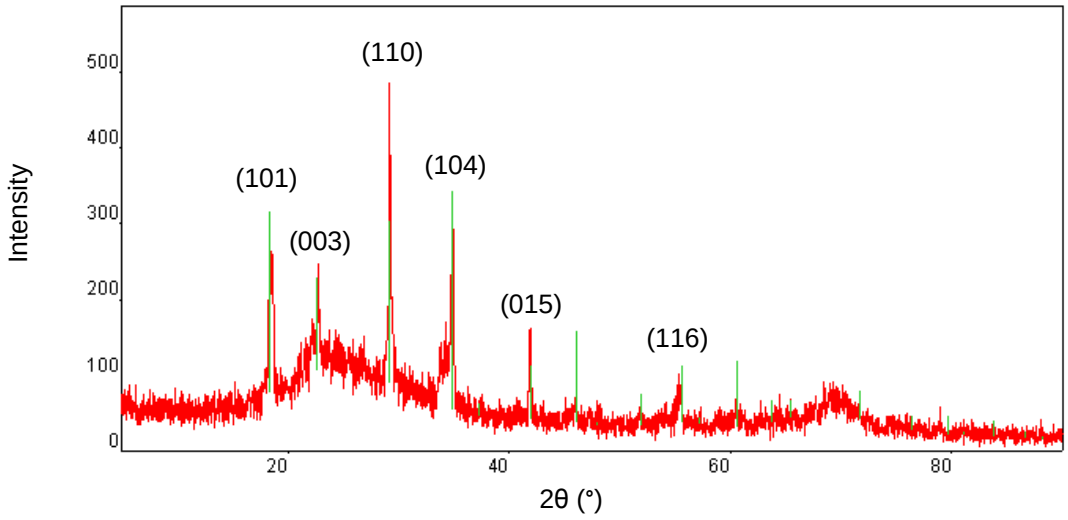


**Figure 6.3 XRD pattern of $B_{12}As_2$ nanowires grown on 20 nm Ni coating on Si wafer at 1200 ℃. The $B_{12}As_2$ peaks are labeled with their miller indices.**

Similarly, Figure 6.4 shows the different morphologies of nanowires grown on Pt powder loaded on SiC at temperatures ranging from 700 to 1200 ℃. At 700 ℃, short and large-diameter (~5μm) wires formed on the Pt particles. Pt does not melt with SiC at this temperature, $B_{12}As_2$

only deposited on the large Pt particles. At 850 ℃ and higher, the Pt and B formed a eutectic phase. This phase produced a liquid-solid interface with the silicon carbide substrate. Arsenic was fed from the vapor phase through the liquid-vapor interface, and the liquid droplet became saturated with B and As. The crystal grew by precipitation from the supersaturated liquid at the solid-liquid interface. It is clearly a VLS growth mechanism [21].

The diameter of $B_{12}As_2$ nanowires grown at 850 ℃ was in the range of 0.5-2μm. At temperatures between 900 and 950 ℃, the diameters decreased to less than 200 nm, as shown in the inserted photos in Figure 6.4 (c) and (d). When the temperature reached 1200 ℃, polycrystalline $B_{12}As_2$ was deposited over the entire substrate and on the Pt particles. Figure 6.4 (f) is an enlarged image of $B_{12}As_2$ nanowires grown at 950 ℃ on Pt powder, showing that the diameter of the wires grown at this condition ranged from 25 nm to 200 nm.

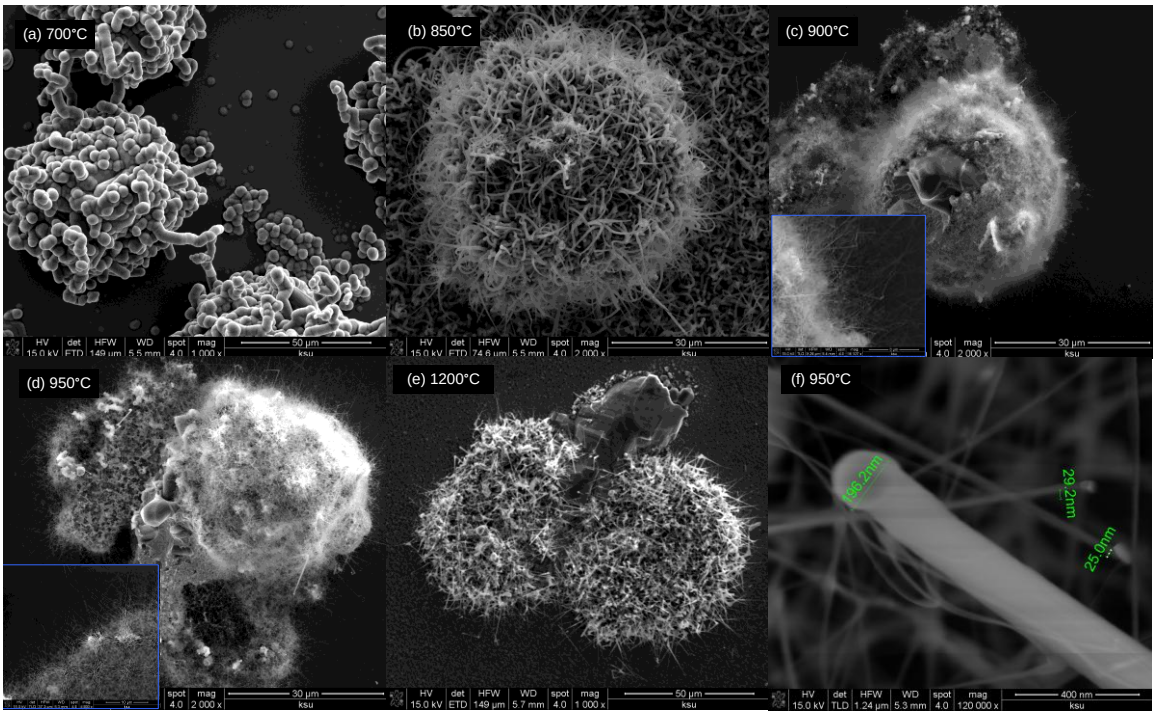


**Figure 6.4 SEM micrographs of $B_{12}As_2$ nanowires grown on Pt powder loaded on SiC wafer at various temperatures (a) 700 ℃, (b) 850 ℃, (c) 900 ℃, insert is a higher magnification image (d) 950 ℃, insert is a higher magnification image, (e) 1200 ℃ and (f) 950 ℃, high magnification image showing the diameter of wires varies from 25 to 200nm.**

The chemical compositions of the $B_{12}As_2$ wires were analyzed by EDS, and the results are listed in Table 6.1. Boron, arsenic and nickel were the majority elements present in the

$B_{12}As_2$ nanowires grown on 20 nm Ni coat on a Si wafer at 950 °. Figure 6.5(a) is the SEM image of the analyzed area. Trace amounts of C and O were detected, possibly from the ambient or surface contamination. Silicon was detected, possibly from the substrate. An obvious Ni ball was observed at the tip of the wire, which had a diameter of 340 nm. It demonstrated the growth mechanism was VLS growth.

**Table 6.1 Chemical composition (atomic%) of $B_{12}As_2$ nanowires grown on 20 nm Ni coating on Si wafer and Pt powder loaded on SiC wafer at 950 ℃ by EDS.**

| Element | Atomic% | |
|---|---|---|
| Substrate | 20 nm Ni coating on Si | Pt powder loaded on SiC |
| B | 85.93 | 84.14 |
| Si | 9.09 | 2.67 |
| Ni | 0.91 | None |
| As | 3.67 | 5.51 |
| Pt | None | 0.12 |
| C | 0.31 | 6.60 |
| O | 0.07 | 0.96 |

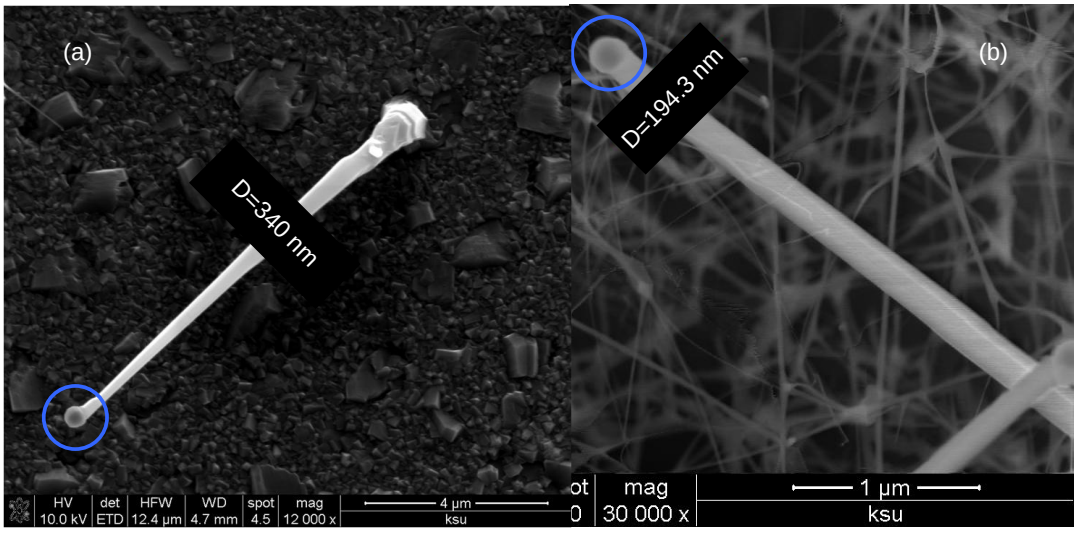


**Figure 6.5 (a) A SEM micrograph of $B_{12}As_2$ nanowires grown on 20 nm Ni coating on Si wafer at 950 ℃, showing a Ni ball at the tip and the diameter of the $B_{12}As_2$ nanowire is 340 nm, (b) a SEM micrograph of $B_{12}As_2$ nanowires grown on Pt powder loaded on SiC wafer at 950 ℃, showing a Pt ball at the tip and the diameter of the $B_{12}As_2$ nanowire is 194 nm.**

Similarly, boron, arsenic and platinum are the major elements present in the $B_{12}As_2$ nanowires grown on Pt powder loaded on Si wafer at 950 ℃. Figure 6.5(b) is the SEM image of the analyzed area. Trace amounts of O possibly come from the ambient or surface contamination. The Si and C peak originated from the substrate. Pt ball was obvious at the tip of the wire, which had a diameter of 194 nm. Its presence provides additional evidence for the VLS growth mechanism.

## 6.4 Conclusion

In conclusion, we have successfully grown $B_{12}As_2$ nanowires by CVD method on 20 nm Ni coating on Si and Pt powder loaded on SiC substrates. The diameter of the nanowires ranged from 50-500 nm and 25-200 nm for the two substrates. Pt powder loaded on SiC substrate can produce $B_{12}As_2$ nanowires with smaller diameters, but required higher growth temperatures (900-950 ℃) than that of 20 nm Ni coating on Si substrate (850-900 ℃). The lengths of the nanowires exceeded 5μm. The $B_{12}As_2$ nanowires were terminated with Ni or Pt, which indicated that they grew by the VLS mechanism. The unique structure of these nanowires, with the possibility of being defect free, suggests that they may have unique transport properties and potential applications in nanodevices.

# Reference


[1] L. Guo, R. Singh, *Mater. Res. Soc. Symp. Proc.*, 1017 (2007)

[2] L. Cao, Z. Zhang, L. Sun, C. Gao, M. He, Y. Wang, Y. Li, X. Zhang, G. Li, J. Zhang, and W. Wang, *Adv. Mater.*, 13, 1701 (2001)

[3] C. J. Otten, O. R. Lourie, M. F. Yu, J. M. Cowley, M. J. Dyer, R. S. Ruoff, and W. E. Buhro, *J. Am. Chem. Soc.*, 124, 4564 (2002)

[4] Z. Wang, Y. Shimizu, T. Sasaki, K. Kawaguchi, K. Kimura, and N. Koshizaki, *Chem.Phys. Lett.*, 368, 663 (2003)

[5] J. Z. Wu, S. H. Yun, A. Dibos, D. K. Kim, and M. Tidrow, *Microelectron. J.* 34, 463 (2003)

[6] H. Z. Zhang, R. M. Wang, L. P. You, Y. Yu, H. Chen, D. P. Yu and Y. Chen, *New J. Phys.* , 9, 13(2007)

[7] J. Jiang, M. Cao, Y. Sun, P. Wu, and J. Yuan, *Appl. Phys. Lett.*, 88, 163107 (2006).

[8] H. J. Dai, E. W. Wong, Y. Z. Lu, S. S. Fan and C. M. Lieber, *Nature*, 375, 769(1995)

[9] J. Q. Wei, B. Jiang, Y. H. Li, C. L. Xu, D. H. Wu and B. Q. Wei, *J. Mater. Chem.* 12 3121(2002)

[10] M. Carrard, D. Emin and L. Zuppiroli, *Phys. Rev. B*, 51(17), 11270 (1995).

[11] D. Emin, *J. Solid. State. Chem.*, 177, 1619 (2004)

[12] D. Emin and T. L. Aselage, *J. App. Phys.*, 97, 013529 (2005)

[13] R.H. Wang, D. Zubia, T. O'Neil, D. Emin, T. Aselage, W. Zhang and S.D. Hersee, *J. Electron. Mater.*, 29 (11), 1304 (2000)

[14] R. Nagarajan, Z. Xu, J. H. Edgar, F. Baig, J. Chaudhuri, Z. Rek, E. A. Payzant, H. M. Meyer, J. Pomeroy and M. Kuball, *J. Cryst. Growth.*, 273, 431 (2005)

[15] X. Zhou, J. H. Edgar and S. Speakman, *J. Cryst. Growth.*, 293, 162 (2006)

[16] Y. Zhang, H. Chen, M. Dudley, Y. Zhang, J. H. Edgar, Y.Gong, S. Bakalova, M. Kuball, L. Zhang, D. Su, K. Kisslinger, Y. Zhu, *Mater. Res. Soc. Symp. Proc.* 1246, B04-2 (2010)

[17] C.E. Whiteley, Y. Zhang, Y. Gong, S. Bakalova, A. Mayo, J.H. Edgar, and M. Kuball, *J. Cryst. Growth*, 318, 1, 553(2011)

[18] D. Zhang, D. N. Mcilroy, Y. Geng, M. G. Norton, *J. Mater. Sci. Lett.*, 18, 349 (1999)

[19] J. L. Gole, J. D. Stout, W. L. Rauch and Z. L. Wang, *Appl. Phys. Lett.*, 76, 17, 24(2000)

[20] M Hansen, Constitution of Binary Alloys, 2nd Ed., McGraw-Hill, New York (1958)

[21] Z. L. Wang., *Adv. Mater.*, 12, 17, 1295(2000)

# Chapter 7 - Growth of Boron Carbide Crystals from a Copper Flux[1]

Yi Zhang[1], J.H.Edgar[1], Jack Plummer[1], Clinton Whiteley[1], Hui Chen[2], Yu Zhang[2], Michael Dudley[2], Yinyan Gong[3], James Gray[3] and Martin Kuball[3]

[1]Department of Chemical Engineering, Kansas State University, Manhattan, KS, 66506

[2]Department of Materials Science and Engineering, Stony Brook University, Stony Brook, NY, 11794

[3]H.H.Wills Physics Laboratory, University of Bristol, Bristol, BS8 1TL, United Kingdom

## ABSTRACT

Boron carbide crystals ranging in size from 50 microns to several millimeters have been grown from a copper-boron carbide flux at temperatures from 1500 ℃ to 1750 ℃. The crystal size increased with growth temperature although copper evaporation limited growth at the higher temperatures. Synchrotron X-ray Laue patterns were indexed according to (001) orientation boron carbide structure, indicating the bulk crystals were single crystalline with {001} growth facets. Raman spectrum of boron carbide indicates an improved crystal quality compared to the source powder, but peaks of crystals grown from $^{11}B$ -enriched source shifted to the lower energy by 1-4 $cm^{-1}$ from literature values, possibly due to the boron isotope dependency. Fivefold symmetric defects and twin planes were common as observed by optical microscope and scanning electron microscope. Raindrop shape etch pits were formed after defect selective etching in molten potassium hydroxide at 600 ℃ for 6 minutes. Typically, the etch pit density was on the order of $10^6$ /$cm^2$.

[1] This paper was published in Mater. Res. Soc. Symp. Proc. 1164, L02-06 (2009)

## 7.1 Introduction

Boron carbide is a good candidate for nuclear applications, such as neutron shielding and neutron detection due to the high neutron absorption capability of $^{10}$B, which has thermal neutron absorption cross section of 3873 barn [1]. $^{10}$B undergoes the following neutron capture reactions when exposed to neutrons:

$$^{10}B + n \rightarrow Li(0.84MeV) + {}^{4}He(1.47MeV) + \gamma(0.48MeV)$$

$$^{10}B + n \rightarrow {}^{7}Li(0.84MeV) + {}^{4}He(1.47MeV)$$

The resulting large kinetic energies listed in parentheses leads to local heating of the solid. In addition, boron carbide is one of the icosahedral boron-riched solids, which have an unusual self-healing ability from radiation damage. Therefore, Emin and Aselage [2] proposed a solid-state boron carbide neutron detector by measuring the Seebeck emf induced by the neutron absorption. Robertson *et al* [3, 4] made a boron carbide-silicon heterojunction diode to detect neutrons by means of collecting the electrons produced by the highly energetic Li and He ions as a result of neutron capture.

The properties of boron carbide are associated with its unique crystal structure. It is based on twelve-boron-atom icosahedra [5], which reside at the corners of an α-rhombohedral unit cell, and three-atom C-C-C chains lying along the rhombohedral [111] axis. Such a complicated structure makes it difficult to produce large, single crystals with low defect densities. Chemical vapor deposition (CVD) methods [6-11] have been extensively studied and developed for boron carbide production. However, for solid-state devices, high quality crystals with good structural order, large size, and low defect densities are necessary. Millimeter size, high quality boron carbide crystals can be produced from a copper-boron carbide solution [12]. In this approach, boron carbide dissolves in the molten copper and forms a solution. As this solution is slowly cooled, boron carbide crystals nucleate and grow. The impact of temperature on the crystal size and quality was determined in this study.

## 7.2 Experiments

Boron carbide crystals were produced from a saturated copper flux. Natural abundance boron carbide, with 20% B-10 isotope, and B-11 enriched (>99%) boron carbide were used as

source materials. Boron carbide and copper powder, in a weight ratio of 1:9, were mixed in a boron nitride crucible. The mixture was held in a high temperature graphite furnace and heated to a temperature between 1500 and 1750 ℃ in 50 ℃ increments to produce a saturated solution. Argon flowed through the furnace to maintain 1atm pressure inside of the furnace. The solution was held for a period between 1 to 12 hours, and then slowly cooled at 10 ℃ /hour. Crystalline boron carbide embedded in a copper matrix was obtained via this process. The copper was dissolved away by the nitric acid and boron carbide crystals were filtered out of the acid.

To optimize the process conditions, two variables in the process were changed, the maximum temperature and the hold time, the effect of which was evaluated in terms of crystal size and quality. The maximum temperature was varied from 1500 to 1750 ℃ with 50 ℃ increment and the hold time was changed from 1, 2 to 12 hours.

Raman spectroscopy, synchrotron white beam x-ray topography, and defect selective etching were utilized to evaluate the crystal quality. Defect selective etching was carried out to assess the dislocation density via etch pit densities. For the latter, the boron carbide crystals were placed in the molten potassium hydroxide at 600 ℃ for 6 minutes.

## 7.3 Results

Well-faceted individual crystals ranging in size from 50 microns to several millimeters were produced.

### *7.3.1 Surface morphology*

In most cases, crystals grew in groups with an uneven fracture surface where crystals separated from the group. Hexagonal and prismatic crystals were produced, examples of which are shown in Figure 7.1. Two typical types of defects were observed, five-fold symmetry defects and twin plane, as shown in Figure 7.2. Twin planes, where crystals grew along two symmetry orientations from the twin boundary, were common defects observed in the boron carbide crystals produced by Aselage *et al* [12].

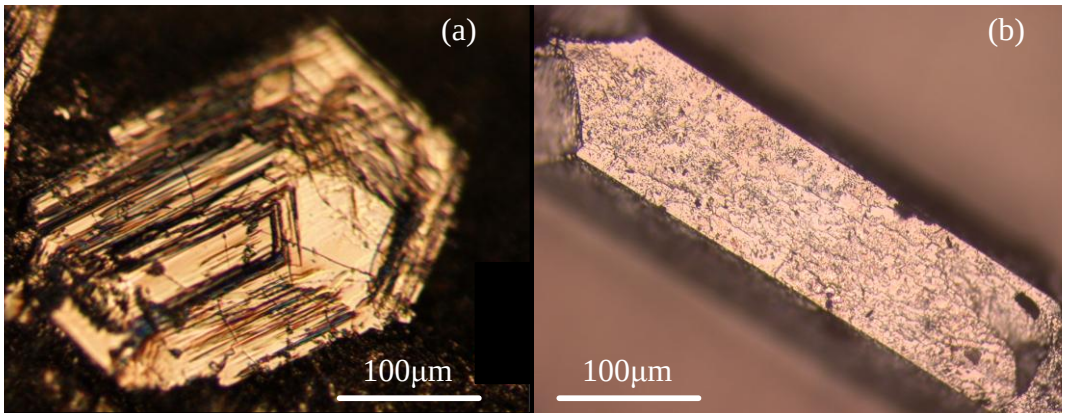


**Figure 7.1 Optical images of boron carbide crystals with (a) hexagonal, (b) prismatic and shape.**

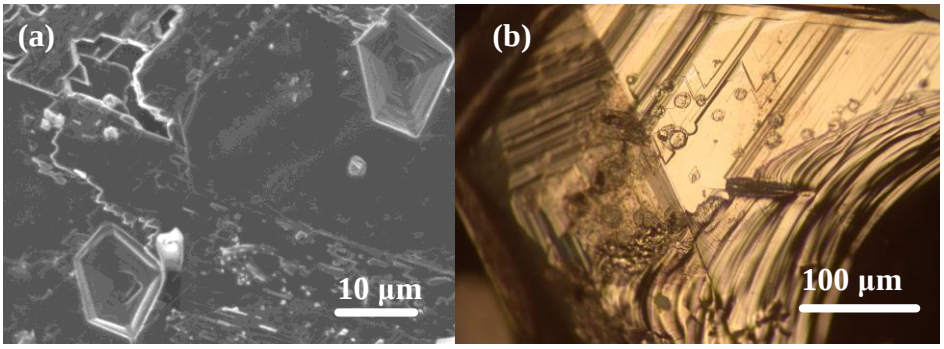


**Figure 7.2 Two typical defects present in carbide crystals. (a) SEM image of five-fold symmetry (b) optical image of twin boundary**

### *7.3.2 Effect of process conditions*

Higher temperatures, from 1600 ℃ to 1750 ℃, produced larger crystals. However, the copper evaporation became significant at such high temperatures, which limited the hold time at temperature. An even higher temperature, 1800 ℃, was tried, but no crystals were produced due to the evaporation of copper. In comparison, at relative low temperatures, from 1500 ℃ to 1600 ℃, the loss of copper is small, making longer hold time possible. Therefore, more crystals were produced, but the crystal size was smaller.

The largest crystal, 1-2 cm in the largest dimension, was obtained at 1750 ℃ and a 2-hour hold. The greatest amount of crystals was produced at 1650 ℃ and 12 hours hold. Ultimately, the best growth conditions are 1700 ℃ and 12 hours hold time.

### *7.3.3 Crystal quality*

The Raman spectrum of two boron carbide crystals grown at different temperatures are displayed in Figure 7.3. The Raman spectra of the crystal grown at 1700 ℃ is consistent with the literature spectra of single crystalline boron carbide with a 4:1 atomic ratio of boron to carbon [13]. The two prominent, narrow bands at 481 and 534 $cm^{-1}$ suggests that the chain structure is well-ordered. However, for the crystals grown from $^{11}B$ -enriched source, at 1550 ℃, these peaks are shifted to lower energy by 1-4 $cm^{-1}$ compared to those grown from natural boron carbide source, which may be due the boron isotope dependency. Aselage et al [14] reported that the Raman peaks were shifted to lower wavenumbers for $^{11}B$ -enriched boron carbide.

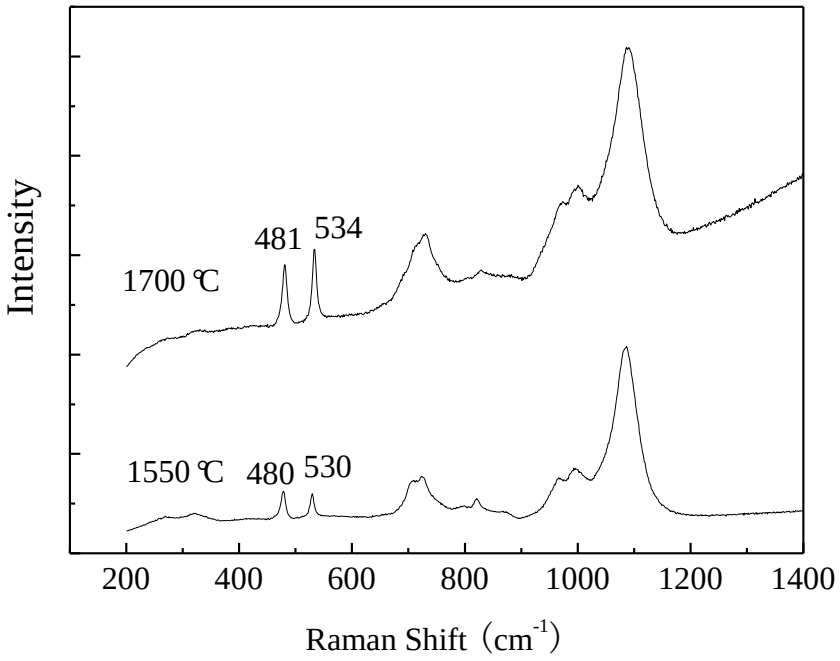


**Figure 7.3 Raman spectrum of boron carbide crystals grown at various temperatures. The crystal grown at 1700 ℃ employed natural abundance boron, while the crystal grown at 1550 ℃ used boron carbide which was isotopically enriched with $^{11}B$.**

Well defined X-ray Laue patterns from synchrotron white beam X-ray topography (SWBXT), shown in Figure 7.4, were indexed according to (001) orientation boron carbide structure, indicating the bulk crystals were single crystalline with (001) growth planes.

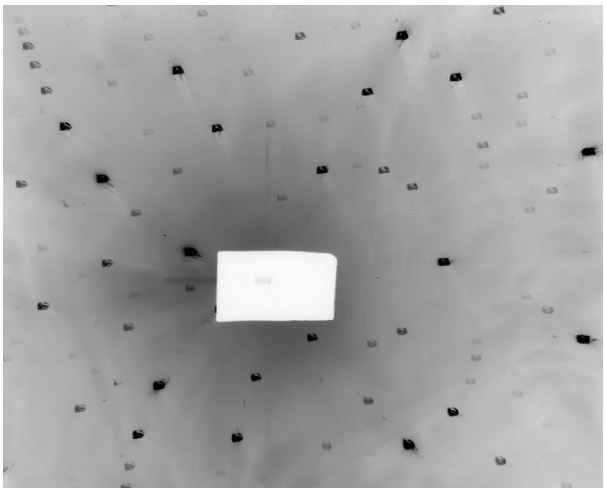

**Figure 7.4 X-ray Laue pattern of boron carbide crystals from SWBXT**

Raindrop-shape pits were the main shape formed by the etching of these crystals. Parallel grooves were also formed (Figure 7.5(a)). Because the etch pits are all oriented in the same direction, as clearly displayed in a SEM image, Figure 7.5 (b), this suggests that they are associated with crystalline defects, possibly dislocations. The etch pits density of the crystal grown at 1700 ℃ was on the order of $10^6$ etch pits/$cm^2$.

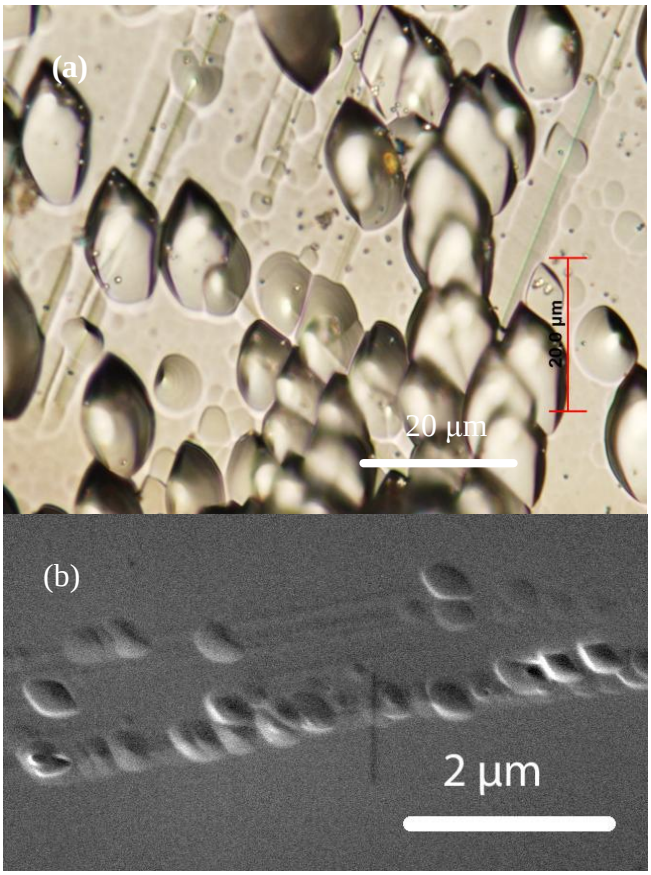


**Figure 7.5 The etch pits in the crystals (a) optical image of raindrop-shape etch pits (b) SEM image, all etch pits oriented in the same direction along a line**

## 7.4 Conclusions

Boron carbide crystals, ranging in sizes from 50 microns to several millimeters, were successfully produced from a copper flux. Higher temperatures, from 1600 ℃ to 1750 ℃, produced larger crystals. At relative low temperatures, from 1500 ℃ to 1600 ℃, more crystals were produced, but the crystal size was smaller. Fivefold symmetry defects and twin planes were typically observed. The best growth conditions were 1700 ℃ and 12 hours hold time.

The Raman spectrum of boron carbide demonstrated single crystalline boron carbide crystals with 4:1 boron to carbon ratio were produced. However, for the crystals grown from $^{11}B$ -enriched source, peaks are shifted by 1-4 $cm^{-1}$ from literature values possibly due to the boron isotope dependency. X-ray Laue patterns from synchrotron white beam X-ray topography (SWBXT) indicated that the bulk crystals were single crystalline with {001} growth facets. The

typical etch pit density after defect selective etching of these crystals by molten KOH was $10^6/cm^2$.

## Acknowledgments

This work was supported by National Science Foundation, program of materials world network, grant numbers DMR062807 and DMR0836150, and the United Kingdom Engineering and Physical Science Research Council, grant number EP/D075033/1.

# Reference


[1] A.O.Sezer and J.I.Brand, *Mater. Sci. Eng. B* 79, 191 (2001).

[2] D.Emin and T.L.Aselage, *J. Appl. Phys.* 97, 019 (2005).

[3] B.W.Robertson, S. Adenwalla, A.Harken, P.Welsch, J.I.Brand, P.A.Dowben, J.P.Classen, *Appl. Phys. Lett.* 90, 3644(2002)

[4] A.N. Caruso, P.A.Bowben, S.Balkir, Nathan Schemm, Kevin Osberg, R.W.Fairchild, Oscar Barrios Flores, Snjezana Balaz, A.D. Harken, B.W. Robertson, and J. I.Brand, *Mater. Sci. Eng. B* 135 , 129 (2006)

[5] D.Emin, *Phys. Today* 1, 55(1987).

[6] J. Winter, H.G. Esser, H. Reimer, L.Grobusch, J. Von Seggern and P. Wienhold, *J. Nucl. Mater.* 176-177, 486 (1990).

[7] K. Shirai and S. Gonda, *J. Appl. Phys.* 67, 6287 (1990).

[8] V.M.Sharapov, A.I.Kanaev, A.P.Zakharov and A.E.Gorodetsky, *J. Nucl. Mater.* 508, 191(1992).

[9] D. Byum, S.Hwang, P.A.Dowben, F.K.Perkins, F.Filips, and N.J. Ianno, *Appl. Phys.Lett.* 64, 1968(1994).

[10] S.V.Deshpande, E.Gulari, S.J. Harris and A.M.Weiner, *Appl. Phys. Lett.*, 65, 1757 (1994).

[11] J.C.Oliveira and O. Conde, *Thin Solid Films* 307, 29 (1997).

[12] T.L.Aselage, S.B.Vendeusen and B.Morosin, *J. Less-Common Metals* 166, 29 (1990).

[13] D.R.Tallant, T.L.Aselage, A.N.Campbell, and D.Emin, *Phys. Rev. B* 40, 5649 (1989).

[14] T.L.Aselage, D.R.Tallant and D.Emin, *Phys. Rev. B* 56, 3124 (1997).

# Chapter 8 - Conclusions and Future Work

Icosahedral boron arsenide, $B_{12}As_2$, is a wide bandgap (3.2 eV) semiconductor, with distinguished properties, such as self-healing from radiation damage, two orders of magnitude higher hole mobility than other boron-rich solids and with a high neutron capture cross-section of the B-10 isotope. These properties make $B_{12}As_2$ an important semiconductor in applications for long-lived radioisotope batteries and solid state neutron detectors. This dissertation discussed the heteroepitaxial growth of $B_{12}As_2$ on SiC substrates and assessed the electrical properties of undoped and Si doped layers. Additionally, $B_{12}As_2$ nanowires-growth via VLS methods, and bulk icosahedral boron carbide ($B_4C$) crystal growth by the solution method, was initiated. The following important conclusions were drawn.

(1) SiC substrates that are capable of eliminating twinning defects in heteroepitaxial $B_{12}As_2$ films include *m*-plane 15R-SiC and *c*-plane 4H-SiC with 4 ° or 7 ° off-cut towards [1-100]. The defect densities of $B_{12}As_2$ films produced on these substrates are reduced, the strain level are decreased and not only is the crystal quality increased but also the electrical properties are improved.

(2) Temperature is the most important parameter affecting the crystal quality and the strain level. The maximum room temperature hole mobility of the $B_{12}As_2$ was 80 $cm^2V^{-1}s^{-1}$, obtained on films produced at 1300 ℃. This is the optimal temperature to deposit $B_{12}As_2$ film because the epitaxial layer has the lowest defect densities, smallest residual strains, highest hole mobility and highest growth rate.

(3) A high $AsH_3$ concentration in the feed gas is advantageous because the high arsenic concentration in the gas phase it creates that prevents the loss of arsenic from the film by thermal decomposition.

(4) $B_{12}As_2$ exhibits a variable-range-hopping conduction mode which is commonly observed in a highly disordered system. The density of localized states is quite small in pristine $B_{12}As_2$, as the intrinsic acceptor levels are compensated by the interstitial boron atoms. However, in Si-doped $B_{12}As_2$, Si may prevent the interstitial boron atoms from compensating the intrinsic acceptor levels, yielding a decreased density of localized states.

(5) The pristine $B_{12}As_2$ films are *p*-type with a room temperature hole concentration on the order of $10^{12}$ - $10^{15}cm^{-3}$. The thermal activation energy of acceptors varies from 0.15 eV to 0.33 eV.

(6) The Hall mobility is dominated by impurity scattering at low temperatures, and by polar phonon scattering at high temperatures.

(7) H, C, O and Si are the major impurities present in the epitaxial $B_{12}As_2$ films. The concentrations of H, C and O are on the order of $10^{19}$ $cm^{-3}$and the background Si concentration is on the order of $10^{18}$ $cm^{-3}$. The Si concentration can be controlled by changing the Si concentration in the gas phase, and is affected by the growth temperature and substrate orientation. The H and C concentrations track the change of Si concentrations possibly due to the formation of the Si-C-H complex.

(8) The resistivity in the $B_{12}As_2$ films can be tuned by Si doping and annealing. It decreases two orders of magnitude when the Si concentration was increased by two orders of magnitude. The Hall mobility of $B_{12}As_2$ epilayer was significantly reduced with increasing dopant concentration possibly due to the creation of As intersitials and structural defects within the crystals.

(9) $B_{12}As_2$ nanowires were produce using Ni and Pt as catalyst in a CVD system, with diameters ranged from 50-500 nm and 25-200 nm, respectively. Pt powder loaded on SiC substrate can produce $B_{12}As_2$ nanowires with smaller diameters, but require higher growth temperatures (900-950 ℃) than that of 20 nm Ni coating on Si substrate (850-900 ℃).

(10) The $B_{12}As_2$ nanowires grew by the VLS mechanism as they were terminated with Ni or Pt balls. The unique structure of these nanowires, with the possibility of defect-free, suggested that they may have unique transport properties and potential applications in nanodevices.

(11) Boron carbide crystals, ranging in sizes from 50 microns to several millimeters, were successfully produced from a copper flux. Higher temperatures, from 1600 ℃ to 1750 ℃, produced larger crystals. At relative low temperatures, from 1500 ℃ to 1600 ℃, more crystals were produced, but the individual crystal size was smaller. The best growth conditions were 1700 ℃ with a 12 hours hold time.

(12) The boron carbide crystals are single crystalline with 4:1 boron to carbon ratio. Fivefold symmetry defects and twin planes were typically observed. The typical etch pit density was $10^6$ etch pits/$cm^2$.

In the future, the following issues are of interest to study.

(1) To understand the position in the $B_{12}As_2$ crystal lattice occupied by Si, XPS or single crystal XRD (required Si-dope bulk crystals in centimeter size) should be employed.

(2) To confirm the formation of the Si-C-H complex in a Si-doped sample, the $B_{12}As_2$ films should be examined by XPS or other techniques sensitive to chemical bonds.

(3) *p-n* junctions ($B_{12}As_2$/SiC) or Schottky diode (Au/$B_{12}As_2$) using $B_{12}As_2$ film with mobilities as high as 80 $cm^2V^{-1}s^{-1}$ should be fabricated and tested under radiation by alpha-emmitters or thermal neutrons.

(4) To determine if the $B_{12}As_2$ nanowires are crystalline, TEM and selected area electron diffraction should be utilized. Electron energy loss spectrum (EELS) should be used to analyze the composition.

(5) The defect densities and the electrical properties of these $B_{12}As_2$ nanowires should be measured.

In conclusion, high quality epitaxial $B_{12}As_2$ films with two orders of magnitude higher mobility were produced by using *c*-plane 4H-SiC with 4 ° or 7 °off-cut towards [1-100] substrates under optimized conditions, and fabricating devices from these films for radioisotope batteries and solid-state neutron detectors are of interest in future. $B_{12}As_2$ is a highly disordered system exhibiting a variable-range-hopping conduction mode. Si doping decreased the resistivity and hole mobility via the substitution of either boron interstitials or arsenic atoms, requiring additional evidence to understand the Si position in $B_{12}As_2$.